ABSTRACT

Title of Document: HIGH-RESOLUTION CLOUDS AND RADIATIVE FLUXES FROM SATELLITES: TRANSFERABILTY OF METHODS AND APPLICATION TO MONSOON ISSUES

Margaret M. Wonsick, Ph. D., 2009

Directed By: Professor Rachel T. Pinker
Department of Atmospheric and Oceanic Science

High-resolution information on clouds and radiative fluxes is produced for the Indian and African monsoon regions of interest to the GEWEX Project as articulated under the Coordinated Energy and Water Cycle Observations Project (CEOP). Such data are needed to provide forcing parameters for regional climate models, to evaluate them, and to facilitate their transferability to various climatic regions. Emphasis is placed on capturing the small-scale spatial variability and the diurnal cycle of cloud systems and on improving flux retrievals under the challenging conditions of high elevation and abundant aerosol loads that are characteristic of the various monsoon regions. Once developed, the data are applied to several issues investigated under CEOP and related to hydro-climate and aerosols.

Documentation of the diurnal cycle of clouds and convection throughout the progression of the Indian monsoon has been limited due to lack of hourly satellite

data over the region prior to 1998. This study adds to the base of knowledge by contrasting the diurnal cycle of clouds and convection in six diverse sectors of the Indian monsoon region and compositing the data for the pre-, peak-, and post-monsoon seasons to better understand the evolution of the monsoon. Comparison of satellite-observed clouds to model-predicted values points out model deficiencies in simulating clouds during the peak-monsoon season and at locations with elevated terrain.

The high-resolution cloud information and cloud optical depth data derived with the radiative flux inference scheme are used to re-evaluate the "Elevated Heat Pump" (EHP) hypothesis. The hypothesis predicts early initiation and enhancement of monsoon precipitation in northern India and the Bay of Bengal due to anomalous warming caused by high aerosol loads in the Indo-Gangetic Basin. Newly derived information on convection is used to study the contrast in precipitation patterns during years with high and low aerosol loads. Evidence of the EHP effect is not found. This may be attributed to aerosol indirect effects or air-sea interactions which are not accounted for in the model simulations that were used to develop the hypothesis.

Experiments are conducted with different aerosol treatments in the radiative flux inference scheme over Africa with the goal of determining whether using observed aerosol inputs can improve on fluxes retrieved with climatological aerosol values. This question is pertinent to the African Monsoon Multidisciplinary Analysis (AMMA) program, a subprogram of CEOP, which seeks to improve prediction of the West African Monsoon. The radiation component of the surface forcing database

used for all AMMA land surface models overestimates clear-sky radiation under high aerosol loads due to poor representation of aerosols. The experiments show that flux retrievals improve when observed aerosol values are used, but biases are reduced even more significantly when aerosol absorbing properties are incorporated into the inference scheme as well. The improved scheme is then used to study the spatial and seasonal variations in downwelling surface shortwave flux and surface albedo over the African continent.

HIGH-RESOLUTION CLOUDS AND RADIATIVE FLUXES FROM SATELLITES: TRANSFERABILTY OF METHODS AND APPLICATION TO MONSOON ISSUES

By

Margaret M. Wonsick

Dissertation submitted to the Faculty of the Graduate School of the
University of Maryland, College Park, in partial fulfillment
of the requirements for the degree of
Doctor of Philosophy
2009

Advisory Committee:
Professor Rachel T. Pinker, Chair
Dr. Robert Hudson
Dr. Daniel Kirk-Davidoff
Dr. Sumant Nigam
Dr. Karen Prestegaard, Dean's Representative

Dedication

This is dedicated to my husband, who started me down the path to believing, to my children, who brought me joy when I needed it most, to my parents, who gave me the best possible start in life, and to my advisor, for renewing my confidence whenever faith started to wane.

Acknowledgements

I would like to acknowledge all of the data providers: the European Organisation for the Exploitation of Meteorological Satellites (EUMETSAT) Archive and Retrieval Facility, source of the *Meteosat-5* and *Meteosat-7* observations; the National Snow and Ice Data Center (NSIDC) at the University of Colorado, Boulder, CO, source of the IMS snow data; the NOAA-CIRES Climate Diagnostic Center, source of the NCEP Re-analysis II data; the Computational Information and Systems Laboratory (CISL) at NCAR, source of the ERA-40 Re-analysis data; and the World Radiation Monitoring Center (WRMC), source of the BSRN data. MODIS figures were downloaded from the Goddard Earth Sciences Data and Information Services Center (GES DISC) Giovanni web site. Some maps were courtesy of www.theodora.com/maps, used with permission. I would also like to thank Yves Govaerts for consulting on the Meteosat calibration and Chuan Li for tremendous assistance in data processing. Many thanks are also due to Hongqing Liu and Yingtao Ma for their assistance. This work was primarily supported under NASA grant NNG05B35G.

Statement of Originality

Limited information reviewed in this dissertation was previously published in articles which I authored or co-authored:

1. The information on sensitivity of derived fluxes to sensor calibration (in Chapter 2, Subsection 2.1.2) appeared in:

Wonsick, M., R. T. Pinker, W. Meng, and L. Nguyen, 2006: Evaluation of surface shortwave flux estimates from GOES: Sensitivity to sensor calibration. *J. Oceanic Atmos. Sci*., **23**, 927-935.

2. The evaluation of fluxes derived from *Meteosat-5* over the Tibet Plateau (in Chapter 2, Subsection 2.2) appeared in:

Yang, K., R. T. Pinker, Y. Ma, T. Koike, M. M. Wonsick, S. J. Cox, Y. Zhang, and P. Stackhouse, 2008: Evaluation of satellite estimates of downward shortwave radiation over the Tibetan Plateau. *J. Geophys. Res.*, **113**, D17204, doi:10.1029/2007JD009736.

Table of Contents

List of Acronyms

AERONET	Aerosol Robotic Network
AMMA	African Monsoon Multi-disciplinary Analyses
AOD	Aerosol Optical Depth
AVHRR	Advanced Very High Resolution Radiometer
BALTEX	Baltic Sea Experiment
BSRN	Baseline Surface Radiation Network
CALIPSO	Cloud-Aerosol Lidar and Infrared Pathfinder Satellite
CATCH	Coupling of the Tropical Atmosphere and Hydrological Cycle
CEOP	Coordinate Energy and Water Cycle Observations Project
DMSP	Defense Meteorological Satellite Program
DSSF	Downwelling Surface Shortwave Flux
ECMWF	European Centre for Medium-Range Weather Forecasts
EHP	Elevated Heat Pump
ENSO	El Nino/Southern Oscillation
EOS	Earth Observing System
GAME	GEWEX Asian Monsoon Experiment
GCIP	GEWEX Continental Scale International Project
GEWEX	Global Energy and Water Cycle Experiment
GMS	Geosynchronous Meteorological Satellite
GOCART	Global Ozone Chemistry Aerosol and Radiation Transport
GOES	Geostationary Operational Environmental Satellite
GPCP	Global Precipitation Climatology Project

IGB	Indo-Gangetic Basin
IITM	Indian Institute of Tropical Meteorology
INDOEX	Indian Ocean Experiment
INSAT	Indian National Satellite
IR	Infrared
ISCCP	International Satellite Cloud Climatology Project
ISMR	Indian Summer Monsoon Rainfall
ITCZ	Intertropical Convergence Zone
Land SAF	Land Surface Analysis Satellite Applications Facility
LBA	Large-scale Biosphere Atmosphere Experiment in Amazonia
LSM	Land Surface Model
LST	Local Standard Time
LUT	Look-up Table
MAGS	Mackenzie GEWEX Study
MISR	Multiangle Imaging Spectroradiometer
MODIS	Moderate Resolution Imaging Spectroradiometer
MSL	Mean Sea Level
NAO	North Atlantic Oscillation
NCAR	National Center for Atmospheric Research
NCEP	National Center for Environmental Prediction
POLDER	Polarization and Directionality of the Earth's Reflectances
SD	Standard Deviation
SRB	Surface Radiation Budget

SSA	Single Scattering Albedo
SST	Sea Surface Temperature
SW	Shortwave
SZA	Solar Zenith Angle
TOA	Top of the atmosphere
TOMS AI	Total Ozone Mapping Spectrometer Aerosol Index
TRMM	Tropical Rainfall Measuring Mission
UMD_SRB-F	University of Maryland Surface Radiation Budget Forward Model
UMD_SRB-O	University of Maryland Surface Radiation Budget Operational Model
UMD_SRB-R	University of Maryland Surface Radiation Budget Research Model
UTC	Coordinated Universal Time
WAM	West African Monsoon

List of Tables

List of Figures

Chapter 1: Introduction

1.1. Broader context of thesis

The objective of this thesis is closely tied to several science issues central to the Coordinated Energy and Water Cycle Observations Project (CEOP) (Bosilovich and Lawford 2002; Koike 2004), a sub-program of the Global Energy and Water Cycle Experiment (GEWEX). CEOP aims to improve understanding and prediction of continental to local-scale hydrological conditions for water resource applications, which requires transferability of regional climate models to areas of climatic interest. To support this goal, high resolution information on clouds and radiative fluxes at regional scale is needed for both model forcing and evaluation.

Among the specific objectives of CEOP are: characterizing the average hydro-climatic conditions over various regions and seasons, enhancing knowledge of water and energy cycles at high elevations; explaining how aerosols affect the hydrologic cycle; improving monsoon rainfall forecasts; and understanding the impact of aerosols on radiative forcing.

1.2. Purpose of thesis

In alignment with the CEOP objectives, the purpose of this thesis is (1) to derive information on clouds and radiative fluxes by transferability of inference schemes to newly available information from satellites in regions of climatic significance, and (2) to use the newly derived information to address climate issues in monsoon regions. Improved observational capabilities are available in the Indian monsoon region since *Meteosat-5* was moved to this region in July 1998 in support of

the Indian Ocean Experiment (INDOEX) (Ramanathan et al. 2001). These data are exploited to gain new insight over previous studies of the region that lacked the benefit of geostationary satellite observations. Newly available information on aerosols is combined with *Meteosat-7* observations over Africa to quantify the impact of aerosols on radiative flux retrievals and to analyze radiation budget parameters that have been derived with improved information on aerosol absorbing properties.

Specifically, the following scientific questions are addressed:

1. **How does the spatial distribution and diurnal cycle of clouds and convection change as the Indian monsoon evolves through the pre-monsoon, peak-monsoon, and post-monsoon seasons?**
2. **How does the aerosol load in the Indo-Gangetic Basin impact the Indian monsoon?**
3. **How are flux retrieval algorithms in the African monsoon region impacted by the source of aerosol optical depth information and the incorporation of aerosol absorbing properties?**
4. **How do the surface albedo and radiation regimes change seasonally over Africa?**

1.3. Current status of cloud and radiative flux information

The need for high-quality information on clouds and radiative fluxes has been emphasized in several research initiatives. Under the GEWEX-sponsored International Satellite Cloud Climatology Project (ISCCP) (Schiffer and Rossow 1983; Schiffer and Rossow 1985; Rossow and Schiffer 1991; Brest and Rossow 1992; Rossow and Garder 1993a and 1993b; Rossow et al. 1996; Rossow and Schiffer

1999) information on clouds and radiative fluxes from various satellites is being collected since 1983. The satellite data sources include a combination of the NOAA and DMSP series of polar orbiting satellites and the GOES, Meteosat, and GMS series of geostationary satellites. Clouds and radiative fluxes are processed globally and are available at a 280 km equal-area grid at 3-hourly temporal resolution. A newer ISCCP raw radiance product is the ISCCP DX data set which is provided independently for each satellite sampled at about 30 km at 3-hourly intervals. The ISCCP D1 cloud data are used to derive surface and top of the atmosphere (TOA) radiative fluxes known as the GEWEX Surface Radiation Budget (SRB). This initiative provides model-based global 3-hourly shortwave and longwave radiative flux parameters from 1983 – 2005 (Raschke et al. 2006).

Through NASA's Earth Observing System (EOS) mission, a series of polar orbiting satellites (e.g., *Tropical Rainfall Measuring Mission* (*TRMM*), *Terra*, and *Aqua*) have been launched with multi-channel instruments to provide detailed, high-resolution information on multiple parameters, including clouds and radiative fluxes. Instruments aboard these satellites include the Clouds and the Earth's Radiant Energy System (CERES) (Gupta et al. 2004; Li et al. 1993) sensor, the Moderate Resolution Imaging Spectroradiometer (MODIS) (Kaufman et al. 1997), and the Multiangle Imaging Spectroradiometer (MISR) (Bothwell et al. 2002). A new era in cloud observations arrived in 2006 with the launch of the CloudSat and CALIPSO satellites with sensors that measure cloud properties through radar and lidar, respectively. The instruments aboard CloudSat (Stephens et al. 2002) and CALIPSO (McGill et al. 2007) provide detailed observations of cloud vertical structure that were unattainable

with previous sensors. These satellites form part of the A-Train, a constellation of polar-orbiting satellites that fly in close formation to give nearly concurrent observations of numerous atmospheric and surface parameters. The data obtained by these specialized instruments have contributed widely to climate studies but are limited because they do not resolve the diurnal cycle of clouds and fluxes due to their once-a-day coverage of the majority of the earth.

1.4. Need for high resolution data sets

In response to the need for high resolution information for hydrological modeling, the various GEWEX subprograms (GCIP, BALTEX, GAME, MAGS, LBA, CATCH) were initiated. These programs are now consolidated under CEOP

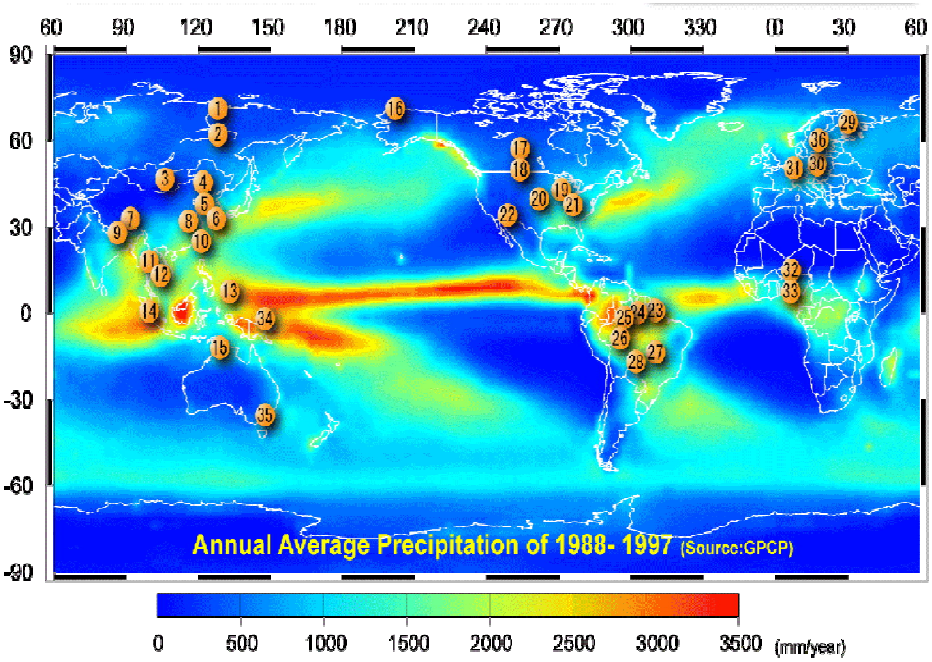

Figure 1.1. Location of CEOP reference sites.

and tied to new programs such as the African Monsoon Multi-Disciplinary Analyses (AMMA).

The map of CEOP selected reference sites is shown in Figure 1.1. At these sites, as well as at regional scales (for model evaluation), cloud and radiative flux information is needed at higher spatial resolution than what has been obtained so far through early GEWEX initiatives. The high temporal resolution of data retrieved from geostationary satellites has been shown to be of great value in model validation (Mitchell et al. 2004). Randall et al. (1991) noted that testing a model's ability to simulate the diurnal cycle can be accomplished with a short integration of the model, and yield insight into model deficiencies without the computational, time, and storage requirements needed for longer integrations. Lau et al. (2005) stated that reproducing the diurnal cycle of clouds is a particularly troubling aspect of models, and studies show this is a pre-requisite to success in seasonal and longer-term forecasts. The research in this thesis has led to the development of cloud and radiative flux products at 1-hourly, 0.125° resolution. The combination of high spatial and temporal resolution makes them good candidates for regional scale science applications.

1.5. Climatic significance of regions in the Meteosat domains

Higher resolution cloud and radiative flux information in the domains covered by *Meteosat-5* and *Meteosat-7* is necessary to address many outstanding scientific questions that originate in these regions. The monsoons in each region show little similarity in their driving mechanism, timing, and characteristics of convection. High resolution radiative flux information can be used to investigate the meso-scale processes that contribute to the uniqueness of these monsoons and possible linkages

between them. The Tibetan Plateau and the latent heat release from deep convection in the Intertropical Convergence Zone (ITCZ) over Africa represent two major planetary heating sources. Radiative flux information can be used to gain a better understanding of processes that radiatively balance these heat sources. Both domains contain significant sources of aerosol, including dust from the desert regions, high concentrations of black carbon from industrial sectors of India and Asia, and extensive biomass burning in Africa. Atmospheric circulation transports these aerosols over wide domains with significant consequences such as influencing the development or dissipation of Atlantic hurricanes (Landsea and Gray 1992). Aerosol impacts on climate change have been recognized (IPCC 2007) by their determination of radiative forcing and feedbacks. The radiative fluxes produced under this research provide the tools to address many of the above issues.

Chapter 2 describes the cloud detection algorithm and the radiative flux inference scheme that are developed to utilize observations from *Meteosat-5* and *-7*. The ensuing chapters deal with the applications of the satellite data.

Chapter 2: New Approach to Derive Clouds and Radiative Fluxes from Meteosat Data

This chapter details the transferability of methods to produce high-resolution analyses of cloud parameters and shortwave (SW) radiative fluxes over the Indian and West African monsoon regions. The satellites selected for coverage of the monsoon areas are *Meteosat-5* and *Meteosat-7*, respectively. These are geostationary satellites with the advantage of being able to provide hourly observations, in contrast to polar orbiting satellite such as the NOAA series and the more recently launched EOS satellites (i.e., *Terra, Aqua, CloudSat*), which observe each location on the earth only about once per day. Another benefit of these satellites is their fairly long data records, with *Meteosat-5* available over the Indian region since 1998 and *Meteosat-7* coverage over Africa beginning in 1997.

2.1. Cloud detection

Cloud detection is a crucial first step in this research. In addition to providing information needed to analyze clouds over the monsoon regions, the cloud detection algorithm supplies fundamental inputs to the inference scheme used to derive radiative fluxes. These include cloud amount, clear- and cloudy-sky reflectance (determines which component of the radiative transfer scheme is to be used), and clear-sky composite reflectance (used for the derivation of surface albedos).

2.1.1. Calibration

In the first step of the cloud detection procedure, a calibration is applied to convert raw counts (gray-scale) from space into reflectance values that can be used for cloud detection tests. The Meteosat satellites carry instruments to measure radiance from space in both visible (0.75 micron) and infrared (IR) (11.5 micron) wavelengths. In general, IR sensors are calibrated onboard the satellite, and some visible sensors, such as those onboard the Earth Radiation Budget Experiment (ERBE) (Barkstrom et al. 1990) and the TRMM and Terra satellites (Lee et al. 1998), carry onboard calibration systems to maintain stable radiance measurements (Minnis et al. 2002). However, most visible sensors, including those on the Meteosat series, require vicarious calibrations. The visible channel calibration procedure accounts for the following: the deep space signal, the degradation of the sensor based on its time since launch, the solar irradiance averaged over the spectral response function for the portion of the spectrum within the sensor's visible channel, sun-earth distance, and solar zenith angle (SZA). The latter two parameters are calculated by standard methods based on date, time, and location, but space count and sensor degradation are empirically derived and may vary among different calibration methods. Likewise, the solar irradiance for the visible channel depends on the choice of the equivalent width (the bandwidth of a hypothetical perfect absorber that would absorb the same amount of energy as a given spectral band) for the visible channel, and may differ among calibration methods.

Reflectance is computed as follows:

$$R = \frac{L}{E\mu_0\delta} \tag{1}$$

where

L narrow-band radiance in $Wm^{-2}sr^{-1}$.

E in-band extraterrestrial irradiance at mean sun-earth distance in $Wm^{-2}sr^{-1}\mu m^{-1}$.

δ square of the sun-earth distance in astronomical units.

μ cosine of SZA.

The narrow-band radiance, L, is given by:

$$L = C_f\,(DC - DC_o) \tag{2}$$

where

DC digital count from the satellite.

DC_o digital count offset for space.

C_f calibration coefficient that accounts for sensor degradation based on the time since the satellite was launched:

$$C_f = C_{f0} + D_f * DSL$$

where

C_{f0} calibration coefficient at launch in $Wm^{-2}sr^{-1}$/DC.

D_f daily drift in $Wm^{-2}sr^{-1}$/DC Day^{-1} 10^5.

DSL number of days since launch.

The calibration constants chosen for this implementation were developed by the European Organisation for the Exploitation of Meteorological Satellites (EUMETSAT). Table 2.1 shows the values of E and C_{f0} and the launch date used to calculate *DSL* for Meteosat-*5* and *Meteosat-7*. In order to monitor the daily drift, calibration of the visible sensor is performed about 4 to 8 times per year using simulations of radiative transfer for ocean and bright desert targets under multiple illumination conditions (Govaerts et al., 2004). The values of DC_o and D_f are updated with each calibration, and the history of their values can be found at:

http://www.eumetsat.int/groups/ops/documents/document/pdf_ten_vis_calibdetail_met5.pdf

for *Meteosat-5* and at:

http://www.eumetsat.int/groups/ops/documents/document/pdf_ten_vis_calibdetail_met7.pdf

for *Meteosat-7*.

Table 2.1. Calibration constants for *Meteosat-5* and *Meteosat-7*.

	Meteosat-5	***Meteosat-7***
E	691.6	690.8
C_{f0}	0.8184	0.9147
Launch date	2 Mar 1991	2 Sep 1997

2.1.2. Impact of calibration

The parameters derived from satellite observations depend on the quality of the calibration, which generally is not perfect. Due to the potential impact on the parameters that are to be examined, it is useful to quantify the error that can be attributed to calibration. A study was performed (Wonsick et al. 2005) on the

sensitivity of derived parameters to the choice of calibration using *GOES-8* visible radiances and calibration methods developed by NOAA's National Environmental Satellite Data and Information Service (NESDIS) (Weinreb et al. 1997) and the NASA Langley Research Center (Minnis et al. 2002).

The ultimate goal of the study was determine the sensitivity of the surface shortwave (SW) downward fluxes to sensor calibration. This was accomplished by evaluating the impact of calibration on various parameters that are used as inputs in the radiation inference schemes. First, the absolute reflectances produced by the two calibrations were compared in order to gain an understanding of the impact on this most basic parameter. Since surface SW downward fluxes are highly dependent on cloud cover, the sensitivity of cloud detection to calibration was evaluated and the results were compared to those from the Moderate Resolution Imaging Spectroradiometer (MODIS) (Platnick et. al. 2003). Finally, the differences between the satellite-estimated SW downward fluxes obtained when applying the NOAA and NASA calibrations were validated using ground measurements from three sources: SURFRAD stations (Augustine et al. 2000), the Arizona Meteorological Network (AZMET) (Brown 1989), and the Illinois State Water Survey Network (Hollinger et al.1994). The results of the study are summarized as follows: differences in visible reflectance ranged from -0.5 to 0.6% for clear-sky conditions and 0 - 3% for cloudy conditions; average difference in monthly mean cloud amount was ~3%; average difference in monthly mean surface SW downward flux was 5 Wm^{-2}, with a maximum difference of 2.5% of the average of the NOAA and NASA monthly mean (See Figure 2.1); differences in bias and rms in validations against ground station

measurements were less than 3 Wm^{-2}. These statistics give a useful estimate of the error in derived parameters that can be attributable to choice of calibration.

2.1.3. Cloud detection

Once calibrated, the data can be applied in cloud detection tests. While the currently available ISCCP cloud data set also uses Meteosat inputs, these are sub-sampled in space and in time. The methods developed here use the full pixel-level resolution of the satellite observations at hourly time intervals. The cloud detection algorithm for both satellites is a simplified version of the Coupled Cloud and Snow Detection Algorithm (CCSDA) developed at the University of Maryland (Li et al. 2007; Pinker et al. 2007). The original algorithm employs one spatial variability test and seven spectral threshold tests using combinations of four channels of data from *GOES-8*, centered at 0.75, 3.9, 10.6, and 11.9 microns. The tests are adapted from the Clouds for AVHRR (CLAVR) cloud detection algorithm for the AVHRR sensor onboard the NOAA polar orbiting satellites (Stowe et al. 1999), and concepts from the MODIS cloud mask (Ackerman et al. 1998) that was developed for the *Terra* and *Aqua* satellite missions. Table 2.1 shows all of the tests that have been developed for the CCSDA and the channels used to employ each test. Meteosat has three channels centered at 0.75, 6.9, and 11.5 microns. Without an additional IR channel comparable to the 10.6 channel of GOES, some of the tests cannot be applied.

Meteosat data are collected at a resolution of 2.5 km in the visible channel and 5 km in the IR channel. In all of the tests, the visible data are reduced to 5 km to match the IR, and cloud tests are applied to 2 x 2 pixel squares. The Reflectance

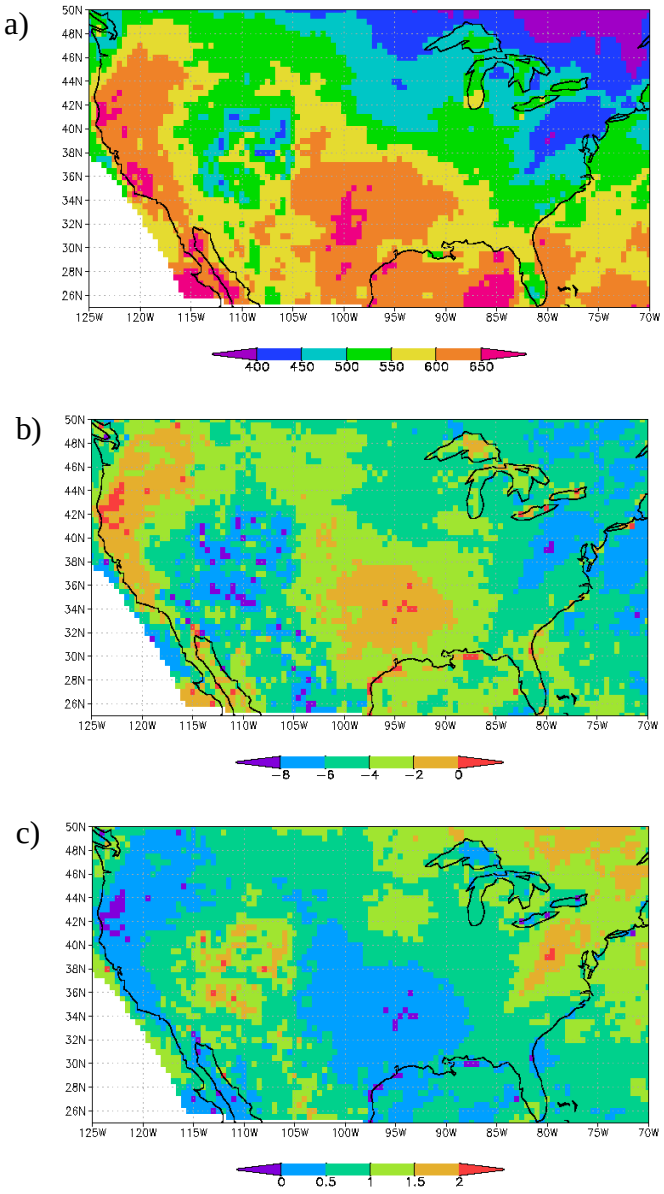

Figure 2.1. (a) Average of the NOAA and NASA monthly mean surface SW downward fluxes (Wm^{-2}) for Aug 2000 (b) difference between monthly mean surface SW downward flux (Wm^{-2}) calculated with NASA and NOAA calibrations for Aug 2000 (c) as in (b), but normalized by the average of the NOAA and NASA surface SW downward fluxes.

Table 2.2. Comparison of cloud tests used in cloud detection process for GOES vs. Meteosat processing.

Cloud Test	CCSDA	Met
Reflectance Gross Contrast Test (Visible)	X	X
Thermal Gross Contrast Test (11 micron)	X	X
Near-IR Reflectance Test (4 micron)	X	
Uniform Low Stratus Test (4 - 11 micron)	X	
Cirrus Test (4 – 11 micron)	X	
Four Minus Five Test (11 –12 micron)	X	
Two Minus Four Test (4 - 11 micron)	X	
Reflectance Uniformity Test (Visible)	X	X

Gross Contrast Test (RGCT) compares the visible reflectance of each pixel to an empirically-derived reflectance threshold set to 30 over the ocean and 44 over land. The theoretical basis for this test is that clouds will be more reflective than the background that would be seen from space. Pixels with reflectances higher than the threshold values are classified as cloudy. Since snow-covered backgrounds have high reflectances that can be mistaken for clouds, this test is turned off when snow is present, as determined by the Interactive Multi-sensor Snow and Ice Mapping System (IMS) data set, a manually developed global snow mask produced at the National Centers for Environmental Prediction (NCEP) (Ramsay 1998; NOAA/NESDIS/OSDPD/SSD 2004).

The Thermal Gross Contrast Test (TGCT) uses the 11.5 μm IR brightness temperature (the temperature a black body would have if emitting the same amount of radiation at the same wavelength) sensed by the satellite. Pixels are classified as cloudy if their IR brightness temperatures are colder than threshold values set to 271 K for *Meteosat-5* over water (269 K for *Meteosat-7* over water) and 249 K over land

for both satellites. The different water thresholds were arrived upon through visual inspection of cloud analyses in comparison to satellite images. This test works well as a supplement to the RGCT during daylight hours, but it is difficult to obtain a quality cloud analysis at night using only the TGCT. The prime objective of developing the cloud detection methodology is to use the cloud mask to derive solar radiation budgets and study the effect of aerosols on the budgets. Since these processes are only of interest during daylight hours, the effort has not been made at this time to develop a robust nighttime cloud detection algorithm. A pixel is considered to be under daytime conditions when its SZA is less than 75°. This threshold was conservatively chosen based on previous investigations of cloud retrievals at low sun angle that showed skill in cloud detection through SZA < 80° (d'Entremont and Gustafson 2006; Dybbroe 2001).

The Reflectance Uniformity Test (RUT) examines the range of reflectances in the 2 x 2 pixel square and compares it to reflectance uniformity thresholds for cloudy and clear conditions. If the RGCT and TGCT tests detect clear conditions, but the difference in reflectances in the 2 x 2 square is more variable than what is expected under clear conditions, the pixels are flagged as mixed clear. Similarly, pixels identified as cloudy are tagged as mixed cloudy if the RUT difference is less variable than what is expected under cloudy conditions. The mixed pixels are then redistributed during the gridding process.

2.1.4. Gridding

Once the cloud classification has been performed at pixel level, the data are re-projected onto a latitude/longitude grid. The gridding process requires the

introduction of a clear-sky composite reflectance (CCR) to be used as a threshold in the reclassification of mixed pixels as either clear or cloudy. The CCR is computed for each pixel by averaging the reflectance values at each pixel for all clear-sky cases over the course of a month. A separate CCR is calculated for each hour of the day to account for variations in bi-directional reflectance. To make the final clear or cloudy determination for pixels flagged as mixed with the individual cloud tests, the reflectances of the mixed pixels in the grid box are compared to two values: the CCR and an empirically-determined cloudy threshold. Mixed pixels with reflectance values less than or close to the CCR value are flagged as clear and mixed pixels with reflectance values larger than or close to the cloudy threshold are flagged as cloudy. The final cloud amount is calculated as the number of cloudy pixels in a grid box divided by the total number of pixels in the grid box. Other variables provided in the gridded projection include clear-sky reflectance, cloudy reflectance, snow amount, and CCR. The resolution of the final gridded product can be selected during the gridding process, and for the purposes of this research it has been set to 0.125°.

2.1.5. Cloud typing

Meteosat observations of 11.5 μm brightness temperature are used to differentiate between low and high clouds. Low clouds have cloud top temperatures > 263 K; clouds with temperatures < 250 K are classified as high clouds following Roca et al. (2005), who found that a threshold of 255 K encompasses the majority of convection-induced high clouds. The cloud classification procedure from MODIS uses multiple spectral bands, but case studies show that the 11 – 12 μm channel brightness temperatures for low, middle, and high clouds generally fall into the ranges

given above (Li et al. 2003). To differentiate between upper-level cloudiness and convection, convective clouds must meet the high cloud temperature threshold and have an optical depth ≥ 23. The optical depth criterion was chosen following the ISCCP algorithm used by Rossow and Schiffer (1991) to identify convective clouds. Cloud optical depth is estimated with the University of Maryland Surface Radiation Budget (UMD_SRB) model (Pinker et al. 2003), which is discussed in the next section.

2.2. Description of the radiative flux inference scheme

The radiative flux inference scheme used in this work is an outgrowth of the University of Maryland Surface Radiation Budget (UMD_SRB) model, as implemented operationally at the National Oceanic and Atmospheric Administration (NOAA)/National Environmental Satellite Data and Information Service (NESDIS) using observations from GOES satellites. The scheme estimates both surface and top of the atmosphere (TOA) upward and downward fluxes in five spectral intervals (0.2–0.4, 0.4–0.5, 0.5–0.6, 0.6–0.7, and 0.7–4.0 μm) and aggregates them into the following climatically relevant intervals: shortwave, photosynthetically active radiation, and near-IR. Flux output is further broken down into clear-sky and all-sky as well as direct and diffuse radiation.

Basics of the inference scheme are reviewed here; a more detailed discussion is presented in Pinker et al. (2003). The approach is based on the known relationship between 1) planetary TOA albedo (A_T, atmosphere plus surface reflection), 2) surface absorption of radiation (which is determined by the surface albedo) and, 3) flux

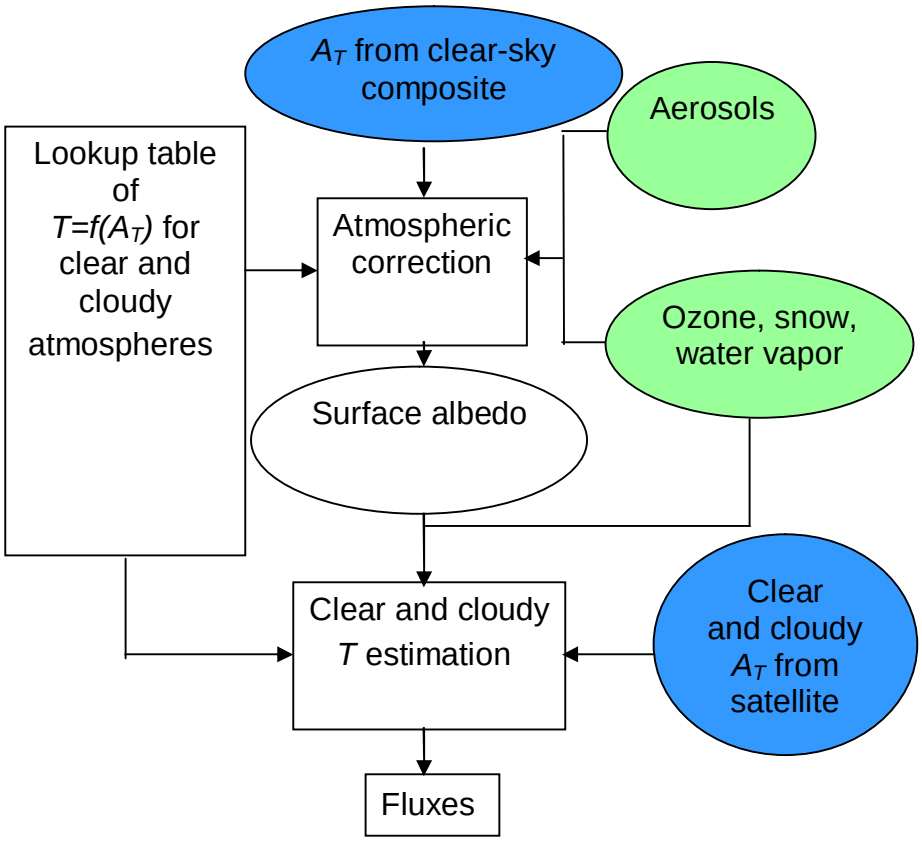

Figure 2.2. Flowchart of radiative flux inference scheme. Cloud inputs are shown in blue and auxiliary inputs are shown in green.

transmittance (T, the fraction of radiation that arrives at the surface after interaction with the atmosphere). The relationship is prescribed by the adding equation of radiative transfer over a vertically inhomogeneous, semi-Lambertian surface. The flux transmittance is required for two stages of the radiative flux inference scheme, as shown in Figure 2.2. First, it is used in combination with the satellite-derived clear-sky composite radiance (the average radiance under clear-sky conditions for about one month) to estimate the surface albedo. Second, it is used in the calculations of upward and downward radiative fluxes to account for extinction of radiation due to atmospheric effects. The flux transmittance has a dependence on the surface albedo, and the surface albedo is influenced by the flux transmittance. Therefore, both

variables cannot be derived simultaneously from the satellite information alone. The model approach is to first make assumptions on the flux transmittance (which is dependent on the water vapor, ozone, and aerosol content of the atmosphere), in order to derive the surface albedo. Once the surface albedo is obtained it is used as the boundary condition to retrieve cloud or aerosol optical depth estimates (for cloudy and clear-sky cases, respectively) from each individual grid point. This is accomplished by calculating a modeled value of TOA broadband albedo for various values of cloud and aerosol optical depths. Next, the satellite-observed TOA albedo is compared to the modeled values, and the appropriate cloud or aerosol optical depth is selected based on the closest match between modeled and observed TOA albedo.

To determine the flux transmittance for calculation of the surface albedo, the model relies on look-up tables (LUTs) of atmospheric reflectivity and transmissivity that are stratified by solar zenith angle (SZA) as well as the water vapor, ozone, and aerosol content of the atmosphere. The LUT values are developed from radiative transfer calculations using the ATRAD2 model (Wiscombe et al.1984; Laszlo et al. 1988; Halthore et al. 2005). Auxiliary inputs of water vapor, ozone, and aerosols are needed to select the proper reflectivity and transmissivity values from the LUTs. Water vapor inputs come from the NCEP/NCAR Re-analysis while season- and latitude-dependent ozone amounts are taken from the McClatchy atmospheres (F. X. Kneizys et al., unpublished data, 1988). At the time of development of the UMD_SRB model, available aerosol information was limited. Accordingly, aerosol treatment in the operational model is fairly simplistic. AOD is assumed to be 0.23 over land and 0.128 over water, per the Standard Radiation Atmospheres [WCP-55,

1983]. Improved aerosol information is now available from several satellite sources including MODIS (Kaufman et al. 1997), MISR (Bothwell et al. 2002), and POLDER (Leroy et al. 1997; Mukai and Sano, 1999). Additionally, the Aerosol Robotic Network (AERONET) (Holben et al. 1998, 2001) has expanded to provide ground-based estimates of radiative flux parameters at over 600 locations. Aerosols play a large role in the radiation budgets of both the Indian and African monsoon regions. Therefore, as part of the transferability effort, two research versions of the model have been developed to incorporate different methods of handling aerosols. Full details of the aerosol sensitivity tests conducted with the research versions are given in Chapter 5.

Improvement of flux retrieval at high elevations also needed to be addressed, particularly for the Tibetan Plateau in the Southeast Asian monsoon region with elevations ranging from 4000 to over 6000 m. Elevated terrain poses a problem for radiative flux retrievals from satellite observations. Total column ozone and water vapor amounts are generally lower above elevated surfaces due to the shorter distance from surface to TOA. The LUTs of atmospheric reflectance and transmittance are based on calculations that assume water vapor and ozone amounts are measured from an elevation of zero. In the research models, an elevation correction is applied to account for this. At mountainous points, the atmosphere is treated as two layers. The top layer represents the atmosphere above the mountain and the bottom is the "mountain" layer. In the first part of the elevation correction, water vapor and ozone amounts are increased by the amount that would be present if the "mountain" layer was replaced by one of five standard atmospheres (tropical, mid-latitude summer,

mid-latitude winter, sub-Arctic summer and sub-Arctic winter) based on location and season. This brings the real atmosphere closer to the model atmosphere which assumes the surface height to be zero. The reflectance and transmittance values chosen from the table using corrected water vapor and ozone amounts are used to calculate the modeled planetary albedos that are matched to the observed broadband albedo to retrieve the aerosol or cloud optical depth (depending on whether the grid point is clear or cloudy). Before calculating the modeled planetary albedos, the reflectance and transmittance due to the "mountain" layer are subtracted from the total values so the only contribution comes from the upper layer (Y. Ma, personal communication).

The impact of this elevation correction (along with the high spatial resolution of the model) is seen in an independent evaluation of surface SW downward fluxes derived over the Tibetan Plateau using a research version of the UMD_SRB model (UMD_SRB-R) with inputs from *Meteosat-5* (Yang et al. 2008). In this region, shading by mountain peaks causes high variability in radiative flux fields and orographic effects produce small-scale variations in the cloud fields that cannot be resolved by many of the currently available cloud products. Liou et al. (2007) showed that average radiative flux over complex terrain may vary by 10 – 50 Wm^{-2} in comparison to fluxes over flat surfaces. The study uses ground observations of surface SW radiative flux obtained at 9 sites with elevations higher than 4000 MSL to validate fluxes retrieved from the UMD_SRB-R model along with flux products from two other radiative flux inference schemes. The first is the ISCCP-FD product, derived with the ISCCP model run by the NASA Goddard Institute for Space Studies

(GISS) using ISCCP D1 cloud input. The second is the GEWEX Surface Radiation Budget model (GEWEX/SRB) as implemented by the NASA Langley Research Center with ISCCP D1 cloud input. Both ISCCP-FD and GEWEX/SRB use cloud inputs that are sub-sampled at 30 km and 3-hour resolution. The final resolution of the ISCCP-FD and GEWEX/SRB radiative flux products are 2.5° and 1°, respectively.

As seen in Table 3.1, the ISCCP-FD and GEWEX/SRB models underestimate surface SW radiative flux at all sites while the fluxes retrieved with the UMD_SRB-R model are much closer to the observed values. To minimize the advantage of the higher spatial resolution of UMD_SRB-R in the statistical comparison, biases were also calculated after upscaling the high resolution data to 1.0° and 2.5° to match the resolution of the other products. The resulting biases were 0.3 Wm^{-2} and -4.0 Wm^{-2}, respectively.

On daily timescale the standard deviation of the errors is smaller for UMD_SRB-R, but ISCCP-FD and GEWEX/SRB perform better at 3-hourly timescale. This behavior is attributed to the nature of clouds in the Tibetan Plateau, which is dominated by fast-moving convective cells with spatial scale of a few kilometers (Yeh and Gao, 1979). As a result, the quality of radiative fluxes produced by the UMD_SRB-R model undergoes a progression from high accuracy of instantaneous fluxes, degraded accuracy at hourly time scales due to the rapidly changing cloud conditions, and a return to greater accuracy at longer time scales when the hourly variability averages out.

Table 2.3. Evaluation of ISCCP-FD, GEWEX/SRB, and UMD_SRB-R surface SW downward radiative fluxes against ground observations in the Tibetan Plateau for Jul – Sep 1998.

Site	SQH	Gerze	MS 3637	Naqu	MS 3478	Anduo	D110	TTH	D66	Ave
Observed mean value										
	293.6	268.5	235.2	237.2	240.8	243.4	259.5	257.2	256.3	254.6
Mean bias error										
ISCCP-FD	-11.9	-16.7	-12.1	-10.3	-9.6	-17.1	-10.0	-15.7	-3.8	-11.9
GEWEX/SRB	-10.2	-13.3	-15.5	-29.5	-12.9	-6.3	-32.2	-19.1	-9.4	-16.5
UMD-SRB-R	-0.1	-14.5	12.7	-0.8	0.8	9.3	-3.1	-5.6	-6.7	-0.9
Standard deviation of the differences between *3hr-mean* observation and satellite product										
ISCCP-FD	83.6	77.9	89.1	83.3	99.2	101.7	102.9	83.9	90.6	90.2
GEWEX/SRB	57.4	59.1	94.5	95.5	102.2	78.7	100.5	88.3	95.3	85.7
UMD-SRB-R	82.3	83.0	95.8	89.4	109.2	87.6	101.3	91.3	89.3	92.1
Standard deviation of the differences between *daily-mean* observation and satellite product										
ISCCP-FD	41.9	34.4	34	30.3	45.7	45.5	42.3	34.6	37.8	38.5
GEWEX/SRB	23.6	25.4	36.6	33.4	42.4	29.8	41.4	35.1	39.9	34.2
UMD-SRB-R	25.8	32.2	45	36	35.7	30.3	31.8	25.3	29.5	32.4

Chapter 3: Indian Monsoon Cloud Climatology

3.1. Background

Predicting the onset, intensity, and intra-seasonal variation of the Indian monsoon continues to be a challenge, in part due to problems with representing clouds, convection, and their diurnal cycle in numerical models. A clear understanding of these parameters is essential for model assessment and improvement. The CEOP program emphasizes the need to document the advance and withdrawal of the monsoons as a basis for understanding their driving mechanisms (http://monsoon.t.u-tokyo.ac.jp/ceop/objectives.html). Cloud distributions in the Indian monsoon region, particularly at diurnal time scales, are not well documented due to the lack of coverage by geostationary satellites until 1998. Prior to that year, geostationary coverage of the region was provided by the Indian National Satellite (INSAT) and the Japanese Geosynchronous Meteorological Satellite (GMS). However, these data sources have limited usefulness in the Indian monsoon region. The Indian Meteorological Department has not made the entire record of INSAT data publicly available. Only a subset is distributed through the National Center for Atmospheric Research (NCAR) (Roca et al. 2005) for a five-year period with only about two frames per day. The GMS series is not the ideal data source as India is on the western limb of the satellite's field-of-view.

The lack of geostationary satellite coverage of the Indian monsoon region is readily apparent in cloud analyses produced by ISCCP. This database suffered for most of its duration from what is known as the "Indian Ocean Gap", a region where only NOAA AVHRR morning and afternoon satellite observations are available. This

greatly reduced the number of observations of cloudiness in the region (Figure 3.1) and clustered the time of the observations to only two daytime hours, one daytime observation per NOAA satellite. In support of INDOEX (Ramanathan et al. 2001), the *Meteosat-5* satellite was moved to 63° E longitude, and continuous operational coverage of the area began in July 1998. *Meteosat-5* observations over India have been incorporated into the ISCCP data set since 1998, yet it does not exploit the full capabilities of the *Meteosat-5* data since they undergo spatial and temporal sub-sampling of 30 km and 3 hours, respectively.

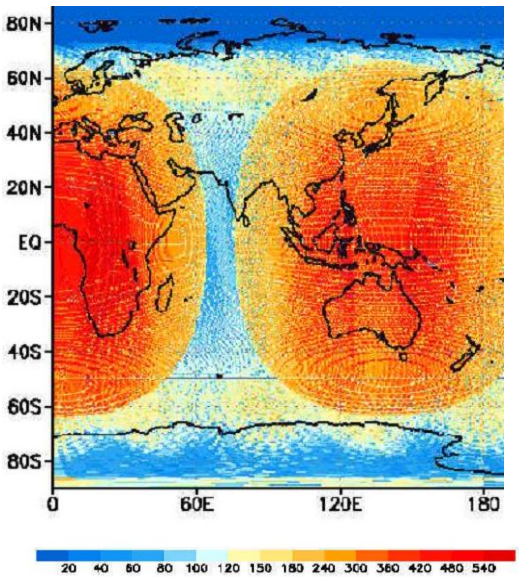

Figure 3.1. Frequency distribution of the number of observations available for the ISCCP D1 dataset for the month of October 1996.

The focus of this chapter is to improve on previous cloud climatologies of the Indian monsoon region by applying the cloud detection algorithm described in Chapter 2 using the full (hourly) temporal resolution and 5-km spatial resolution of *Meteosat-5* observations to characterize cloud variability on seasonal and diurnal

timescales over India, the surrounding waters, and the Tibetan Plateau. Emphasis is placed on how the patterns change as the monsoon evolves through the pre-monsoon (March – May), peak-monsoon (June – September), and post-monsoon (October – November) seasons.

After spatial patterns of clouds for the various seasons are presented, the diurnal cycles of clouds and convection are addressed. Information on the diurnal cycle is valuable since some of the most fundamental processes are those associated with the diurnal cycle, and as such, can facilitate improvements in numerical model physics. Accurate prediction of the diurnal cycle of clouds is considered to be a prerequisite for improved forecasts on seasonal and longer time scales (Lau et al. 2005). Moreover, Randall et al. (1991) noted that testing a model's ability to simulate the diurnal cycle can be accomplished with a short integration of the model, and yields insights into model deficiencies without the computational, time, and storage expenses required for longer integrations.

The years 2001 and 2003 are chosen for analysis. These are years with climatologically normal rainfall (Figure 3.2) based on rain gauge observations as available from the Indian Institute of Tropical Meteorology (IITM) at Pune, (Parthasarathy et al. 1995). In most cases, only the results for 2001 are shown since the analyses for both years are quite similar.

3.2. Spatial variability of clouds

To document the progression of the monsoon, the mean total daytime cloud amount for the 2001 and 2003 pre-monsoon, peak-monsoon, and post-monsoon

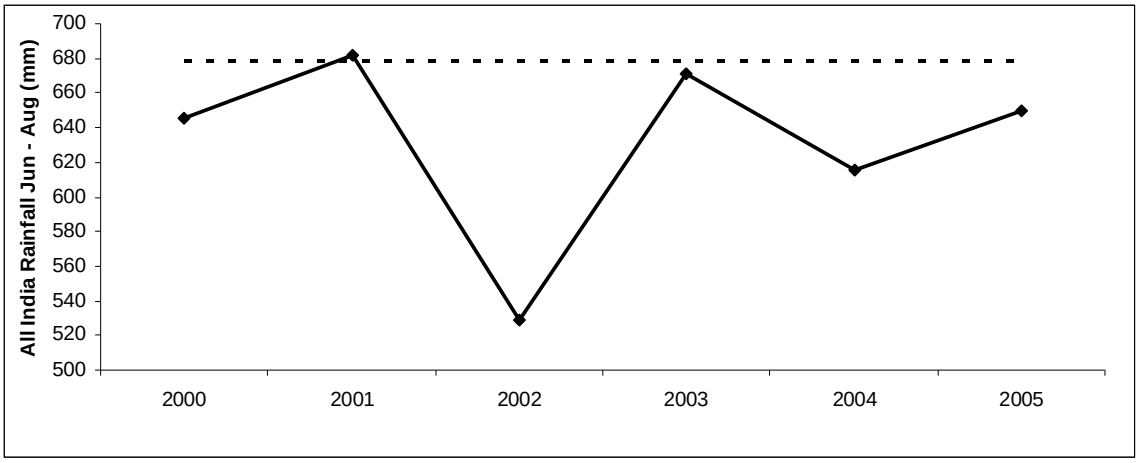

Figure 3.2. All-India monsoon rainfall for the years 2000 – 2005 as derived from rain gauge data compiled by the IITM. Dashed line represents the climatologically normal rainfall amount.

seasons are computed and are presented in Figure 3.3. In the pre-monsoon phase (Figure 3.3, top panels), the Indian subcontinent and surrounding oceans experience no more than 30% cloudiness. During the peak-monsoon months (Figure 3.3, middle panels) mean cloud amounts increase to 50 – 80% in northeastern India and the Arabian Sea, and up to 90% over a large portion of the northern Bay of Bengal. Northwestern India, however, does not experience a large increase in cloud cover. This may be explained by the fact that the monsoon wind flow is northwestward from the Bay of Bengal onto the subcontinent, and most of the moisture is depleted before reaching the northwestern region. An alternative explanation is that the region remains relatively cloud-free because the northward extent of the migration of the ITCZ is about 25° N. Post-monsoon cloud amounts (Figure 3.3, bottom panels) drop dramatically throughout most of the subcontinent. In 2001 it is particularly evident that cloudiness continues during this phase in the eastern portion of the southern peninsula, which typically receives most of its rainfall during the months of

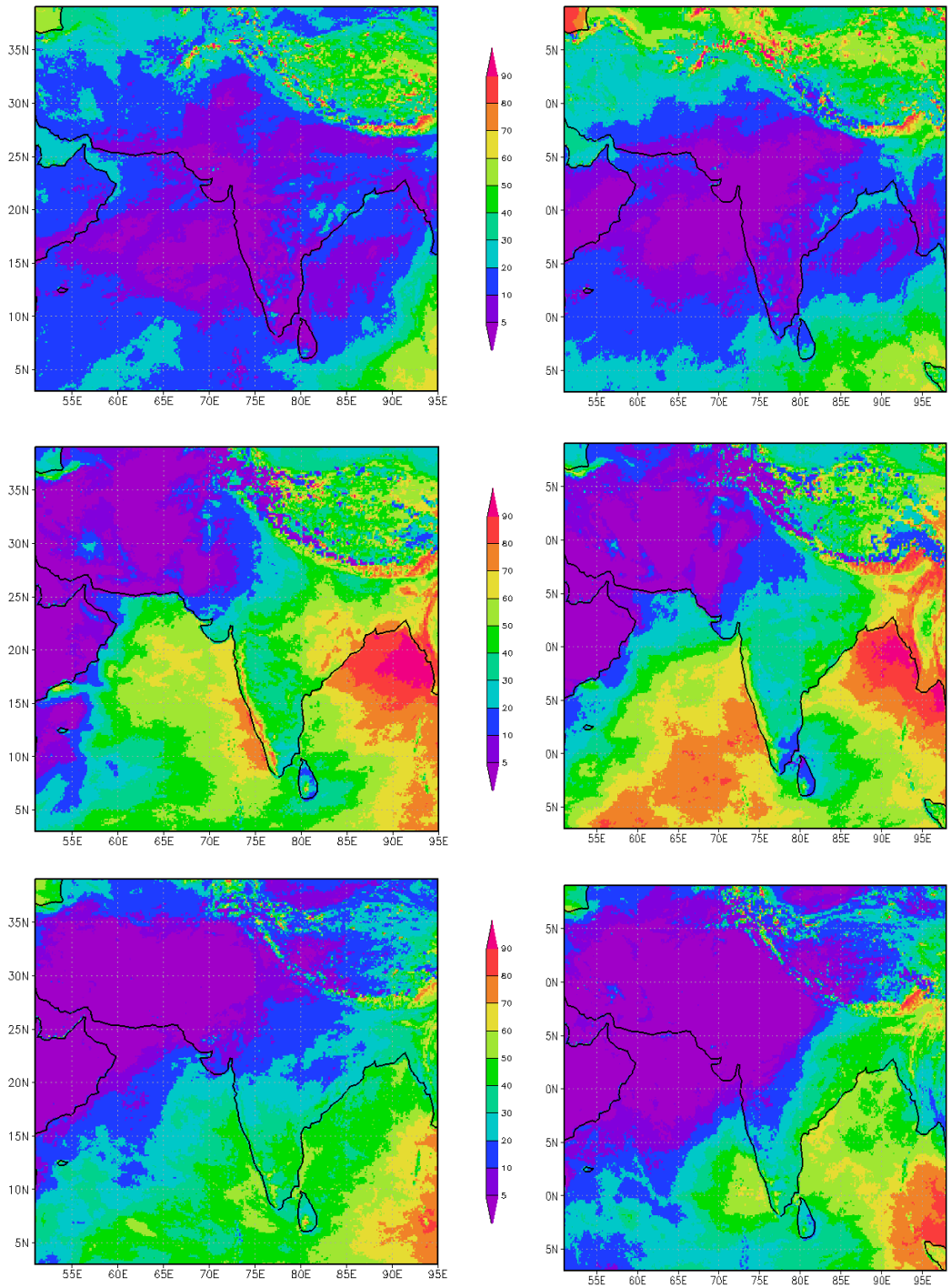

Figure 3.3. Average daytime cloud amount (%) for pre-monsoon (Mar – May, top panels), peak-monsoon (Jun – Sep, middle panels), and post-monsoon (Oct – Nov, bottom panels) seasons for 2001 (left) and 2003 (right).

October and November (Gadgil 2003). Regions of high cloud amount over water progress southward as the monsoon subsides.

Figure 3.4 shows the change in monthly mean total daytime cloud amount as the monsoon moves through different phases for the 2001 season. During the monsoon build-up from May into June (Figure 3.4a), the maximum increase in cloudiness occurs in latitudes 10° N – 20° N. At the height of the monsoon (July into August, Figure 3.4b), the zone of maximum increase in cloudiness pushes to 25° N, and then drops to 5° N – 15° N during the monsoon dissipation phase (September into October, Figure 3.4c).

3.3. Diurnal variation of clouds and convection

Previous studies to depict the diurnal cycle of clouds and precipitation over the Indian monsoon region have used various sources of information. Yang and Slingo (2001) used the European Union Cloud Archive User Service data set to infer clouds from 11-12 μm brightness temperature. This data set is based on the ISCCP B3 data with spatial resolution of 0.5° sampled at 30 km and temporal resolution of 3 hours. For the period of the study, only polar orbiter data are included in the ISCCP data over India, so the diurnal cycle is not well-represented in this region. Roca and Ramanathan (2000) reported on the diurnal variation of convective clouds based on cloud size, as derived from 3-hourly INSAT 10.5 – 12.5 μm data. Their study focused mainly on clouds during the winter monsoon season. Sorooshian et al. (2002) evaluated convection over the Bay of Bengal and Calcutta from microwave and radar measurements of rainfall from the *TRMM* satellite. Janowiak et al. (1994) used passive microwave data from the Special Sensor Microwave/Imager (SSM/I)

a)

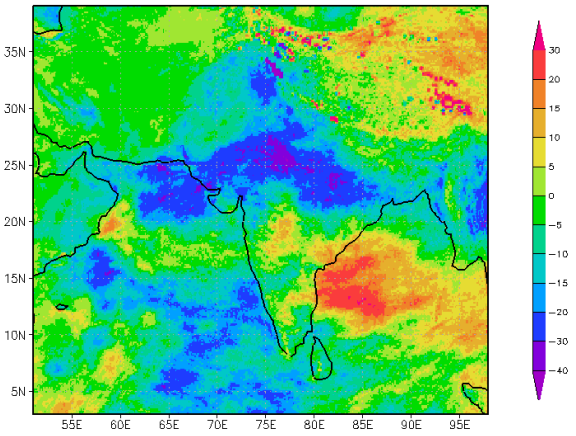

b)

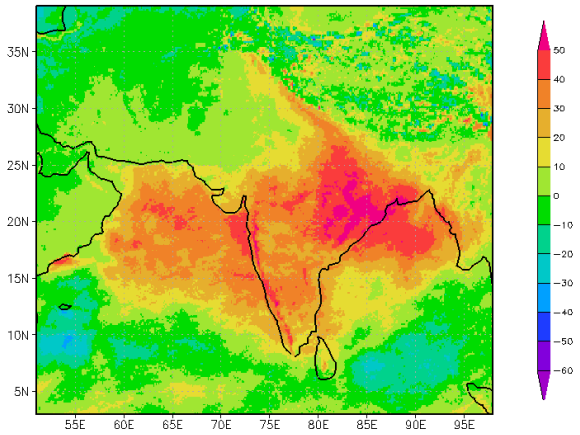

c)

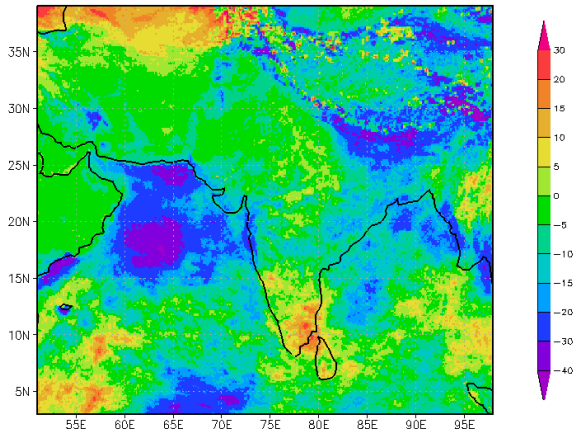

Figure 3.4. Difference in monthly mean cloud amounts (%) for daylight hours for a) June minus May 2001, b) August minus July 2001, c) October minus September 2001.

instrument onboard polar orbiting Defense Meteorological Satellite Program (DMSP) satellites to determine the diurnal cycle of rainfall. Diurnal characteristics were inferred by using several DMSP satellites with different nodal crossing times for a total of six observations per day with a gap from 0930 to 1710 Local Standard Time (LST). Islam et al. (2004) tracked the diurnal cycle of clouds and precipitation in Bangladesh and a small part of the Bay of Bengal with IR brightness temperature data from the Japanese *GMS-5* and radar data from the Bangladesh Meteorological Department. Sen Roy and Balling (2007) examined data from 78 land-based rain gauges over the Indian subcontinent for the summers of 1980 – 2000. A few studies have employed *Meteosat-5* in a different context than the current study. Zuidema (2003) contrasted convection in the Bay of Bengal for two years based on IR brightness temperatures from *INSAT* in 1988 and *Meteosat-5* in 1999. Krishnamurti and Kishtawal (2000) and Barros et al. (2004) used a combination of *Meteosat-5* IR brightness temperature data along with rainfall observations from *TRMM* for studies of convection in the Asian monsoon region. The former study focused solely on a break period of the monsoon to detect a diurnal mode of convection, and did not address monsoon characteristics. The latter investigation concentrated on convection patterns in the Tibetan Plateau, Himalayas, and Ganges Basin.

The current study adds to these results in several ways. It offers a new cloud detection algorithm that incorporates visible satellite imagery along with brightness temperature information and exploits the high temporal resolution of *Meteosat-5*. It encompasses a large area and contrasts the behavior of clouds in different parts of the monsoon region. Finally, it aggregates cloud observations in terms of pre-monsoon,

peak-monsoon, and post-monsoon time frames to better understand the evolution of cloud patterns as the monsoon progresses.

3.3.1. Daytime diurnal cycle of clouds

The amplitude of the daytime diurnal cycle of low clouds and high clouds is shown in Figure 3.5. The amplitude is defined as the difference between the maximum and minimum percentage of cloud amount for daylight hours for each day, averaged over the pre-monsoon, peak-monsoon, and post-monsoon seasons of 2003. The low and high cloud classifications are based on cloud top temperature as seen from the satellite. As such, a high cloud classification does not preclude the presence of low clouds underneath, or a low cloud base as in the case of deep convective clouds.

In the pre-monsoon season (top panels) cloud fraction is low throughout the region and there is very little diurnal variation in low cloud amount (Figure 3.5a). The exception is just north of the Bay of Bengal, where moisture from southerly flow over the bay condenses when it encounters the Himalaya range, leading to a stronger diurnal cycle. There is more diurnal variability in high clouds over the southern peninsula and the Tibetan Plateau (Figure 3.5b). Over oceans, the amplitude of the diurnal cycle of high clouds is much smaller, in agreement with Bergman and Salby (1996), who found a nearly uniform diurnal cycle of tropical oceanic convection.

In the peak-monsoon season (middle panels) low cloud diurnal variability increases strongly over land with the northward push of monsoon clouds (Figure 3.5c). Despite the increase of convective clouds in the southern Arabian Sea, diurnal variability increases only slightly, as observed by Rozendaal et al. (1995) who

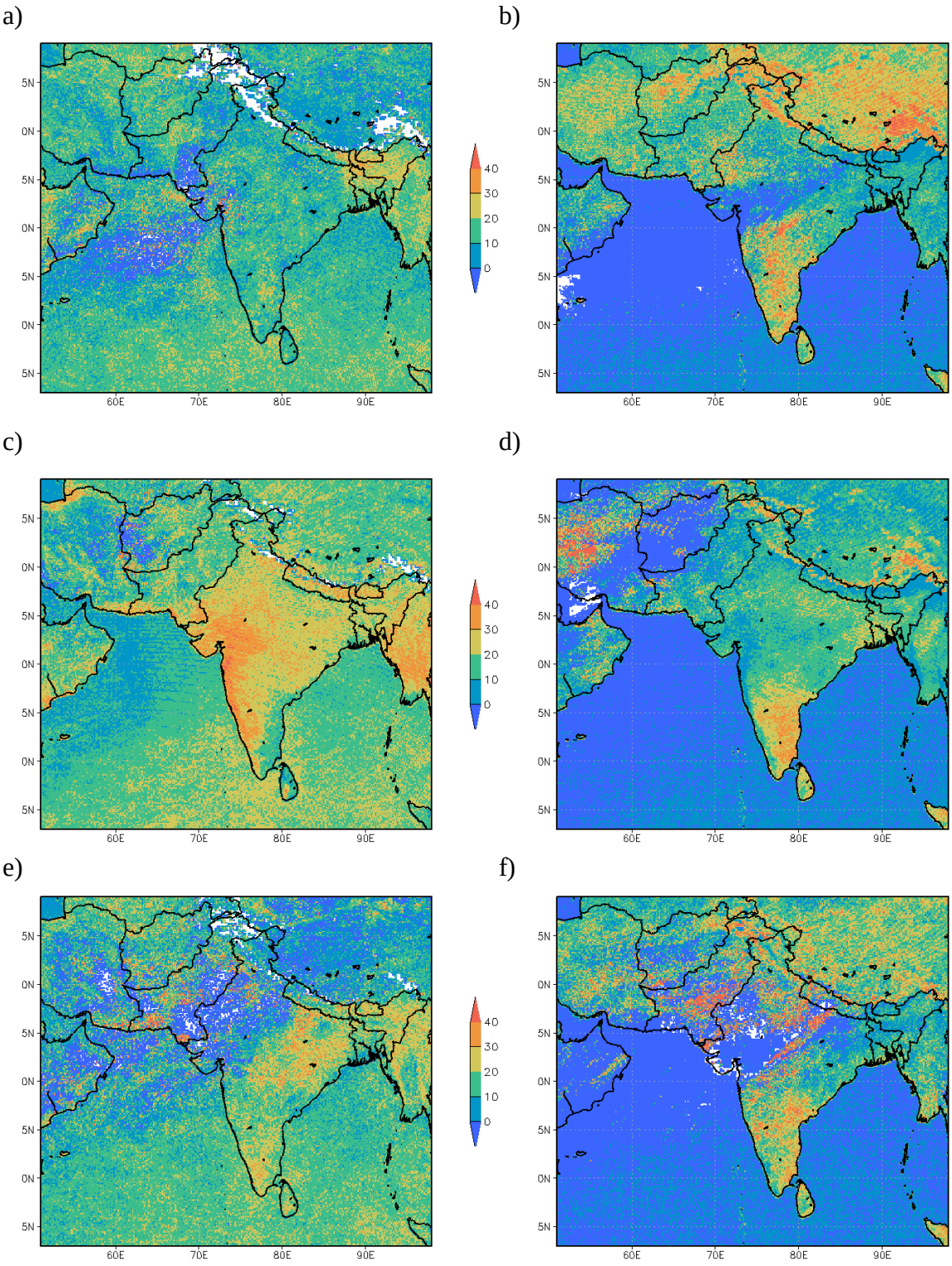

Figure 3.5. Amplitude of diurnal cycle of low cloud amount (left panels) and high cloud amount (right panels) averaged over the (a, b) pre-monsoon, (c, d) peak-monsoon, and (e, f) post-monsoon seasons.

showed that only non-convection marine low-level clouds exhibit large diurnal variability. High cloud amount becomes more variable in northern India but is reduced sharply over the Tibetan Plateau (Figure 3.5d). In the post-monsoon season (Figures 3.5e,f), diurnal variability is still high in the eastern part of the southern peninsula, which receives most of its annual rainfall in October, but the retreat of the monsoon is evident with a reduction in the amplitude of the diurnal cycle of clouds in the northern parts of the subcontinent.

To illustrate the variability of the diurnal cycle in different parts of the Indian monsoon region with emphasis on the times at which clouds most frequently occur, six points have been chosen for analysis (Figure 3.6). The points are chosen based on the location of the largest changes in cloud amount between the different monsoon

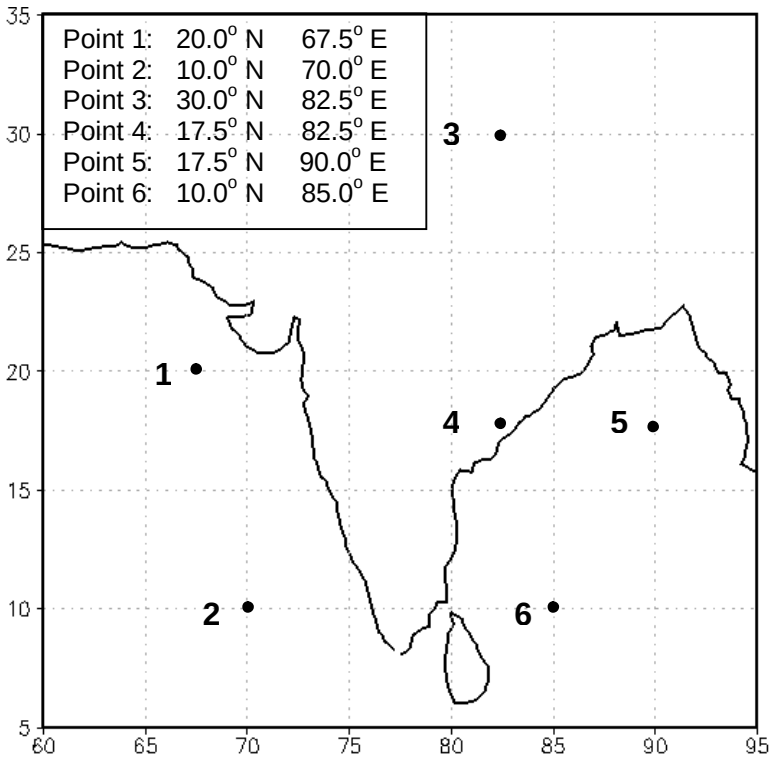

Figure 3.6. Location of data points used in analysis.

seasons (as shown in Figure 3.4) to capture the most dynamic cloud regimes. Figure 3.7 gives the mean total cloud amount at these points averaged over the 2001 (a) pre-monsoon, (b) peak-monsoon, and (c) post-monsoon season for hours 0800 – 1500 LST. In the pre-monsoon season the diurnal cycle is rather flat at most locations, although the northern Arabian Sea and both points in the Bay of Bengal display a morning maximum of clouds. In the peak-monsoon season, all points show a U-shape distribution, with diminishing cloud amounts in the middle of the day. A pronounced afternoon build-up of clouds is observed in the Tibetan Plateau. Afternoon cloudiness dominates at nearly every location in the post-monsoon season.

The breakdown of frequency of occurrence of low clouds (left column) and high clouds (right column) is given in Figure 3.8 for the 2001 pre-monsoon (top row), peak-monsoon (middle row), and post-monsoon (bottom row) seasons. There are several notable features of the distributions. The northern Arabian Sea is dominated by low clouds in the peak-monsoon season, indicating that although the northward progression of the monsoon brings an increase in cloud cover to the region, it is not of a convective nature. These clouds have maximum frequency in the morning. Alternatively, the southern Arabian Sea has more high cloud cover than low during both the pre- and peak- monsoon seasons and there is little diurnal variability for either type. Cloud behavior in the southern Bay of Bengal is quite similar to the southern Arabian Sea. For all seasons, the Tibetan Plateau is dominated by low clouds which peak in the afternoon. In coastal India and the northern Bay of Bengal, the diurnal cycle of low clouds is relatively flat for the pre-and peak-monsoon

a)

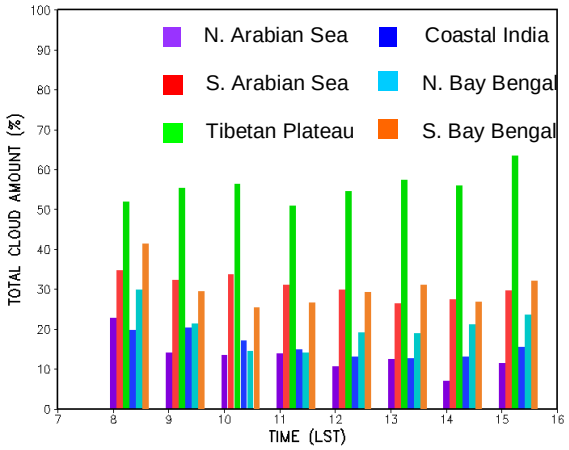

b)

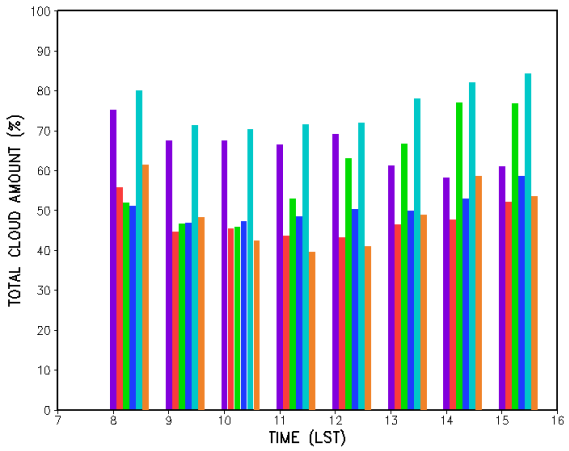

c)

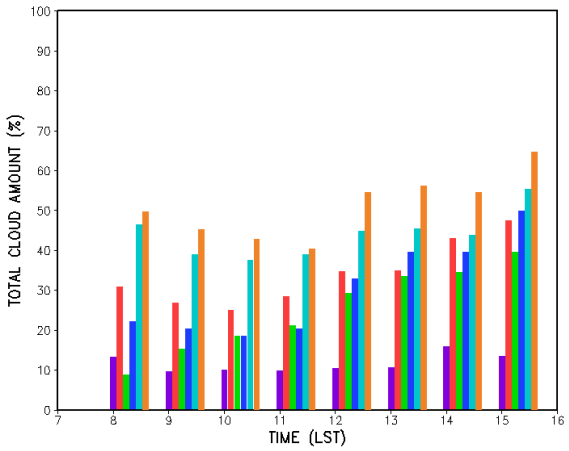

Figure 3.7. Diurnal variation of total cloud amount (%) for a) pre-monsoon (Mar – May), b) peak-monsoon (Jun – Sep), and c) post-monsoon (Oct – Nov) season 2001 for the hours of 8 – 15 LST for points shown in Figure 3.6.

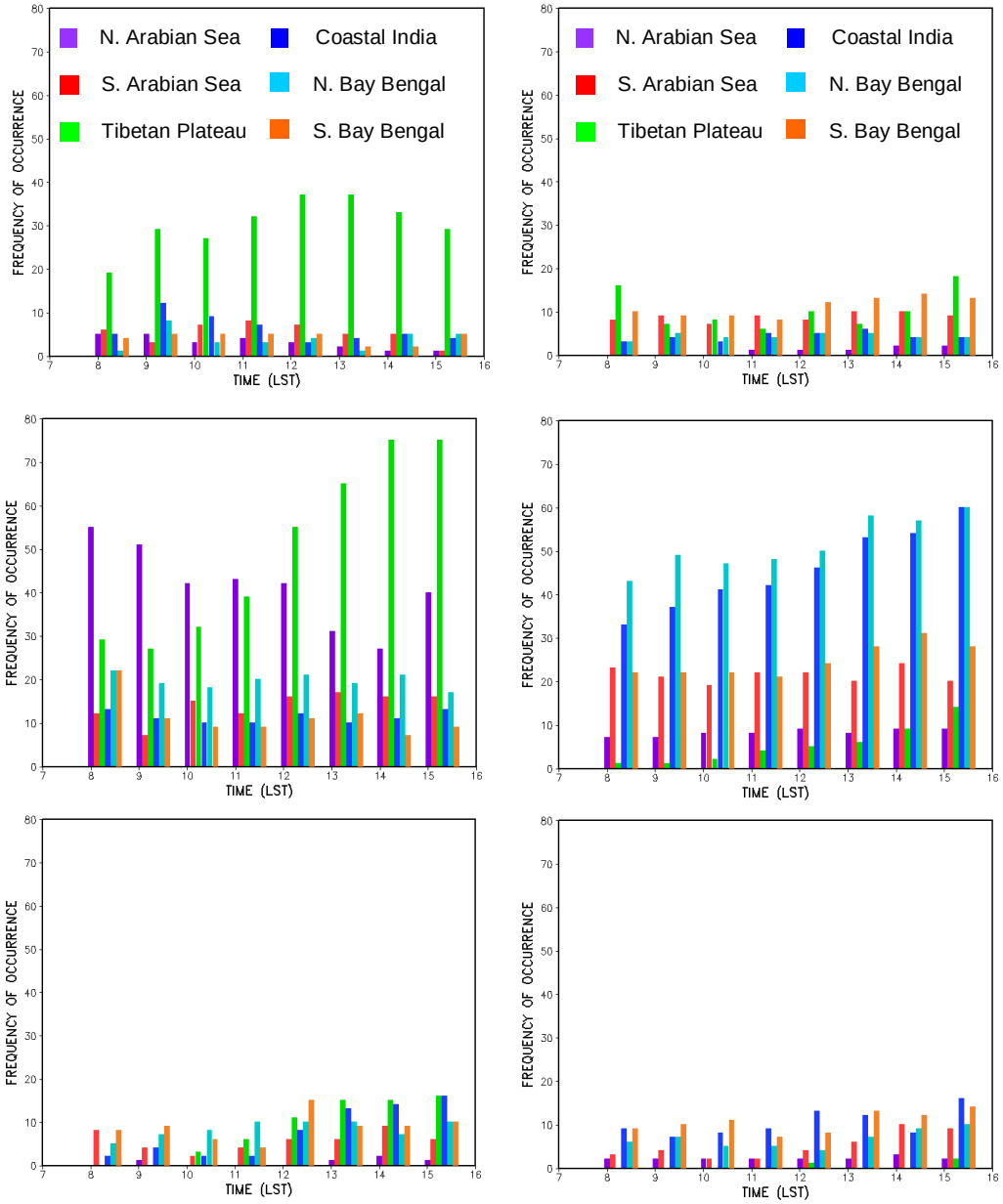

Figure 3.8. Diurnal variation of frequency of occurrence of low cloud (left column) and high cloud (right column) for pre-monsoon (Mar – May; top row), peak-monsoon (Jun – Sep; middle row), and post-monsoon (Oct – Nov; bottom row) season 2001 for the hours of 8 – 15 LST for points shown in Figure 3.6.

seasons, with a slight increase in afternoon low clouds during the post-monsoon season. The only noticeable diurnal signal in high clouds at these points occurs with the afternoon build-up of convective clouds during the peak of the monsoon.

3.3.2. Daytime diurnal cycle of convection

Since the majority of the monsoon rainfall is linked to convection, it is beneficial to analyze convective clouds separately from the total cloud amounts. Figure 3.9 shows the frequency of occurrence of convection for selected daytime hours throughout the Indian monsoon region during the peak-monsoon season 2001. The daytime diurnal maximum of convection occurs in the afternoon over both land and water, although the peak is earlier (1300 LST) at ocean points. The diurnal variation over the Bay of Bengal is consistent with the patterns reported in Zuidema's (2003) study of convection over the Bay during the 1998 and 1999 monsoon seasons. Many studies of the tropics as a whole agree that convection over land reaches a maximum in late afternoon (e.g. Gray and Jacobson 1977; McGarry and Reed 1978; Murakami 1983; Janowiak et al. 1994; Dai 2001; Gambheer and Bhat 2001; Nesbitt and Zipser 2003; Islam et al. 2004). The time of maximum frequency of convection for the analysis point in coastal India matches the value derived by Sen Roy and Balling (2007) using land-based rain gauges. An early morning maximum in tropical ocean convection has been reported by Sui et al. (1997), Yang and Slingo (2001), and Dai (2001). This is attributed to higher relative humidities and the nocturnal nature of meso-scale convective systems. Since the *Meteosat-5* observations analyzed in this

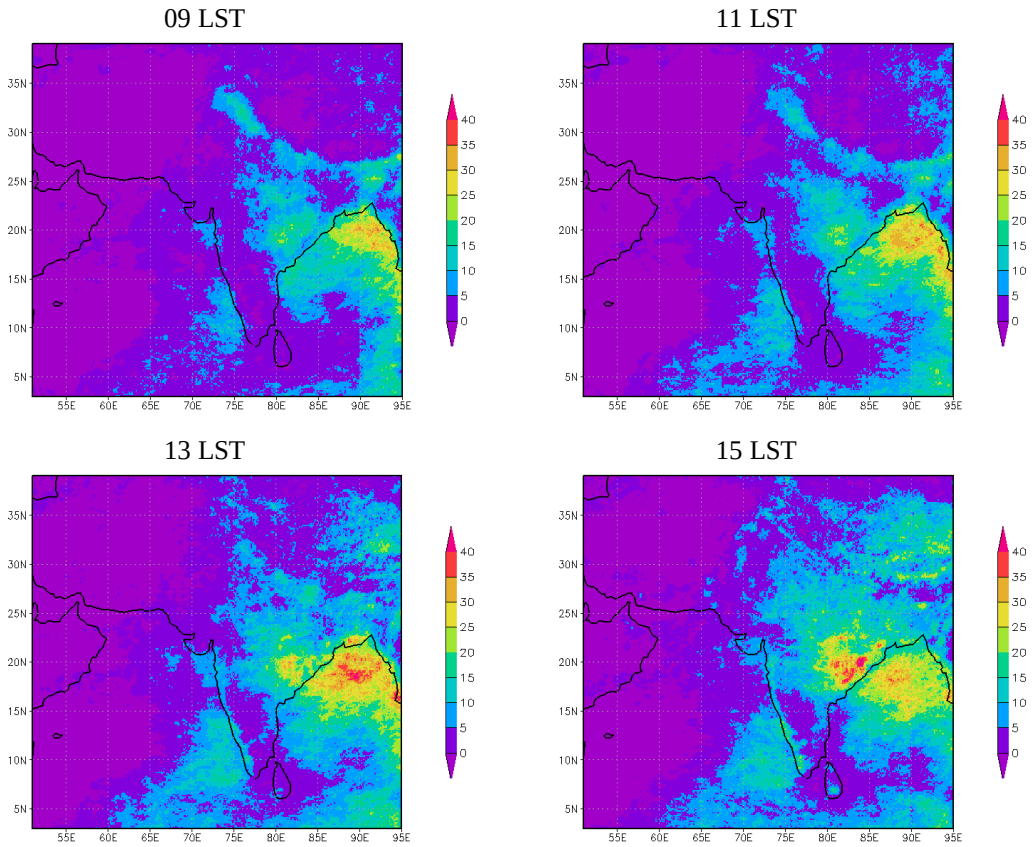

Figure 3.9. Frequency of occurrence of convective clouds at selected daytime hours for the peak-monsoon season (Jun – Sep) 2001.

study do not cover the non-daylight hours, this diurnal feature is neither confirmed nor contradicted. However, other studies do agree with the observed afternoon convective peak over tropical oceans seen here. Both ship and satellite data employed by McGarry and Reed (1978) in their study of the Global Atmospheric Research Program's (GARP) Atlantic Tropical Experiment (GATE) region yielded a convective cloudiness/rainfall maximum at 1400 LST, seemingly associated with large-scale convergence. Sorooshian et al. (2002) analyzed *TRMM* data in the Bay of Bengal and observed an extended period of convective rainfall that

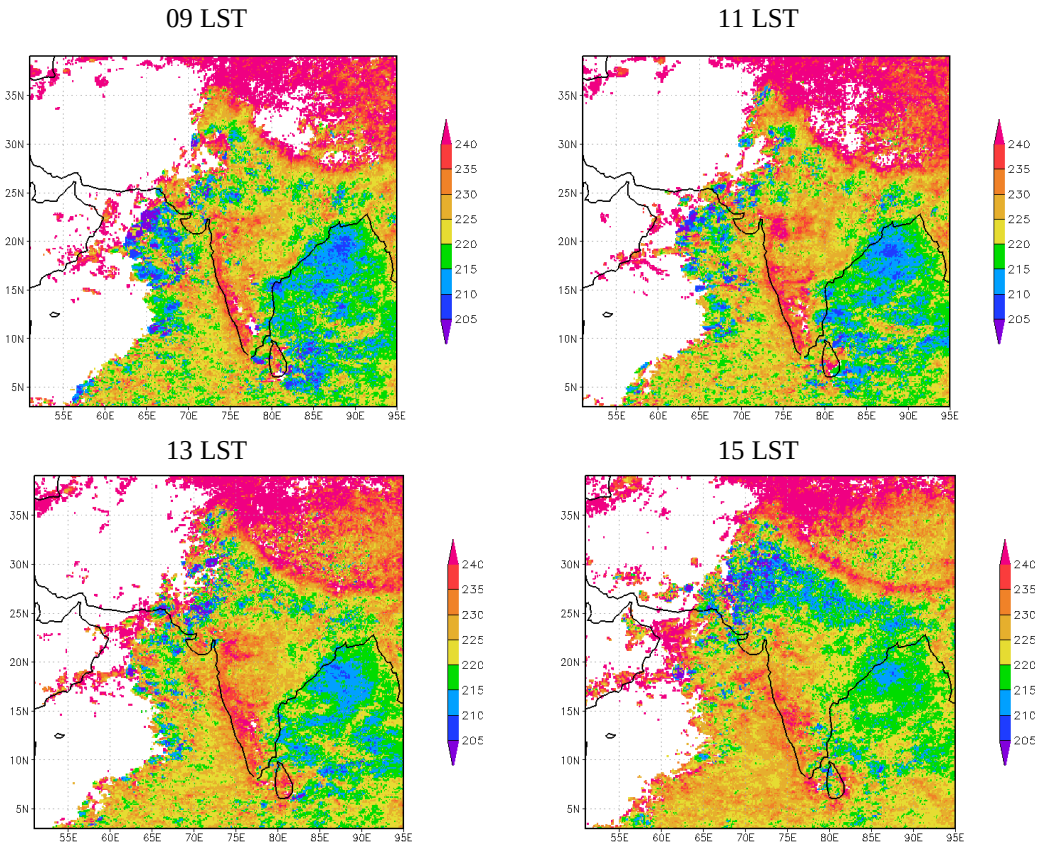

Figure 3.10. Mean temperature of convection (K) for selected daylight hours for peak-monsoon season (Jun –Sep) 2001.

began in early morning hours and reached its peak at 1400 LST, while Islam et al. (2004) found the maximum in the bay to occur between 1400-1600 LST. Gambheer and Bhat (2001) reported a peak in formation of new convective systems in the waters surrounding India between 15 and 24 LST. At the Tropical Ocean Global Atmosphere Coupled Ocean Atmosphere Response Experiment (TOGA COARE) observation site in the western Pacific, Sui et al. (1997) noted that the deepest convection displayed an early morning ocean maximum, but warmer convective clouds were most frequently observed in the afternoon due to the diurnal cycle in ocean skin temperature. These results were corroborated by Janowiak et al. (1994), who found that clouds with IR brightness temperatures > 235 K appeared mainly in

the afternoon. Figure 3.10 shows the mean temperature of convection averaged over the 2001 peak-monsoon season (for selected daytime hours). The main feature to note is that the coldest convection occurs in the earlier hours over ocean and in the later hours over land. This agrees with reports of the strongest ocean convection occurring in the early morning hours (not included in this study) and the conclusion that the secondary afternoon peak in ocean convection occurs within warmer cells.

3.4. Comparison to numerical model cloud analyses

The cloud information from *Meteosat-5* can be used to diagnose the shortcomings in numerical model cloud analyses. Numerical model representation of clouds impacts the physics that drive the monsoon rainfall predictions. Identifying errors in model cloud representation through validation with satellite-derived cloud information can lead to model improvement. Presented here are comparisons of Meteosat-derived total cloud amount over the Indian monsoon region versus two model sources: the ERA-40 Re-analysis (Uppala et al. 2005), are-analysis of the numerical weather prediction model run by the European Centre for Medium-Range Weather Forecasts (ECMWF), and the NCEP/NCAR Re-analysis (Kistler et al. 2000), a re-analysis of NCEP model data enhanced by assimilating other observational data sources.

Figure 3.11 shows an instantaneous picture of total cloud amount at 06 UTC on 1 July 2001 from *Meteosat-5* (Figure 3.11a), ERA-40 (Figure 3.11b), as well as the actual IR and visible satellite imagery for the corresponding time (Figures 3.11c and 3.11d, respectively). The *Meteosat-5* cloud amounts are gridded at 0.125° resolution. The ERA-40 Re-analysis data are also shown at 0.125° resolution, but

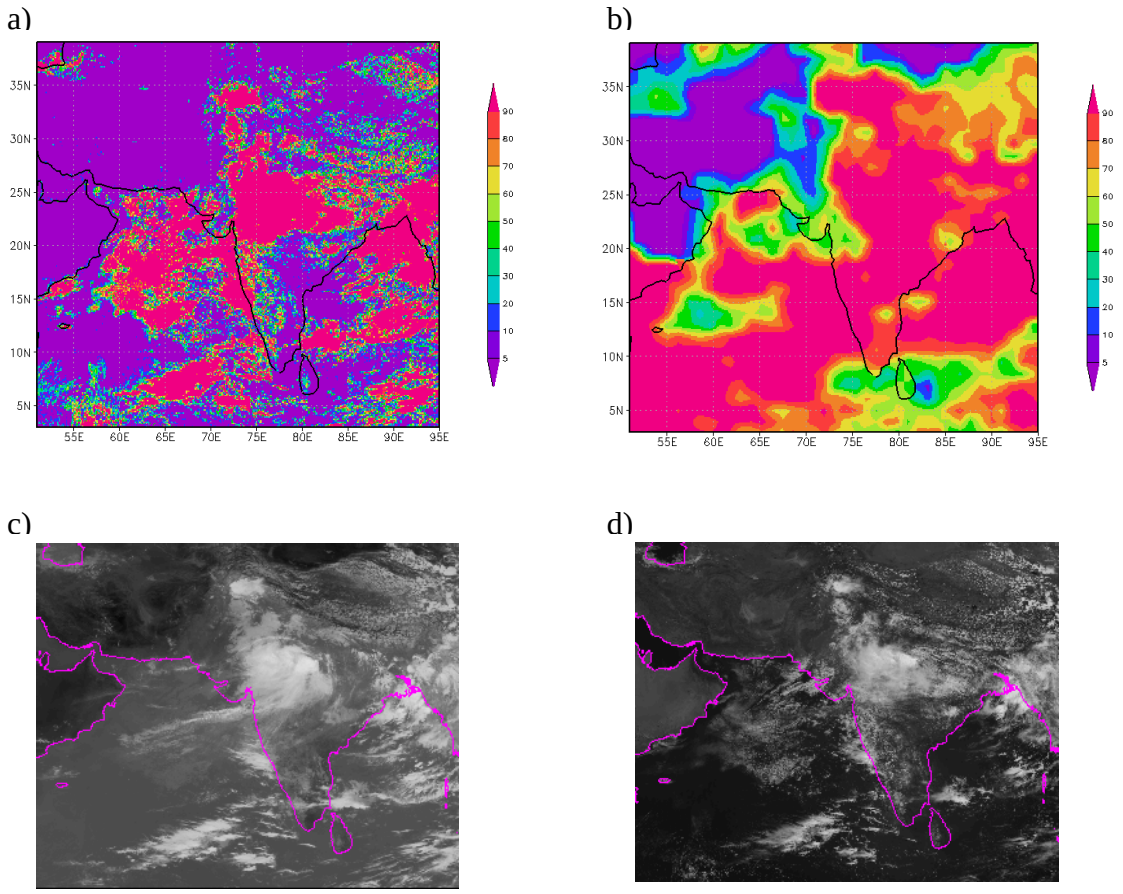

Figure 3.11. Total cloud amount (%) at 06 UTC on 1 July 2001 from a) *Meteosat-5* cloud analysis, b) ERA-40 Re-analysis; *Meteosat-5* image from c) IR channel, d) visible channel.

smoothing is apparent since it was interpolated from the ECMWF model output on an N80 reduced Gaussian grid with approximate resolution of 1.125°. The NCEP data are not shown because of the much larger disparity in resolution, (~ 2°) for the T62 Gaussian grid. The ERA-40 Re-analysis shows a pronounced over-analysis of clouds in comparison to the satellite-derived clouds, which are in close agreement with the actual satellite imagery.

A more comprehensive analysis is used to determine whether the model over-analysis of clouds seen in Figure 3.11 represents a trend. It is of interest to know how

the models perform as a function of season as well as geographical location. To address these concerns, an analysis is performed for each month of the Asian monsoon season for the year 2001 (Figure 3.12). The cloud data are further broken down by location using the six data points in Figure 3.6 to contrast the various cloud regimes. Data from 06 UTC are chosen for the comparison as the model data are available in 6-hourly increments (00, 06, 12, and 18 UTC) daily, and 06 UTC is a daylight hour for the entire *Meteosat-5* domain in this study. The ISCCP D1 data are also included for comparison. To address concerns that spatial resolution of the products may affect the analysis, the *Meteosat-5* data are up-scaled to 2.5° resolution and the 2.5° version of the ERA-40 Re-analysis is used to match the ISCCP D1 resolution. The NCEP/NCAR re-analysis resolution is comparable at ~2°. Of the four data sources, the ERA-40 Re-analysis consistently produces the highest cloud amounts at all points throughout the season. On average, the ISCCP D1 cloud amounts are the next highest, followed by the NCEP/NCAR Re-analysis. *Meteosat-5* cloud amounts are generally lower than the others. This occurs in part because the more detailed analysis at 0.125° resolution detects more breaks between clouds. When the high resolution data are averaged in the up-scaling process, the 0% cloud amounts in the breaks reduce the overall average in the 2.5° grid box.

Chevallier and Kelly (2002) found that the spatial correlation between clouds derived from ECMWF and *Meteosat-5* was lower over land than ocean. In this evaluation, agreement between all cloud sources is best over the northern parts of the Arabian Sea and Bay of Bengal, while larger variation exists in the southern parts of the water regions. The largest disparity in cloud amounts occurs for the Tibetan

Plateau, where snow and highly variable terrain increase the difficulty of analysis, forecasting, and satellite retrieval of clouds.

Agreement between the various data sets is best at the beginning and the end of the monsoon season, with more variability during the peak monsoon months. The lack of agreement in cloud forecasts during this time frame confirms the well-documented shortcomings of numerical models in predicting the Indian monsoon rainfall (Sperber and Palmer 1996, Krishnamurthy and Shukla 2000; Cherchi and Navarra 2003).

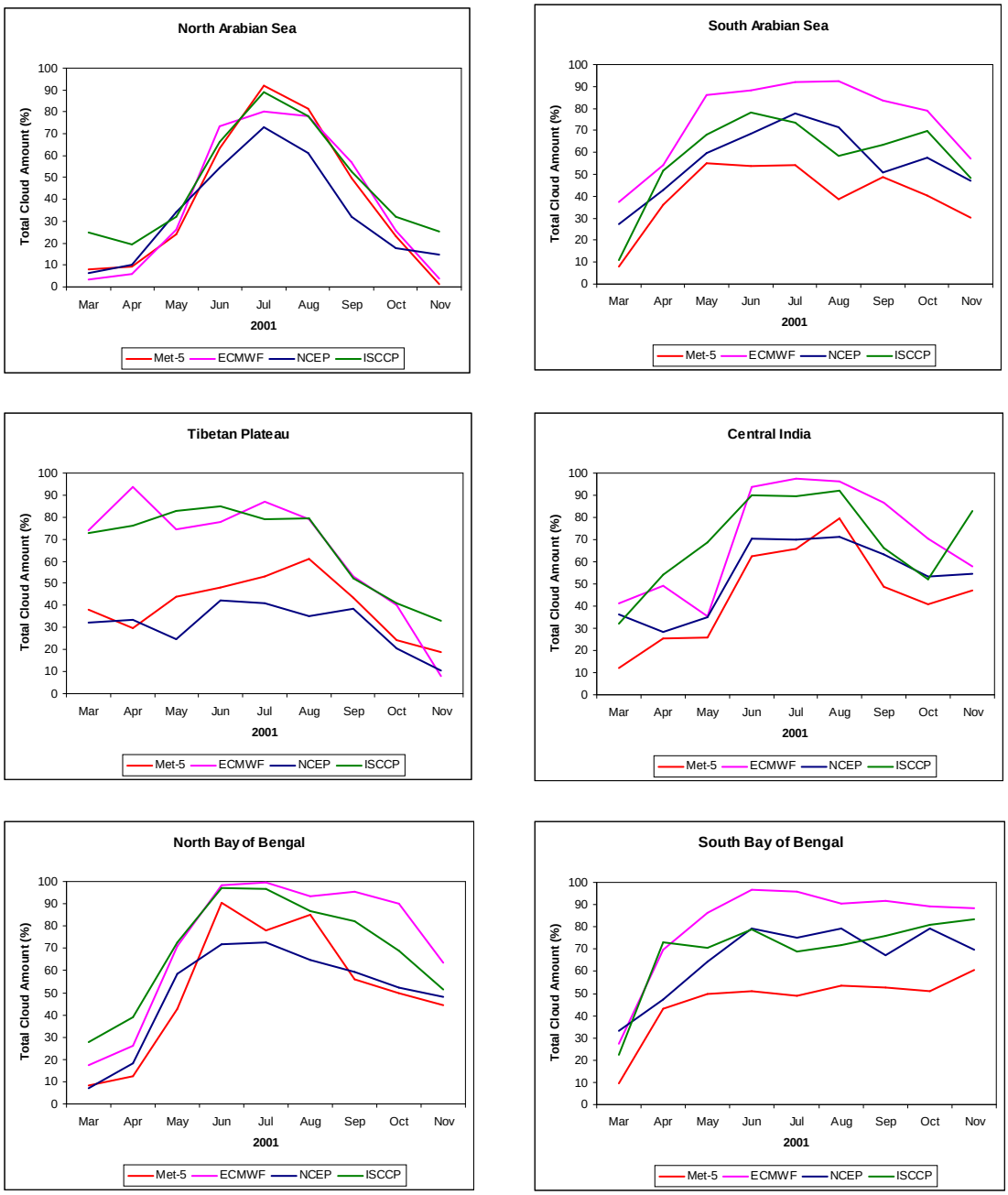

Figure 3.12. Comparison of monthly mean total cloud amount (%) at 06 UTC for each month of the 2001 monsoon season for *Meteosat-5*, ERA-40 Reanalysis, NCEP/NCAR Re-analysis, and ISCCP for each point in Figure 3.6.

Chapter 4: Revisiting the "Elevated Heat Pump" Hypothesis

4.1. Background

The role of aerosols in the monsoon system and the need to address them in numerical models is gaining attention (Lau et al. 2006; Babu et al. 2004; Chung et al. 2002). Increased availability of aerosol data from in situ observations and remote sensing platforms makes this a promising area of exploration. Aerosols pose a complex problem due to their competing effects of both reflecting and absorbing solar radiation. Certain aerosol types, such as volcanic ash, tend to cause temperature decrease at the earth's surface by reflecting incoming solar radiation—the so-called "solar dimming" effect (Stanhill and Cohen 2001; Wild et al. 2004). Conversely, dust, black carbon, and other aerosols produce an atmospheric heating effect by absorbing solar radiation. Recent studies of aerosol effects on the Indian monsoon resulted in somewhat conflicting conclusions. Results from general circulation model (GCM) simulations have shown that solar dimming from aerosols can decrease the intensity of the Indian monsoon on multi-decadal time scales by weakening the land-sea temperature gradient in the region (Ramanathan et al. 2005). Alternatively, aerosol-induced atmospheric heating has been linked to a strengthening of the monsoon in southern China, northern India, and the Bay of Bengal by impacting circulation patterns, vertical motions, and atmospheric stability (Menon et al. 2002;

Lau et al. 2006). These conflicting findings illustrate the necessity for further investigation into aerosol impacts on the monsoon.

The high-resolution cloud analyses derived from *Meteosat-5*, along with supplementary observational data provide an opportunity to examine the "Elevated Heat Pump" (EHP) hypothesis proposed by Lau et al. (2006). The basic premise of the hypothesis is that absorbing aerosols such as black carbon from northern India and dust from the deserts of western China, Afghanistan, Pakistan, and southwest Asia stack up against the foothills of the Himalayas in the pre-monsoon season and cause anomalous upper-tropospheric warming in the Tibetan Plateau region. The aerosol transport is evident in Figure 4.1, which shows the long-term mean of the general circulation near the surface in April. A relatively strong band of westerlies extends from the deserts of southwest Asia toward the Indo-Gangetic Basin (IGB) at the base of the Himalayas. A southerly wind from northeast India contributes industrial black carbon to the aerosol load in the IGB. The hypothesis proposes that warming by aerosol absorption causes the air to rise and act as an "Elevated Heat Pump", drawing in moist air from the Indian Ocean and bringing an early onset of the Indian monsoon and a northwestward shift in monsoon rainfall. The sinking motion that completes the meridional circulation also shifts northward, such that the southern part of the Indian subcontinent experiences dryer-than-normal conditions in the early part of the peak-monsoon season. Impacts on rainfall extend farther than the subcontinent itself, as the heat low established over the Tibetan Plateau is balanced by an elongated surface high pressure ridge oriented southwest to northeast from the northwestern Pacific through the northern South China Sea and southern Bay of

Bengal into the central Indian Ocean. This pushes the typical *Mei-yu* rain belt northward and suppresses precipitation in the northern Indian Ocean, eastern China, and the western Pacific, while increasing rainfall totals in central India, the northern Arabian Sea, the northern Bay of Bengal, central China, and Korea. These conclusions were reached based on a 10-year run of the NASA finite-volume GCM with and without aerosol forcing.

The role of the Tibetan Plateau as an elevated heat source has long been recognized as one of the driving mechanisms of the Asian monsoon (Flohn 1968; Yeh 1981; Murakami 1987; Ueda and Yasunari 1998). Li and Yanai (1996) observed that the reversal of the meridional temperature gradient due to intense heating of the Tibetan Plateau in springtime coincides with the onset of the monsoon. The heating of the plateau prior to monsoon onset is mainly due to sensible heat flux in the semi-arid western part of the Plateau and latent heat flux in the more humid eastern region (Flohn 1968; Yeh and Gao 1979; Luo and Yanai 1984; He et al. 1987). Taniguchi and Koike (2007) also showed that latent heat release from convective activity is responsible for heating through the depth of the troposphere in the eastern plateau, even before the rainy season begins. The EHP hypothesis suggests that warming caused by absorbing aerosols provides another mechanism to enhance the heating of the Tibetan Plateau. The potential impact of aerosol absorbing effects is magnified in this situation since the mass of the atmosphere above the plateau is roughly half of that near sea level and any heat added warms the air more effectively than over low-level terrain (Yeh 1981). This can further strengthen the thermally induced

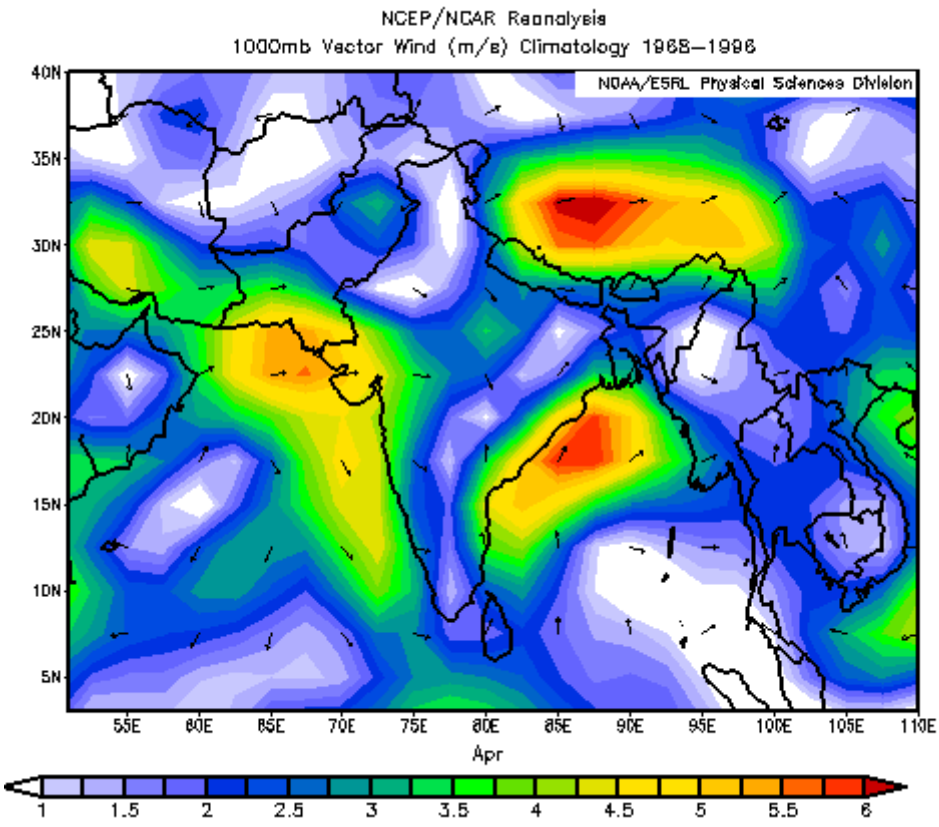

Figure 4.1. Long term mean (1968-1996) 1000 mb wind vectors for April from NCEP/NCAR Re-analysis. Colors represent wind speed in m/s.

circulation that draws in moisture from the Indian Ocean, bringing potential for increased convection.

Preliminary validation of the hypothesis was conducted by Lau and Kim (2006). Four high-aerosol years (1980, 1985, 1988, and 1991) and four low-aerosol years (1982, 1983, 1990, and 1992) were selected for the analysis based on the Total Ozone Mapping Spectrometer (TOMS) Aerosol Index (AI) (Hsu et al. 1999). The TOMS AI is a measure of how much the observed wavelength dependence of UV radiation backscattered from aerosols differs from that due to pure molecular scattering. The data record runs from 1978 through 2006, although data collected after mid-2000 are unsuitable for trend analysis due to inhomogeneous degradation of

the instrument's scanner mirror. Details of the problem can be found on the TOMS web site at: http://toms.gsfc.nasa.gov/news/news.html.

Figure 4.2 shows the TOMS AI values for May of each year used in the analysis of Lau and Kim (2006). Of the high-aerosol years, 1988 and 1991 have significant levels of aerosols in IGB with an AI of 3 or more. Of the low-aerosol years, 1982 and 1983 have AI values less than 2 in the IGB. The remaining 2 years in each category are less extreme, with an average AI value between 2.25 – 2.50. Evaluation of the hypothesis was performed using rainfall observations from the

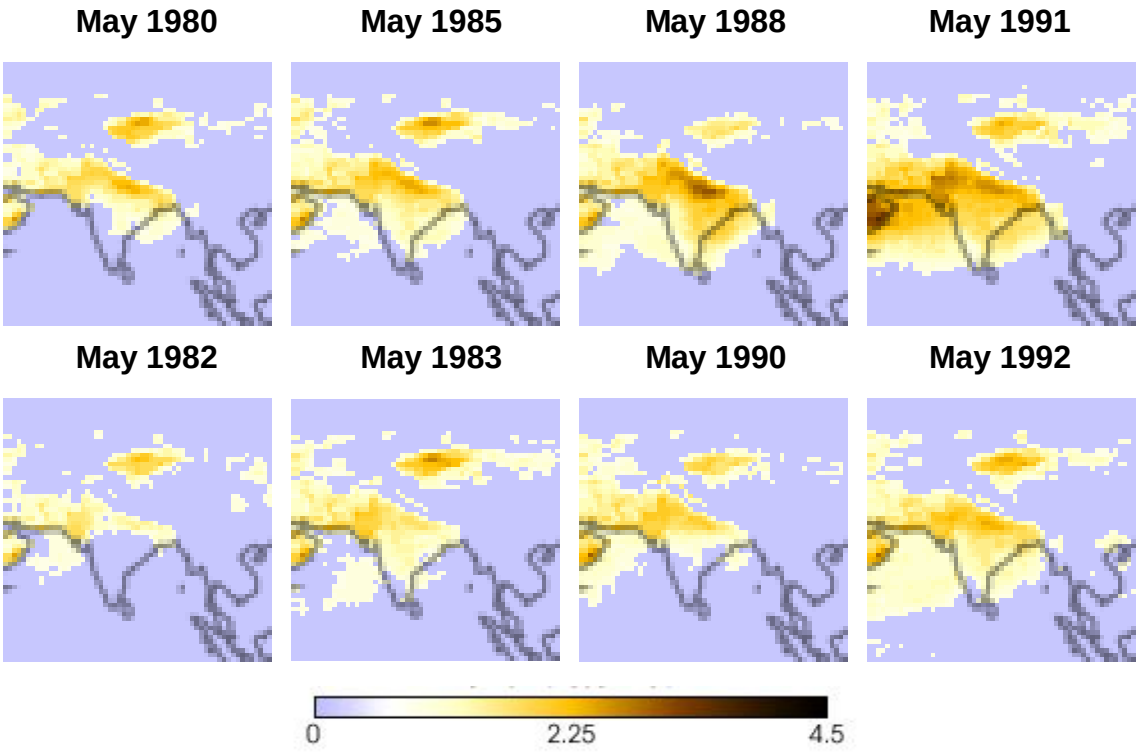

Figure 4.2. TOMS aerosol index for May of the years used in the study by Lau et al. (2006). High aerosol years are shown in top row and low aerosol years are shown in bottom row.

Global Precipitation Climatology Project (GPCP) (Huffman et al. 1997) and temperature and wind fields from the NCEP/DOE-R2 reanalysis data (Kanamitsu et al. 2002) composited separately for the high- and low-aerosol years. In agreement with the hypothesis, the following features were found in the high aerosol years: Composite rainfall data showed an increase in precipitation in northern India in the early part of the season, spreading to all of India in June and July, and decreasing in August; enhanced ascent of warm air along the Himalayan foothills in May was evident in the composite wind fields; statistically significant correlation between high aerosol levels and warm upper tropospheric temperature anomalies in northern India and the Tibetan Plateau were found. An opposite behavior was observed during the low aerosol years.

Bollasina and Nigam (2008) conducted an evaluation of the EHP hypothesis using regressions of various parameters such as precipitation, diabatic heating, winds, and radiative fluxes on the TOMS AI for May of the years 1979-1992. In contrast to the results of Lau and Kim (2006), they concluded that high aerosol loads in the IGB are associated with deficient precipitation throughout India in early spring. Additionally, their results suggest that land-surface processes set in motion by high aerosol concentrations, rather than the EHP mechanism, led to stronger monsoon rainfall during the months of June and July.

The approach used in the current work utilizes newly available information on several crucial parameters for confirming the existence of the EHP hypothesis. In contrast to the previous studies that used TOMS AI, the springtime aerosol load in the IGB is determined from aerosol optical depth retrieved from MODIS and MISR,

which provide an improved representation of the total columnar aerosol optical depth as compared to the TOMS AI. Cloud and convection data used in the analysis are obtained from hourly *Meteosat-5* satellite observations processed at 0.125° resolution. The high spatial resolution of this product allows a detailed investigation of cloud patterns in the Himalaya foothills region where much of the EHP effect is proposed to play out, and the high temporal resolution gives a good measure of the frequency of occurrence of convection. Finally, the monsoon behavior during individual years is analyzed in relation to the aerosol load in the IGB for each year. This approach is favored over analyzing the composite of several years because the predicted patterns should be evident during extreme aerosol years if the EHP mechanism is operating as hypothesized.

4.2. Experiment design

4.2.1. Data

The determination of aerosol loading was made by analyzing aerosol retrievals from MODIS and MISR. Figure 4.3 shows the time series of monthly mean aerosol optical depth (AOD) in the IGB from April 2000 – December 2005 for both sensors. AOD peaks around June under the influence of both industrial pollutants and dust and washes out rapidly with monsoon precipitation. Both data sources agree that 2004 had the highest aerosol content. MODIS shows 2001 as the lowest aerosol year of the decade, while the lowest MISR aerosol retrieval occurred in 2005. Prasad and Singh (2007) compared MODIS and MISR AOD to ground-based observations in the IGB from AERONET for the years 2000-2005. They found that MISR retrievals were in closer agreement to ground observations than MODIS for both winter and

summer seasons, attributable to the multiple viewing angles and spectral resolution of the MISR instrument. The use of monthly mean aerosol information precludes a detailed examination of the effect of rainfall scavenging on the reduction of aerosols as the monsoon evolves. However, the EHP hypothesis is built on the impact of warming due to the aerosol load in the pre-monsoon season, before washout by monsoon precipitation. Monthly mean aerosol information sufficiently characterizes the load for pre-monsoon months.

Radiance observations from *Meteosat-5* at hourly resolution are used to determine cloud amount and frequency of occurrence of convection. Total and convective cloud amounts are derived using the method described in Chapter 2. Since the cloud detection method is limited in its ability to accurately detect clouds at night when visible data are unavailable, the cloud data used in the study are based only on daytime values. The lack of nighttime cloud data does not appear to hamper the analysis for several reasons. First, clouds and convection are analyzed in a relative sense of high-aerosol year versus low-aerosol year, so absolute values of cloud amount and convection have lesser importance. Next, the percentage of convection missed overnight in the areas of interest is small because convection over land peaks in late afternoon in the Indian monsoon region (Gray and Jacobson 1977; Dai 2001; Islam et al. 2004.). Third, cloud patterns derived from *Meteosat-5* show close agreement with rainfall amounts from other sources, indicating that they adequately represent the convection.

As in the study by Lau and Kim (2006), temperature data from the NCEP/DOE-R2 reanalysis and precipitation data from GPCP are incorporated into

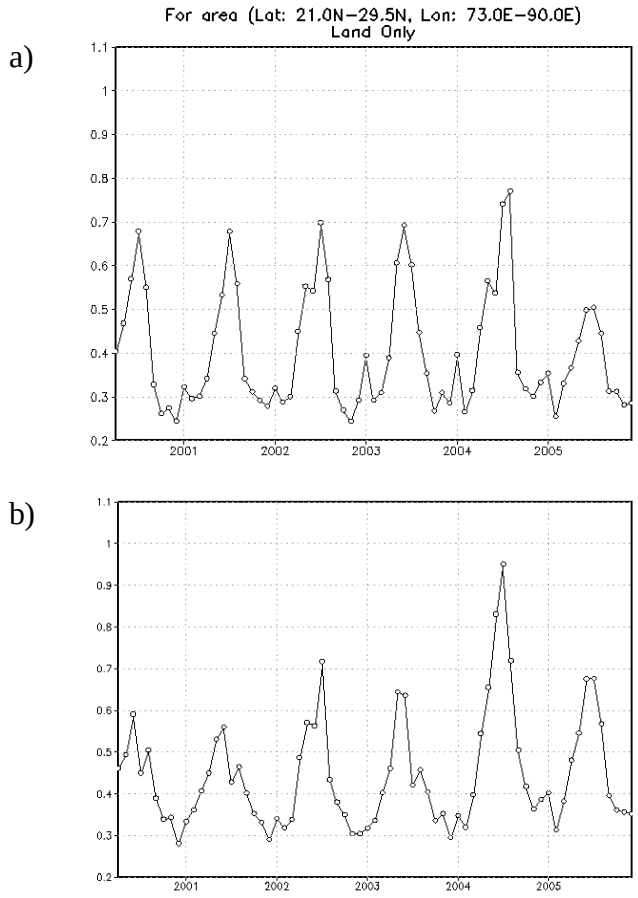

Figure 4.3. Monthly mean daytime aerosol optical depth at 0.55 μm in the Indo-Gangetic Basin as derived from a) MISR, and b) MODIS.

the hypothesis validation. Additionally, rainfall information from ground based observations from the IITM at Pune are used. The rain gauge network consists of 306 stations, and monthly mean rainfall amounts are computed for 30 subdivisions in India using an area-weighted average (Figure 4.4).

4.2.2. Methodology

The years 2000 – 2005 were used for the study based on the overlap between availability of aerosol information from modern sensors and the *Meteosat-5* satellite imagery used to derive cloud amount and convection. In light of the aerosol retrievals shown in Figure 4.3, the following classifications are made: 2004 = high-aerosol year; 2001 and 2005 = low-aerosol years; 2000, 2002, and 2003 = moderate-aerosol years. The following verifiable aspects of the proposed EHP effect are

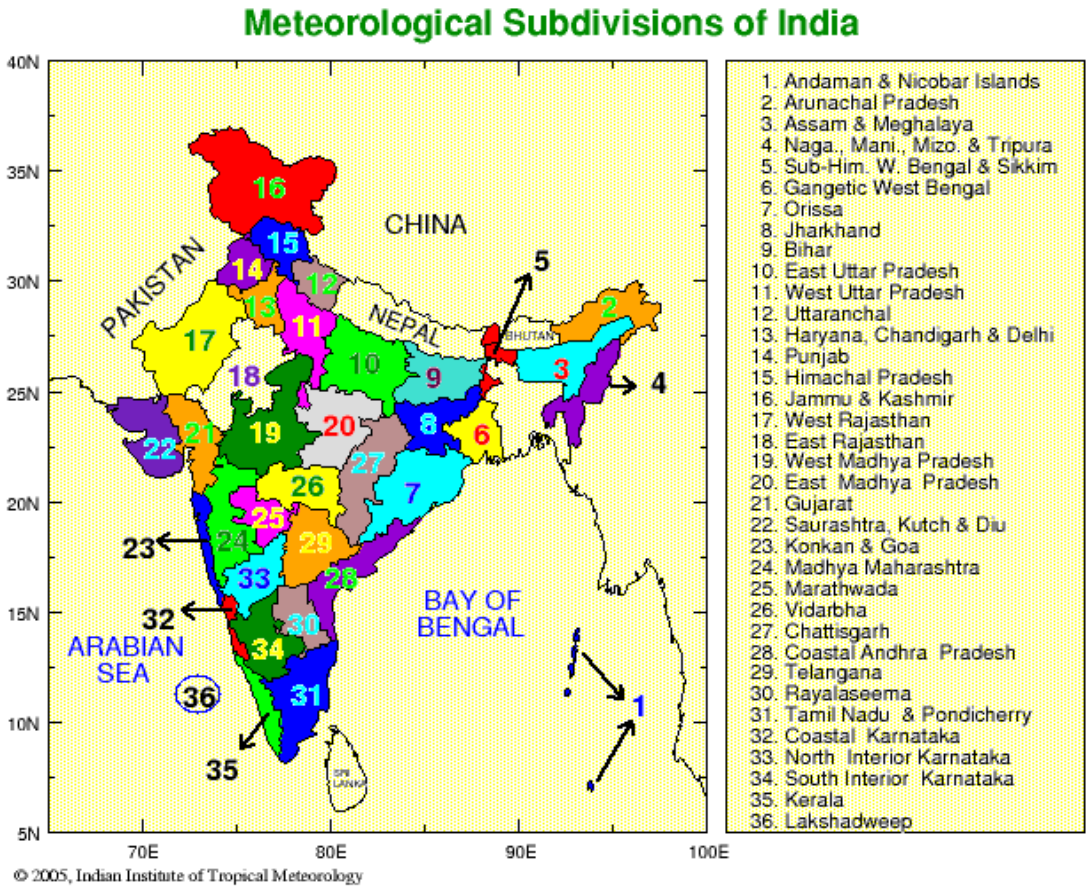

Figure 4.4. Meteorological subdivisions of India used to compile rain gauge data from the IITM at Pune.

assessed in relation the aerosol load for each year: (1) the temperature above the Tibetan Plateau region during April should be higher in the high aerosol year due to aerosol absorption of shortwave radiation, (2) convection and precipitation in the foothills of the Himalayas and in northern India should be higher in May during the high aerosol year due to the early onset of the monsoon, (3) convection and precipitation in southern India should be lower in June in the high aerosol year due to the northward shift in the subsiding branch of the meridional circulation over India, (4) convection and precipitation for the peak-monsoon season in the high aerosol year should be higher in northern India and the Bay of Bengal, and lower in eastern Asia, the northern Indian Ocean, and the western Pacific.

4.3. Experiment results

4.3.1. Temperature

According to the EHP hypothesis, in the high-aerosol year the Tibetan Plateau should undergo anomalous upper tropospheric warming in April due to absorption of shortwave radiation by aerosols. Figure 4.5 shows the April 400 mb temperature anomaly from the NCEP/DOE-R2 Reanalysis for the high aerosol year. The anomaly is based on climatology from 1968-1996. Although anomalous warming is observed over the Tibetan Plateau in the high-aerosol year, the center of the anomaly is located north of 45° N and cannot be attributed to heating from aerosol absorption.

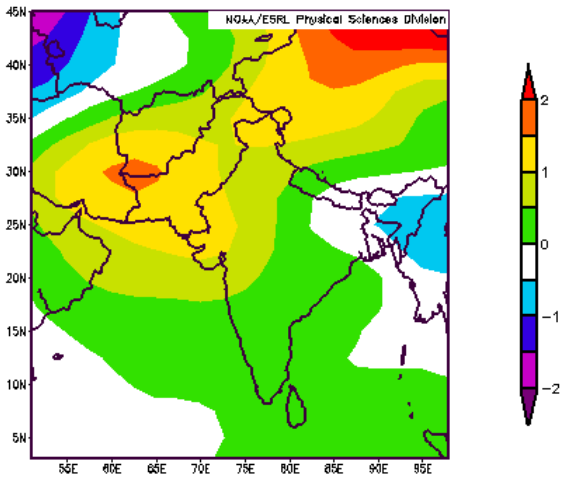

Figure 4.5. 400 mb temperature anomaly (°C) from NCEP/DOE-R2 Reanalysis for April 2004.

4.3.2. Clouds and convection in pre-monsoon season

According to the hypothesis, the anomalous warming observed over the Tibetan Plateau should accelerate the monsoon cycle and shift precipitation northward, resulting in enhanced convection in the foothills of the Himalayas in May during a high-aerosol year. The difference between frequency of occurrence of convection in the foothills for May 2004 and May of the other years of the study is shown in Figure 4.6. Frequency of occurrence of convection is computed for each point in the domain as the number of daytime hours in the month in which cloud top temperature and optical depth meet the convective cloud criteria described in Chapter 2. In Figure 4.6e there is evidence of an increase in convection in the high-aerosol year in comparison to 2005, the lowest aerosol year. This gives some weight to the prediction that the high aerosol load accelerates the monsoon onset. However, there is little increase in convection in comparison to the other low aerosol year (2001,

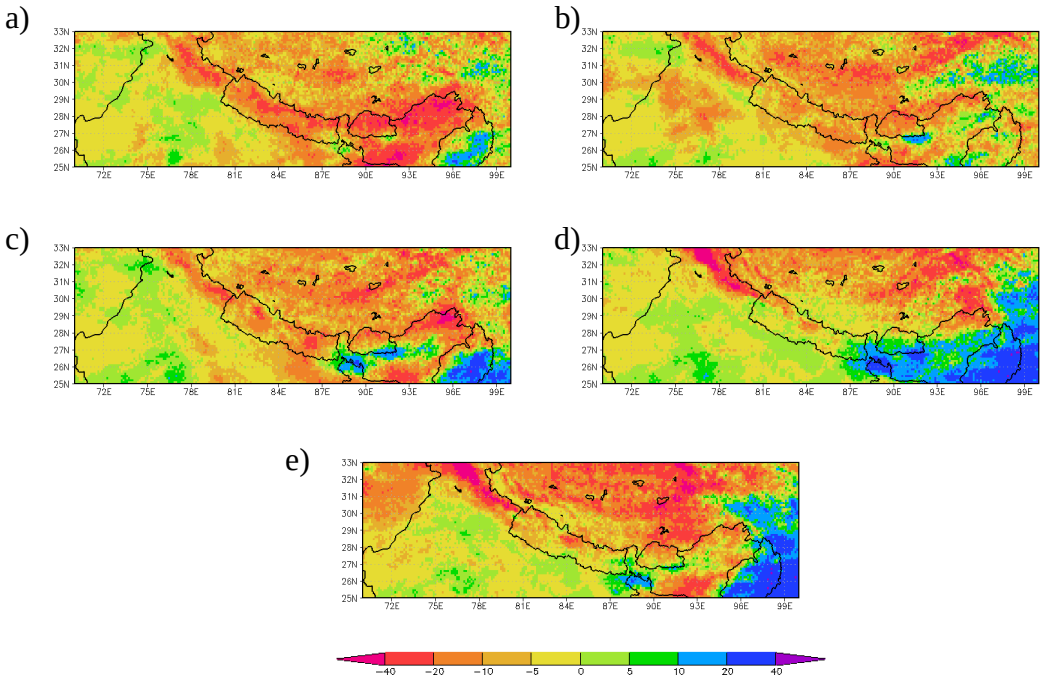

Figure 4.6. Difference in frequency of occurrence of convection for May of a) 2004-2000, b) 2004-2001, c) 2004-2002, d) 2004-2003, e) 2004-2005.

Figure 4.6b). In fact, the largest increase in convection occurs relative to 2003, which should be unrelated to the EHP hypothesis since it is a moderate-aerosol year.

The frequency of occurrence of convection in the Himalaya foothills region derived from *Meteosat-5* agrees well with rain gauge data collected by the IITM. Table 4.1 shows the May rainfall totals for the years 2000 – 2005 for 4 subdivisions located in the Himalaya foothills region as shown in Figure 4.4. The data confirm that 2004 precipitation was higher than 2003 and 2005 in all subdivisions and lower than 2001 in all but the easternmost subdivision.

In addition to the proposed increase in convection in the foothills region, the simulations of Lau et al. (2006) predict a northward shift in precipitation during May

Table 4.1. May rainfall totals derived from IITM rain gauge data for subdivisions shown in Figure 4.4.

	Sub 3	Sub 5	Sub 9	Sub 10	Sub 11	Sub 13	Sub 14
2000	3152	2995	1551	505	382	365	440
2001	2331	2933	1406	404	352	773	507
2002	2191	1241	926	340	407	748	332
2003	2137	1865	549	34	65	141	61
2004	3646	2285	830	231	347	537	484
2005	2872	1982	254	129	104	107	13

of the high aerosol year, with enhanced activity located north of 20° N. Figure 4.7 shows the difference in frequency of occurrence of convection for all of India between May of 2004 and the average of the months of May for the mid- and low-aerosol years. In contrast to what is expected, a significant increase in clouds and convection occurred during the high-aerosol year in southern India and the southern parts of the Arabian Sea and Bay of Bengal. The majority of the region north of 20° N experienced a decrease in convection during 2004. The similarity in patterns for

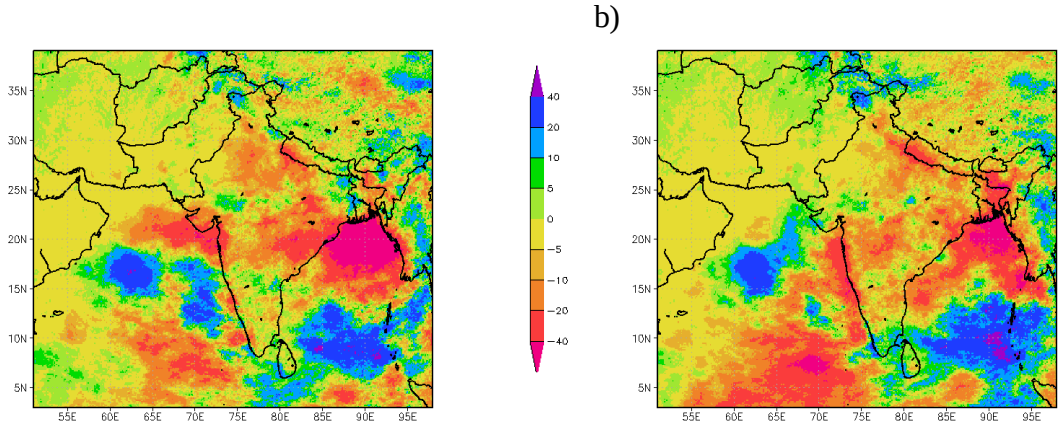

Figure 4.7. Difference in frequency of occurrence of convection derived from *Meteosat-5* for a) May 2004 – average of May for the low-aerosol years, and b) May 2004 – average of May for the mid-aerosol years.

a) b)

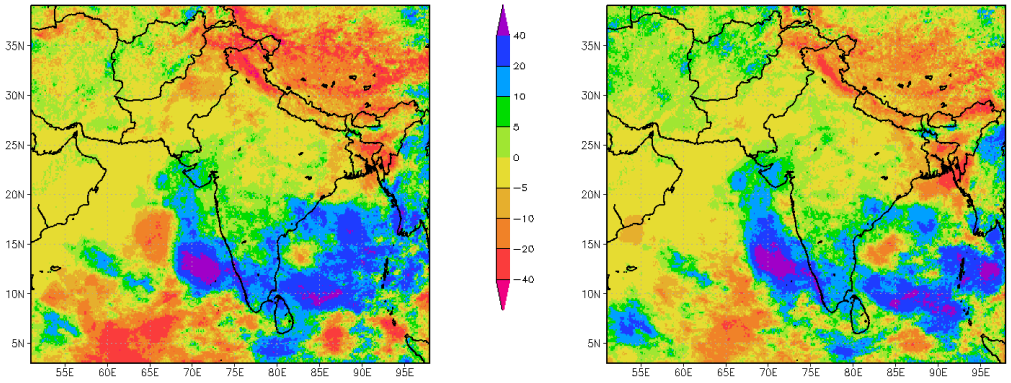

Figure 4.8. Difference in frequency of occurrence of convection derived from *Meteosat-5* for a) June 2004 – average of June for the low-aerosol years, and b) June 2004 – average of June for the mid-aerosol years.

the mid- and low-aerosol years seems to indicate that the aerosol loading in the IGB is not a major influence on the convective activity.

4.3.3. Clouds and convection in peak-monsoon season

Throughout the peak monsoon season (June – September) there are some discrepancies between the behavior predicted by the EHP hypothesis and the actual turn of events. By June, the subsiding branch of the meridional circulation that balances the forced ascent in the foothills should be well-established, causing a decrease in convection in southern India in the high-aerosol year. This aspect of the hypothesis is evident in Figure 4.8, which shows the difference in frequency of occurrence of convection between June of 2004 and the average of the months of June for the mid- and low-aerosol years. The convection patterns in southern India are reversed from May, with less convection occurring in the high-aerosol year. Note however that this pattern holds throughout the entire sub-continent, whereas the

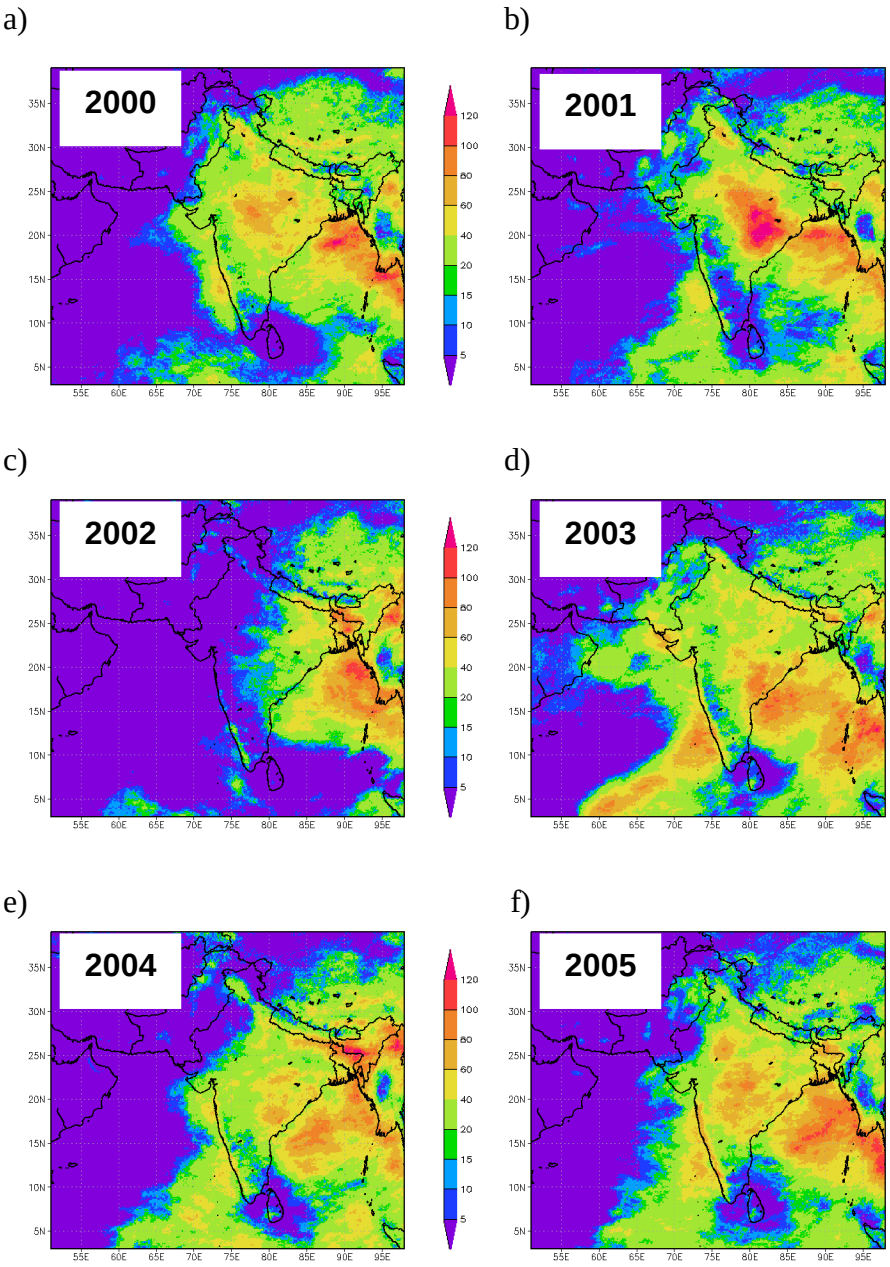

Figure 4.9. Frequency of occurrence of convection derived from *Meteosat-5* for July of 2000 – 2005.

hypothesis prescribes that precipitation in the north in 2004 should still exceed that in the low-aerosol years because of the early progression of the monsoon.

Frequency of occurrence of convection for each July of 2000 – 2005 is displayed in Figure 4.9. The year 2004 is second only to 2002 (an extremely notable drought year) as the year with the least amount of convection in the Indian subcontinent. The year 2001 had the highest occurrence of convection, and 2005 had a healthy amount as well. This contradicts the hypothesis, which predicts more precipitation in the high aerosol year.

As shown in Figure 4.10, it is not until August that convection in northwest India and the northern Bay of Bengal in the high-aerosol year exceeds that in the low-aerosol years. This is again contradictory to the hypothesis, which asserts an early start to the monsoon and an early drawdown to the season.

Figure 4.11 shows the difference in overall rainfall patterns for the combined months

a) b)

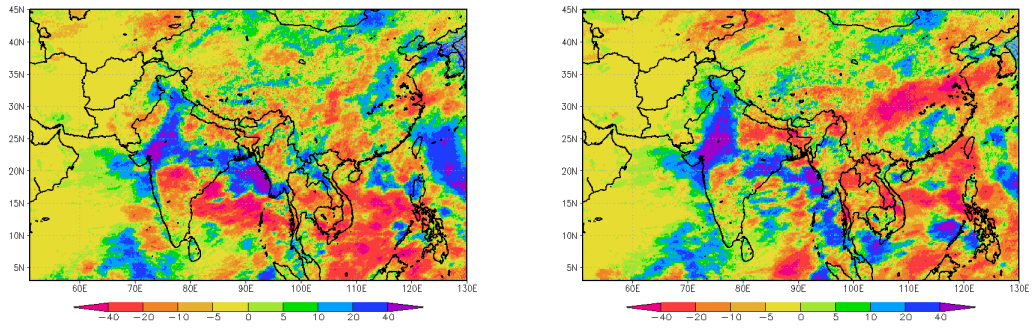

Figure 4.10. Difference in frequency of occurrence of convection derived from *Meteosat-5* for a) August 2004 – August 2001 and b) August 2004 – August 2005.

a) b)

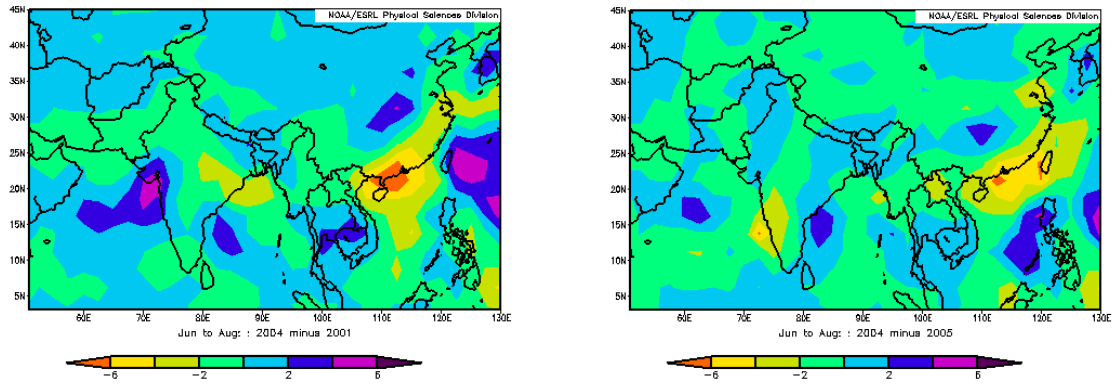

Figure 4.11. Difference in GPCP rainfall (mm/day) for a) JJA 2004 – JJA 2001, b) JJA 2004 – JJA 2005.

of June, July, and August for the high aerosol year minus the low aerosol years. Precipitation is derived from the GPCP database. There is less precipitation throughout most of India, the northern Bay of Bengal, and eastern China during the high-aerosol year. Positive rainfall differences occurred in the southern parts of the Arabian Sea and Bay of Bengal, central China, and Korea. These patterns are in stark contrast to what was predicted by the EHP hypothesis in the region of India and its surrounding waters, although they do agree over China and Korea.

4.4. Interpretation of results

While it would have been interesting to perform the current analysis for the years used by Lau and Kim (2006), the sources of high resolution cloud and aerosol information chosen for this study were not available until 1998 and 2000, respectively. Therefore, the years 2000 – 2005 were used for the study based on the overlap between availability of aerosol information from modern sensors and the *Meteosat-5* satellite imagery used to derive clouds and convection. If the EHP hypothesis truly characterizes the impact of aerosols on monsoon behavior, its effects

should be evident when comparing 2004, which had the highest aerosol load of the decade, with low aerosol years such as 2001 and 2005. While some of the behavior predicted by the EHP hypothesis was observed to occur in this study, many events unfolded contrary to what was anticipated. Several possible reasons for why the observations did not agree with the predictions are explored here.

4.4.1. Global influences on monsoon rainfall

Global teleconnections have been found between Indian Summer Monsoon Rainfall (ISMR) and various atmospheric and oceanic patterns outside the Indian monsoon region. Of the numerous indicators, some of the most prominent are El Nino/Southern Oscillation (ENSO), the North Atlantic Oscillation (NAO), and Eurasian snow cover. Analysis of the record of ISMR for the last century shows a strong correlation between drought years and the warm phase of ENSO (Kumar et al. 2006; Chakraborty and Krishnamurti 2003; Krishnamurthy and Goswami 2000, Rasmussen and Carpenter 1983). A high winter value of the NAO Index, which measures the strength of mid-latitude westerlies in the North Atlantic, has been linked to deficient monsoon rainfall the following summer (Kakade and Dugam 2006; Dugam et al. 1997). Additionally, an inverse relationship has been observed between the amount of Eurasian snow cover and ISMR ((Hahn and Shukla 1976; Parthasarathy and Yang 1995; Bamzai and Shukla 1999). These factors would not have been captured by the model simulation used to develop the EHP hypothesis, so it is possible that their influence could mask or take precedence over the EHP effect. Thus, it is necessary to examine the larger picture and investigate whether or not any

a)

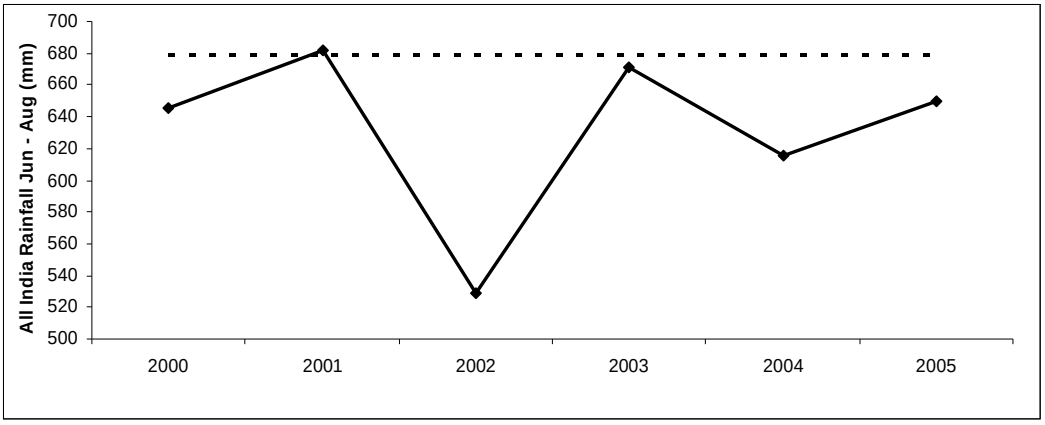

b)

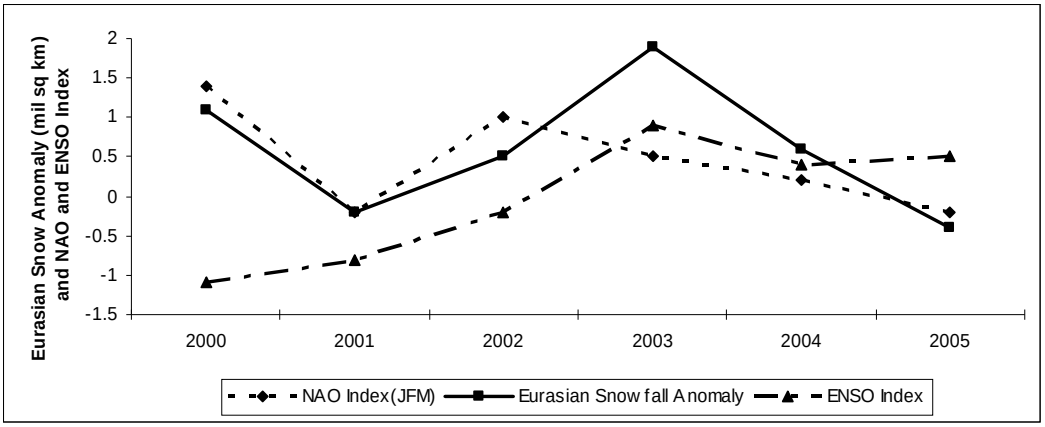

Figure 4.12. a) All India Rainfall from Jun – Aug for the years 2000 – 2005 (dashed line gives average seasonal rainfall for the period 1871 – 2002), b) Eurasian snowfall anomaly, NAO Index, and ENSO Index for the same years.

of these teleconnections had a strong impact on monsoon behavior for the period of interest.

To address this possibility, the inter-annual variability of the aforementioned factors has been compared to the variation in monsoon conditions seen for the years 2000 – 2005. Figure 4.12a shows the All India rainfall for June – August as derived from the IITM rain gauge data. The dashed line represents the average seasonal

rainfall from the period 1871 – 2002. Figure 4.12b shows the Eurasian snow cover anomaly and the NAO and ENSO indices for 2000 – 2005. The inverse relationship between Eurasian snow cover and ISMR was observed for the years 2000, 2002, and 2004. Snow cover was nearly neutral in 2001 and quite high in 2003, yet ISMR in both years was very close to average. The year 2005 did not fit the pattern at all, as both snow cover and ISMR were lower than average. The correlations between the NAO Index and ISMR nearly mirrored those of the Eurasian snow cover anomaly. The main differences were that the NAO Index was only weakly positive in 2004 when rainfall was extremely low and it was not as high as the snow cover anomaly in 2003. Recent studies have shown that the relationship between the ENSO Index and ISMR has broken down in the last two decades (Kumar et al. 1999; Chang et al. 2001). In the period of interest, the ENSO Index showed a cold phase for the years 2000 – 2002 and a warm phase for 2003 – 2005. Therefore, 2004 and 2005 were the only years that fit the classic pattern of below-average rainfall during the warm phase of ENSO. Based on these data, it appears that none of the teleconnections had a major influence on the monsoon evolution for the years of this study.

4.4.2. Model inaccuracies

Disparities in predicted monsoon behavior have been seen between fixed sea surface temperature (SST) models and coupled ocean-atmosphere models. The model used by Lau et al. (2005) to develop the EHP hypothesis used fixed SSTs and predicted enhanced Asian monsoon rainfall. Similarly, the study conducted by Menon et al. (2002) with a fixed SST model also found increased monsoon precipitation in parts of India and China and decreased precipitation in the northern

Indian Ocean. Alternatively, simulations with coupled models by Ramanathan et al. (2005) and Meehl et al. (2007) resulted in less Asian monsoon precipitation. When the SSTs were allowed to respond to the decreased solar radiation in northern India and surrounding waters due to aerosol absorption, the meridional SST gradient weakened. Since this gradient is one of the major driving mechanisms of the monsoon, precipitation decreased in turn.

Although climate models are valuable tools for assessing the impact of changes in individual variables, the results can be skewed by model deficiencies and biases, as well as inaccuracies in initial conditions. Observation-based studies such as the current work are complementary to model simulations and can point to parts of the model that may need improvement. In this case, the observations support the model's prediction of upper tropospheric warming above the Tibetan Plateau but not the early onset, intensification, and early drawdown of the monsoon.

4.4.3. Cloud microphysics

Lau et al. (2006) acknowledge that the simulations leading to the EHP hypothesis address only direct aerosol effects (absorption and reflection of solar radiation), and that aerosol indirect effects could complicate matters. The indirect effects of aerosols can take several forms. In the first indirect effect (Twomey effect), aerosols act as cloud condensation nuclei to produce more numerous cloud droplets with smaller sizes. This implies higher cloud reflectance and cloud optical depths. The second indirect effect (also called the cloud lifetime effect) directly follows: small cloud droplets are less efficient at generating precipitation, resulting in longer cloud lifetimes in polluted clouds than in cleaner clouds. Additionally, absorption of

solar radiation by aerosols heats the atmosphere and may cause evaporation of clouds—the so-called semi-direct effect.

Evidence of this behavior of aerosols has been identified in the Asian monsoon region by numerous investigators. Heymsfield and McFarquhar (2001) analyzed aircraft data from flights made through polluted and clean clouds in the Indian Ocean during INDOEX (Ramanathan et al. 2001) and found a three-fold increase in droplet concentrations and a 35% decrease in droplet effective size in polluted clouds. Their simulations with a 1D parcel model further implied a doubling of cloud optical depth with the high aerosol concentrations. Chylek et al. (2006) investigated the Twomey effect over the Indian subcontinent and surrounding waters using data from MODIS (Kaufman et al. 1997; Tanre et al. 1997). The cloud droplet effective radii retrieved from MODIS in clean months (the average of September months of the years 2000 – 2004) were up to 33% smaller than those retrieved in polluted months (Januarys of 2000 – 2004). Largest differences occurred in the land regions north of the Bay of Bengal, corresponding to regions of peak aerosol optical depth. Ackerman et al. (2000) found that the semi-direct effect from the haze layer observed during INDOEX 1998 and 1999 was responsible for a 25% and 40% decrease in fractional cloud cover, respectively.

Bollasina and Nigam (2008) observed that the semi-direct aerosol effect appeared to have a strong influence on pre-monsoon precipitation in the IGB. Their regression of rainfall on the TOMS AI for the years 1979-1992 showed a link between high aerosol load and deficient springtime precipitation, which they attributed to dissipation of clouds through the aerosol semi-direct effect. To

Table 4.2. Spatial correlation between MODIS AOD and frequency of convection derived from *Meteosat-5* for May of 2000-2005 for the region bounded by 25° N - 33° N and 70° E - 100° E (Himalaya foothills).

2000	2001	2002	2003	2004	2005
-0.58	-0.56	-0.67	-0.57	-0.57	-0.44

determine if such a link exists in the data used in the current study, the spatial correlation between MODIS AOD and *Meteosat-5* derived frequency of occurrence of convection in the Himalaya foothills region in May was calculated for each year of the study period. Results are shown in Table 4.2. The negative correlation is apparent for all years, albeit more strongly for some years.

In explanation of the contrast between their findings and the enhancement of precipitation in the IGB in May observed by Lau and Kim (2006), Bollasina and Nigam (2008) noted the different mechanisms at work in the eastern and western parts of the IGB. In the western region where the aerosol load is highest, precipitation appeared to be subdued by the aerosol semi-direct effect. Some increase in precipitation was seen in the eastern region, where the large-scale circulation flows northward over the Bay of Bengal, picking up abundant moisture and rising orographically when it encounters the Himalayas. Their results suggest that the high aerosol load in the west may affect the large-scale circulation in a manner that enhances this precipitation-producing mechanism in the east. However, the aerosol load in the east is rather small and does not directly cause rising motion through the EHP mechanism. Furthermore, they assert that since Lau and Kim (2006) used a

longitudinal average of precipitation across the IGB, the rainfall reduction in the west was masked by the activity in the east.

The details brought forth by the high-resolution *Meteosat-5* data support the conclusions of Bollasina and Nigam (2008). Referring back to Figure 4.6, it is clear that the most significant increase in convection during the high-aerosol year occurs in the eastern regions. The western part of the IGB predominantly shows decreases in convection, or slight increases interspersed with decreases. Based on these results along with the negative correlation found between AOD and frequency of occurrence of convection, it appears that the aerosol semi-direct effect plays an important role in observed behavior of the monsoon for this period of study.

4.4.4. Anomalies in 2004

In 2004, not only did the enhanced precipitation predicted for India under the EHP hypothesis not materialize, but it was, in fact, a notable drought year. Indian Summer Monsoon Rainfall (ISMR) lagged 13% below normal rainfall totals. Jenamani et al. (2007) produced an in depth study of the factors that characterized the failure of the 2004 monsoon, and found multiple culprits. First, there was a decided shortfall of depressions in the region. The three depressions that formed represent less than half of the number expected on the average. Since the 1960s, the number of depressions formed during the monsoon season has been on a steady decline (Singh 2001), but in years with few depressions there is often compensation from a higher number of persistent lows (Jenamani 2004). This was not the case in 2004, when the number of lows was near-normal. It was further noted that many of the semi-permanent systems that are highly correlated with the strength of the monsoon were

in unfavorable positions in 2004, particularly during the month of July, which had the largest rainfall deficit. The strength of the Mascarene High, which is key to the pressure gradient that drives the monsoon, was 1 – 2 hPa below normal. The monsoon trough lay at the foothills of the Himalayas during much of July—too far north to produce typical monsoon rainfall on the Indian subcontinent. The Tibetan Anticyclone which forms in the upper troposphere due to the heating effect of the Tibetan Plateau was displaced 5° southward of its usual position. This type of shift is known to cause break periods in the monsoon. Finally, southwesterly onshore flow from the low level jet in the Arabian Sea was weaker than normal, limiting the amount of moisture transported onto the subcontinent. With all of these factors working against the development of a productive monsoon, it is possible that the EHP effect was overwhelmed in this particular year.

4.5. Summary and Conclusions

The high spatial and temporal resolution of *Meteosat-5* satellite data along with improved aerosol information from sources such as MODIS and MISR provide a unique opportunity to investigate processes that affect the Asian monsoon. This work exploits these capabilities to apply a different approach for evaluating the EHP hypothesis. It was found that in some aspects, observations were in agreement with the hypothesis but not in all aspects of it.

- Anomalous warming over the Tibetan Plateau *was observed* but appears too far north to be associated with the absorbing aerosols in the IGB

- Enhanced convection in the foothills of the Himalayas and northward shift in precipitation in May *was not observed*
- Suppression of precipitation in southern India in June *was observed*
- Early drawdown of monsoon *was not observed*
- Overall cloud and precipitation patterns for JJA
    - *Did not match* hypothesis for India and surrounding oceans
    - *Did match* hypothesis for central China and Korea

There are several factors that may have been responsible for discrepancies between the *Meteosat-5* derived cloud and convection patterns and those predicted by the EHP hypothesis:

- The impact of ocean/atmosphere coupling was not accounted for in the model simulation used to develop the EHP hypothesis.
- The model simulation did not account for aerosol semi-direct effects, which seem to be responsible for reduced precipitation in the western portion of the IGB under high aerosol load.
- Many anomalous dynamical factors combined to make 2004 a notable drought year. These factors may have masked evidence of the EHP effect.

Chapter 5: Impact of Aerosols on Shortwave Flux Retrieval

5.1. Background

The goal of the AMMA program is to improve understanding of the West African monsoon (WAM) and the factors that determine its variability on daily to inter-annual timescales. The AMMA multi-scale approach considers local, meso-, regional, and global scale processes associated with the monsoon, and their interactions. The radiative fluxes produced in this thesis are particularly suited for addressing the regional-scale processes of the WAM, where land-surface feedbacks are important. African rainfall is closely tied to land surface conditions such as soil moisture and vegetation cover (Chou et al. 2001; Grodsky and Carton 2001; Taylor and Lebel 1998). Moreover, rainfall anomalies can change soil moisture and vegetation characteristics, which in turn impact radiation and water budgets. The changes in African vegetation cover in recent decades due to drought and deforestation also affect the surface albedo, which is a strong moderator of the energy budget (Fuller and Ottke 2002). These feedbacks need to be understood in order to improve the prediction of the WAM.

The above aspects of the WAM are addressed through the AMMA land-surface modeling (LSM) component. Multiple LSMs are run to address different surface features, such as hydrological models, crop models, and soil-vegetation-atmosphere transfer schemes. A surface forcing database has been developed to ensure forcing consistency between the various models. Forcing parameters include radiation, precipitation, surface characteristics, and near-surface atmospheric parameters.

The Land Surface Analysis Satellite Applications Facility (Land SAF) produces the downwelling surface shortwave flux (DSSF) data for LSM forcing. It is based on shortwave and near-IR radiance measurements from the Spinning Enhanced Visible and Infrared Imager (SEVIRI) instrument aboard the *Meteosat-8* satellite. Separate algorithms are used for flux retrievals under cloudy- and clear-sky conditions, as determined by a cloud mask (Derrien and Le Gleau 2005) produced at the Nowcasting and Very Short Range Forecasting Satellite Applications Facility (NWC SAF). For clear-sky cases, the aerosol optical depth is determined from a climatology of aerosol types.

Initial evaluation of the Land SAF DSSF product at six European ground observing sites (Figure 5.1) shows that both the clear- and cloudy-sky flux retrieval algorithms meet user accuracy requirements, as reported in the Land SAF Validation Report for DSSF (SAF/LAND/MF/VR_DSSF/I_08 2008). For the period October 2004 – October 2006, instantaneous biases under clear- and cloudy-sky conditions combined ranged from 0 to +7 Wm^{-2}. Biases ranged from +2 to +15 Wm^{-2} for clear-sky cases and -7 to +4 Wm^{-2} for cloudy sky cases. Although the clear-sky biases are larger, they are lower as a percentage of average radiative flux values (being higher under clear conditions). The standard deviation (SD) of the differences between in situ and satellite-retrieved fluxes were 33 – 70 Wm^{-2} for clear skies and 99 – 117 Wm^{-2} for cloudy cases.

The validation report notes that on further evaluation of the Land SAF DSSF product conducted for 7 months of 2006 at the African sites of Agoufou and Banizoumbou (Figure 5.1), performance of the algorithms at these sites was

Figure 5.1 Location of ground evaluation sites for Land SAF algorithm.

significantly degraded in comparison to the European sites. Most notably, the clear-sky cases had significant positive biases on the order of 60 Wm^{-2}. It was determined that the aerosol treatment in the Land SAF algorithm is not appropriate for regions with high aerosol loads. This implies that using the Land SAF DSSF product for surface forcing in the AMMA LSMs can cause overestimation of DSSF in the WAM

region, where aerosols have a strong impact on the energy balance. Land SAF's proposed solution to this problem is to replace the aerosol climatology with an observed aerosol product, but as yet this has not been done.

The *Meteosat-7* radiative flux inference scheme provides a useful test bed for studying the sensitivity of flux retrievals to the source and treatment of aerosol inputs. The emphasis of this chapter is to investigate the impact of aerosol treatment on the accuracy of the derived fluxes. The use of both synthesized and observed aerosol properties are compared to determine the best approach for representing aerosol effects.

5.2. Aerosol experiments: model version descriptions

The availability of better aerosol information from newer observing platforms such as the EOS satellites makes it possible to include more sophisticated aerosol treatments in the radiative flux inference scheme. Two different research versions of the UMD_SRB model replace the operational version's simplistic approach of using static AOD values and very limited information on other aerosol properties with a more detailed treatment of aerosols. The following describes the approaches used in the research versions:

1) UMD_SRB-R: In this version aerosol treatment has been improved to incorporate spatial and temporal variability in AOD and to account for additional aerosol effects. The aerosol properties accounted for now include a variable single scattering albedo (SSA), asymmetry parameter, and normalized extinction coefficient. Tables are generated for five spectral intervals of 0.2–0.4, 0.4–0.5, 0.5–0.6, 0.6–0.7, and 0.7–4.0 μm. The aerosol inputs come from an aerosol "climatology" developed

by synthesizing satellite observations, model simulations, and ground measurements (Liu et al. 2005; Liu et al. 2008; Liu and Pinker 2008). The aerosol sources in the climatology include MODIS AOD retrievals (Kaufman et al. 1997, Tanre et al. 1997), simulations from the Global Ozone Chemistry Aerosol and Radiation Transport (GOCART) model (Chin et al. 2002), and ground measurements from AERONET (Holben et al. 1998, 2001). Data from all three sources are merged by using leading empirical orthogonal functions (EOFs) to identify spatial and temporal variations in the satellite and model data, and then fitting the EOFs to the AERONET observations. SSA is obtained by using the spectral variation inferred from AERONET almucantar retrievals to extrapolate the GOCART SSA value at 550 nm to the entire solar spectrum. The MODIS Angstrom exponent is used to obtain the asymmetry parameter based on an empirical relationship derived from AERONET data, and also to calculate the normalized extinction coefficient. The final data set consists of monthly mean values of aerosol properties on a global 2° x 2.5° latitude/longitude grid that accounts for variation in space, time, and spectral interval.

2) UMD_SRB-F: This version uses monthly mean *observed* values of AOD retrieved from MODIS at 1° x 1° resolution. Since MODIS does not provide information on aerosol absorbing characteristics, default values of SSA = 0.893 and asymmetry parameter = 0.95 are used. At locations where the MODIS AOD observation is missing (this occurs frequently over bright desert surfaces), the AOD values from the aerosol climatology are used in conjunction with the default values of SSA and asymmetry parameter.

The ideal aerosol input for the radiative flux inference scheme would contain *observed* values of both AOD and all of the radiatively important aerosol parameters. However, the improved aerosol information is available only from recent years and, as yet, does not include all of the aerosol properties. Due to limitations in the current information, each of the inference schemes described compromises one aspect of this ideal aerosol input. The UMD_SRB-R model has the advantage of using a more realistic representation of aerosol absorbing properties and asymmetry parameters. However, the absorbing properties could only be obtained by synthesizing

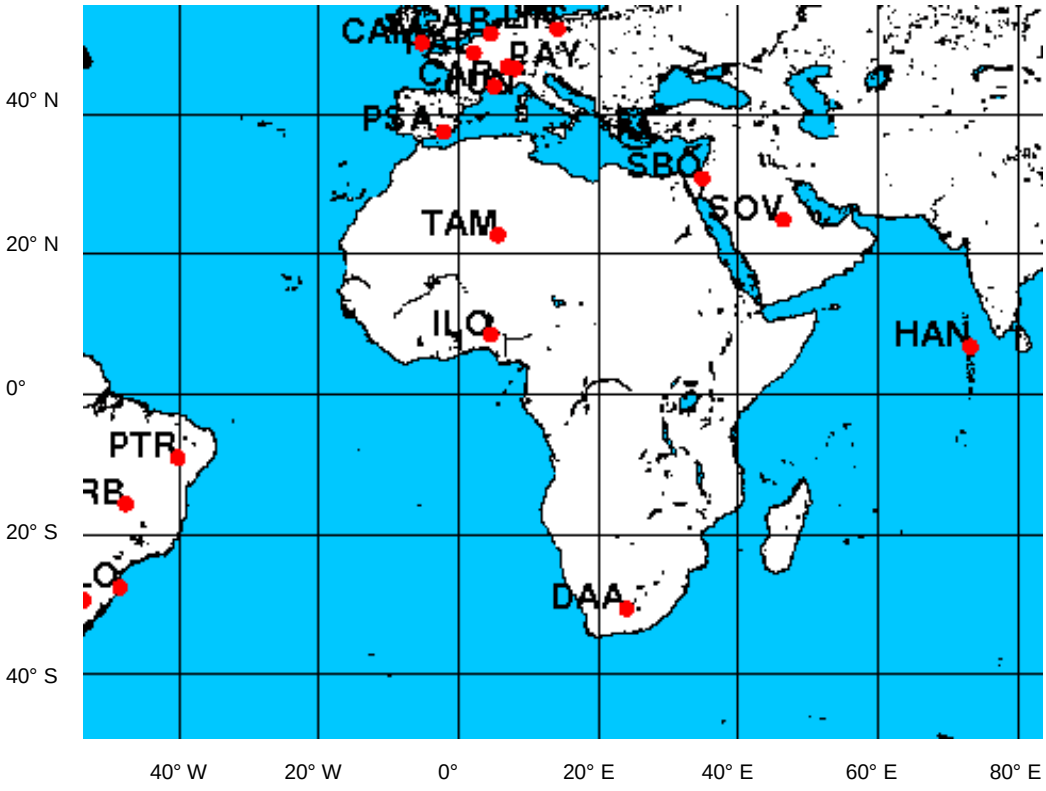

Figure 5.2. Location of BSRN sites.

information from multiple sources, including model simulations. These computations were made for a 1-year period that may not match the actual year being processed. Therefore, it is not a true observational dataset and does not account for interannual variability in aerosol properties. The UMD_SRB-F model incorporates the observed monthly variability of AOD, but uses default values of the absorbing properties, which are not currently observed on a large spatial scale. Although neither option is ideal, the motivation of this work is to examine the relative influence of these advantages and disadvantages through evaluation of derived DSSF against ground observations.

5.3. Evaluation against ground measurements over land

Ground measurements of DSSF from the Baseline Surface Radiation Network (BSRN) (Ohmura et al. 1998) are used for validation of the *Meteosat-7* derived fluxes. The red dots in Figure 5.2 indicate BSRN observing sites as of 2008. The current evaluation is conducted with data from January – October 2004, during which the available stations within Africa and surrounding regions are Tammanrasett (TAM) in northwestern Africa, De Aer (DAA) in southern Africa, and Sede Boqer (SBO) in Israel. Observations of DSSF at the BSRN sites are available at 1 minute intervals. Analysis is conducted for instantaneous measurements corresponding to the satellite observation times.

Figures 5.3 – 5.5 show the evaluation of fluxes produced by the UMD_SRB-R and UMD_SRB-F models against ground observations at the three BSRN sites for instantaneous clear-sky only cases for the January to October 2004. The clear-sky determination is made according to the *Meteosat-7* cloud detection algorithm. Both

versions of the *Meteosat-7*-based model produce better representations of clear-sky fluxes than what is seen in the Land SAF clear-sky flux validation at Agoufou and Banizoumbou for 2006. At those stations, the average biases of the instantaneous fluxes are on the order of 60 Wm^{-2}, with some individual months reaching values closer to 100 Wm^{-2}. The smaller biases achieved with the UMD_SRB research versions indicate the advantage of the implementing a more realistic aerosol treatment.

Although both versions of the UMD_SRB radiative flux inference schemes produce more accurate fluxes than the Land SAF algorithm, large differences occur between the two UMD_SRB schemes. Superior performance is seen using the aerosol climatology (UMD_SRB-R) rather than the monthly mean AOD values observed by MODIS (UMD_SRB-F). While in principle the observed AOD values should lead to higher accuracy, these results highlight the importance of the more complete characterization of the aerosol absorbing properties in the UMD_SRB-R model. In the UMD_SRB-F model, the fairly high static values of SSA (0.89) and asymmetry parameter (0.95) lead to higher transmission and less extinction and backscatter of radiation in the flux retrieval. This can create a positive bias in DSSF when the static values are not representative of the observed atmosphere. Actual values of SSA and asymmetry parameter at SBO are available from AERONET observations for the period of the study and they confirm that the assumed asymmetry parameter is too high, contributing to the positive bias. More information on the observed aerosol characteristics at TAM (currently unavailable) are necessary to explain the negative bias of the UMD_SRB-F model at TAM.

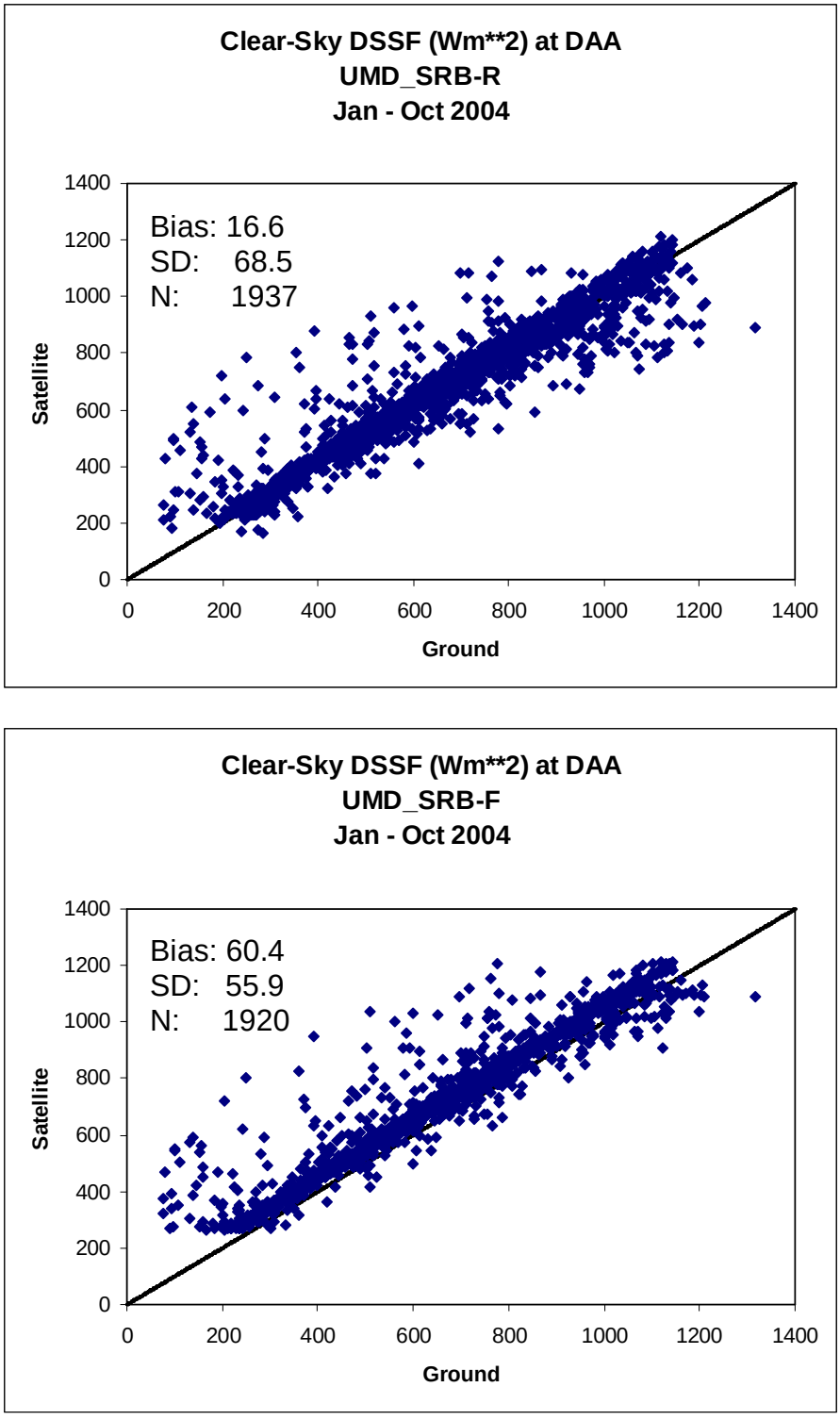

Figure 5.3. Comparison of *Meteosat-7* instantaneous clear-sky DSSF and ground measurements at DAA for Jan – Oct 2004 for UMD_SRB-R (top) and UMD_SRB-F (bottom).

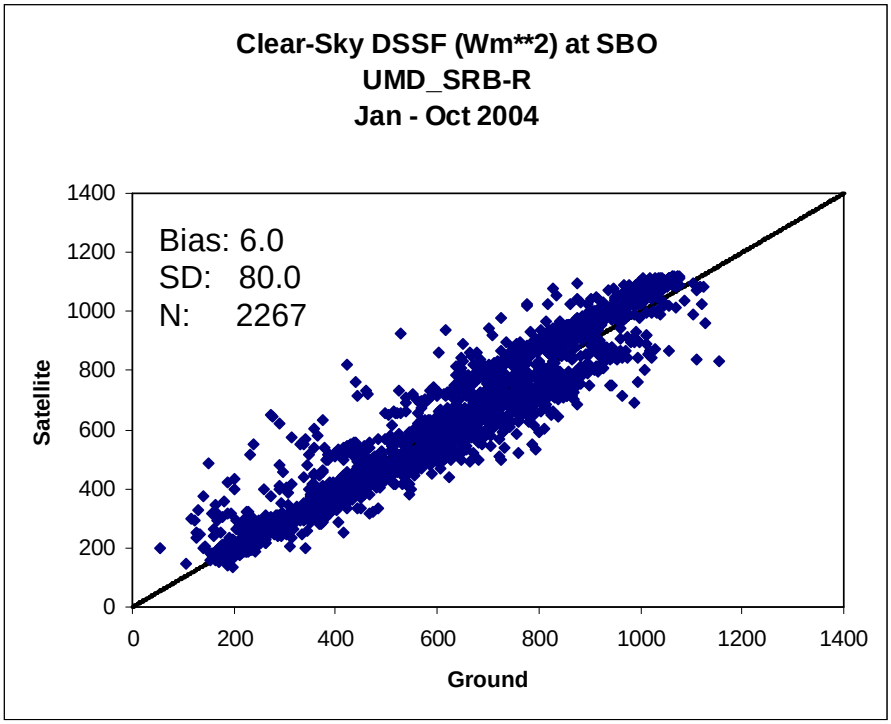

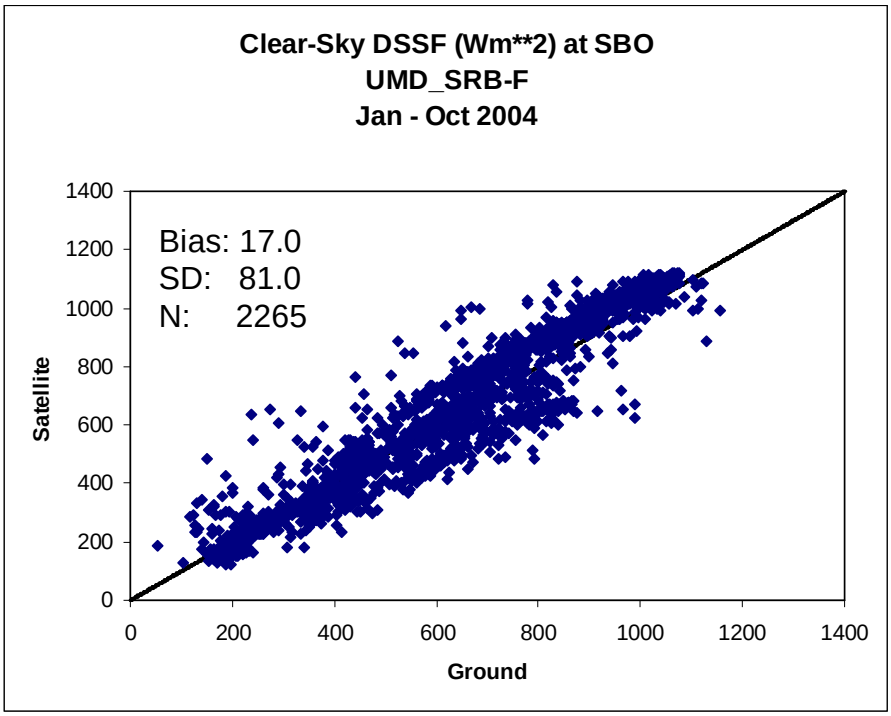

Figure 5.4. As in Figure 5.3 but for SBO.

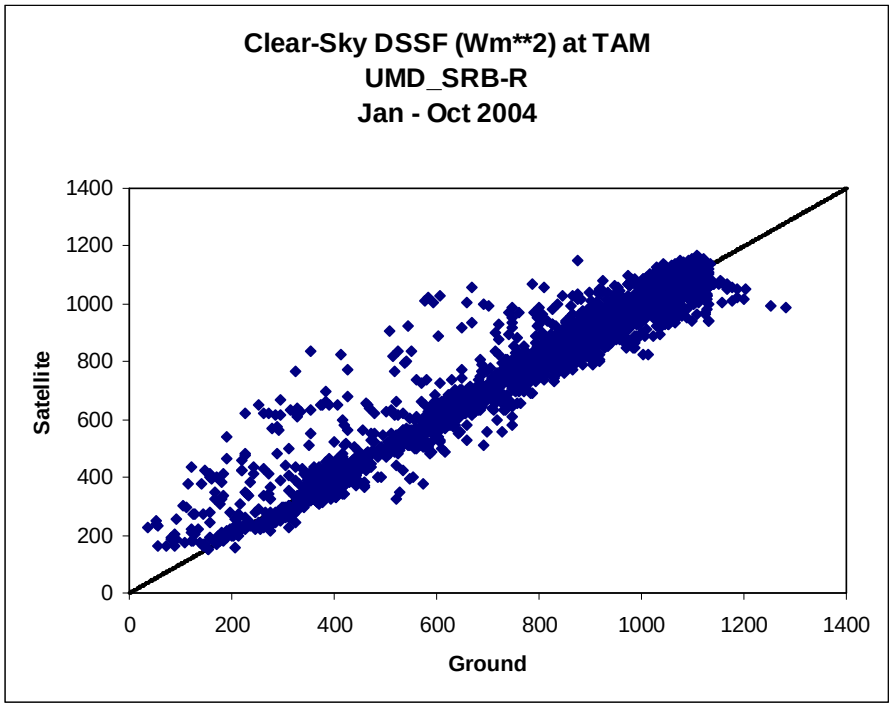

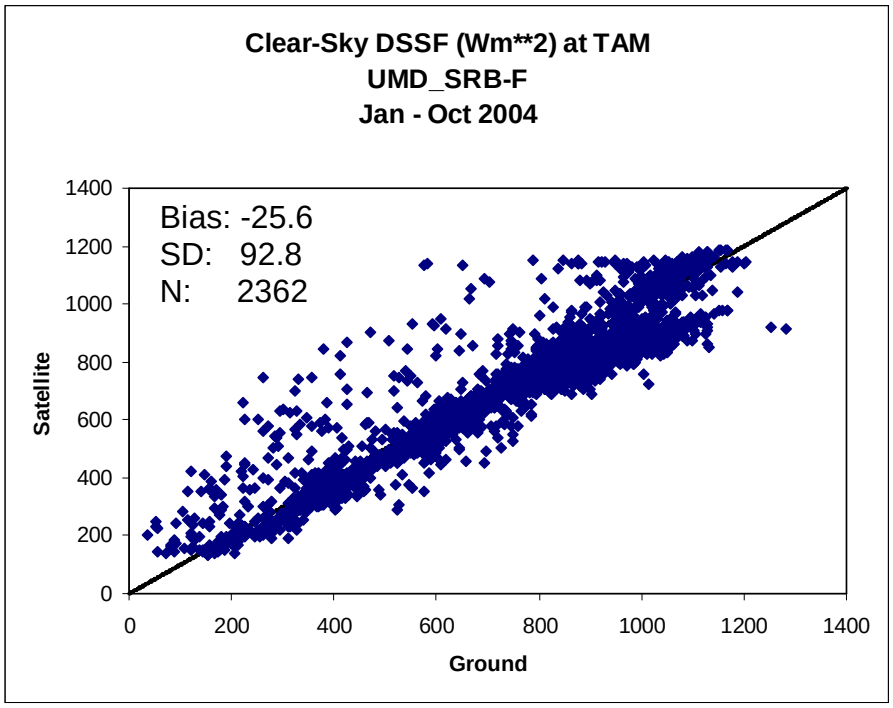

Figure 5.5. As in Figure 5.3 but for TAM.

These results quantify the degree of improvement that can be achieved by incorporating more sophisticated aerosol treatment in flux retrieval algorithms. In comparison to the evaluation of DSSF conducted with the Land SAF algorithm, biases are reduced by about 30 – 50 Wm^{-2} using the research versions of the UMD_SRB model. The approach of incorporating observed aerosol products in the radiative flux inference scheme contributes to the improvement, but the importance of aerosol absorbing properties is shown to be equally significant. This factor should also be considered in the implementation of a new aerosol treatment for the Land SAF DSSF forcing database.

5.4. Evaluation against ground measurements over ocean

Comparisons are also done over the Atlantic ocean. The research versions of the UMD_SRB model are compared to the original version (designated UMD_SRB-O) that is run operationally with very limited aerosol information. In addition to the aerosol differences in the versions, UMD_SRB-O differs from the others because it is driven with the ISCCP D1 cloud analysis at 2.5° x 2.5° resolution rather than cloud information from *Meteosat-7*. To minimize any advantage that may be due to resolution, the Meteosat-derived fluxes used in the comparison are first upscaled to match the resolution of the UMD_SRB-O fluxes.

The Prediction and Research Moored Array in the Atlantic (PIRATA) dataset (described at http://www.pmel.noaa.gov/pirata/) is used over three water locations in the Atlantic Ocean given by the coordinates in the first column of Table 5.1. DSSF values at the buoy sites are measured at 2-minute intervals but only daily means are reported. Since clear-sky-only conditions cannot be extracted from daily means, this

evaluation compares daily mean all-sky DSSF values from the UMD_SRB model versions to the PIRATA ground measurements. Results are based on the month of May 2004, and are given in Table 5.1. Both the UMD_SRB-R and UMD_SRB-F models perform better than the operational model. Since the impacts of the aerosol treatments have less influence in the all-sky daily average than in the instantaneous clear-sky cases, it is possible that some of the improvement can be attributed to better cloud detection with the *Meteosat-7* algorithm vs. the ISCCP D1 cloud information. Interestingly, the bias in the UMD_SRB-F model is even lower than the bias in the UMD_SRB-R model, a result that did not occur over land. This result suggests an area for further study, as the impact of AOD vs. other aerosol absorbing and scattering properties on flux retrievals may differ for land and water.

Table 5.1 Evaluation of daily average all-sky DSSF derived with the UMD_SRB-R, UMD_SRB-F, and UMD_SRB-O models in comparison to measurements at PIRATA buoy sites for May 2004.

Buoy Site	**Bias (Wm^{-2})**			**RMSE (Wm^{-2})**			**N**		
	-R	**-F**	**-O**	**-R**	**-F**	**-O**	**-R**	**-F**	**-O**
0N / 23W	7.02	2.93	2.68	13.27	12.80	21.96	30	30	30
0N / 35W	3.4	1.06	8.97	11.99	13.07	28.85	30	30	28
8N / 38W	2.35	-1.04	16.36	9.74	10.60	20.87	30	30	27
Combined	**4.26**	**0.98**	**9.33**	**11.67**	**12.16**	**23.89**	**90**	**90**	**85**

Chapter 6: Radiation Budget over Africa

The focus of this chapter is to use the radiative flux information derived from *Meteosat-7* to characterize the spatial and temporal variation in DSSF and surface albedo that occur over the African continent.

6.1. Variation in DSSF

Figure 6.1 shows the monthly mean DSSF derived with the UMD_SRB-R model for the months of January, April, July, and October 2004. In January, maximum DSSF values exceeding 325 Wm^{-2} occur in southwest Africa. Values range from 225 – 275 Wm^{-2} for the majority of the region bounded by 15° N to 15° S, with the exception of a band of lower DSSF from 0 - 10° S. This corresponds to the ITCZ, where heavy cloud cover reflects the incoming solar radiation. A reduction in DSSF due to persistent marine stratocumulus clouds off the coast of Namibia in southwest Africa can also be seen. Above 15° N the pattern is zonal with values decreasing poleward from 175 to 125 Wm^{-2}. The relative homogeneity of the land surface in the Saharan Desert along with the lack of cloudiness lead to this zonal pattern.

In April the region north of 10° N experiences DSSF values over 300 Wm^{-2} while values range from 200 – 275 Wm^{-2} in regions south of 10° S. A slight northward shift in the ITCZ is observable by the diminished DSSF values between 5° N and 8° S. Despite being located in the same latitude band as the ITCZ, the Horn of

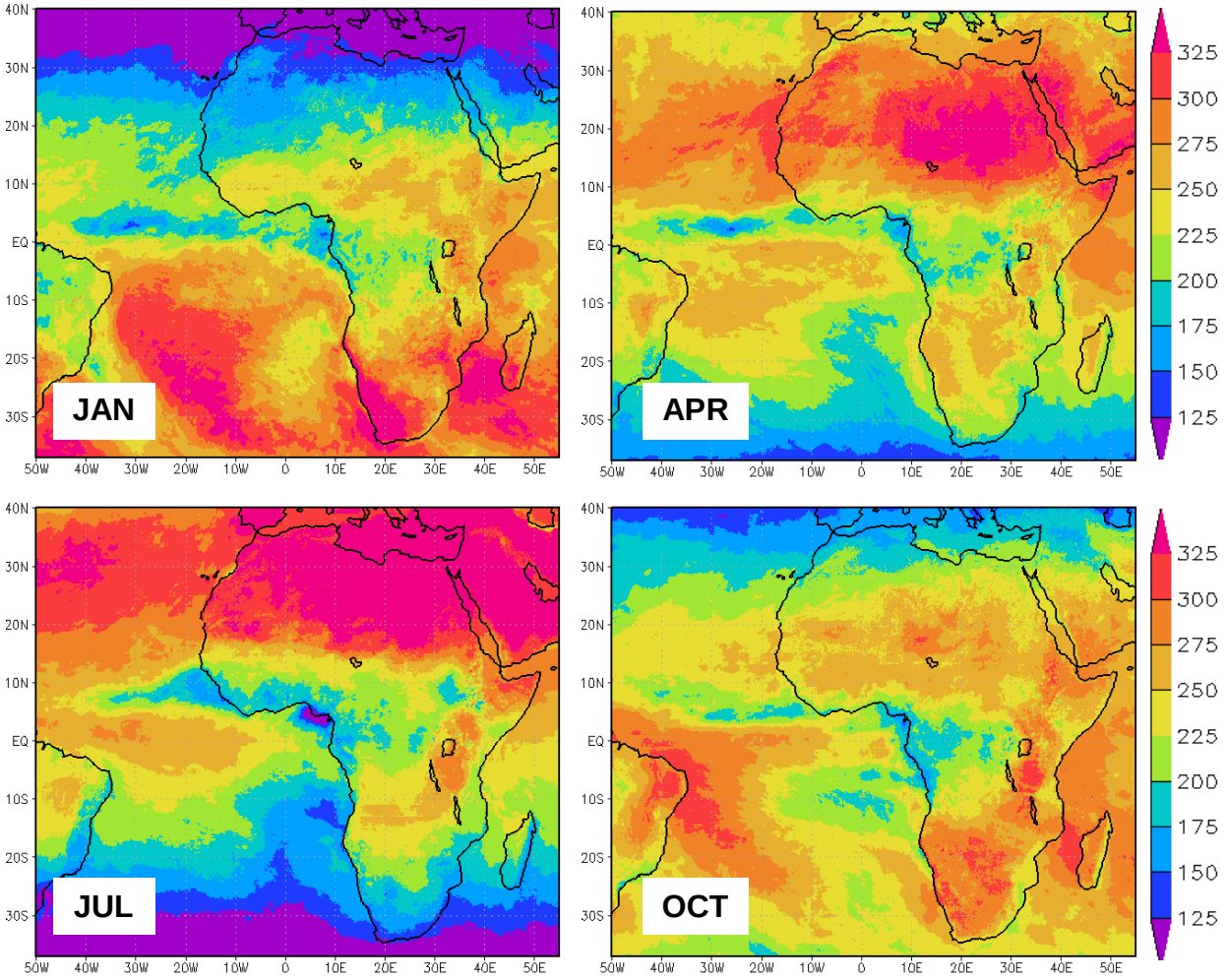

Figure 6.1. Monthly mean DSSF (Wm^{-2}) for January, April, July, and October 2004.

Africa does not experience the same drop in DSSF. The mountains of the Great Rift. Valley produce a rain shadow that keeps the region more arid than western equatorial Africa. This effect can be seen in all panels of Figure 6.1.

By July, DSSF values exceed 325 Wm^{-2} in nearly all parts of the continent north of 10° N. The ITCZ is strongly evident by the band of DSSF values in the range of 150 – 200 Wm^{-2} from 10° N to 5° S. Minimum values of less than 150 Wm^{-2} occur at the southern tip of Africa.

In October the DSSF values in the Sahara drop to 250 – 275 Wm^{-2}. The ITCZ returns to about the same position as April, with DSSF values less than 200 Wm^{-2} between 5° N and 10° S. The impact of marine stratocumulus clouds off the southwest coast of Africa is less prominent than in the other seasons. Maximum values of 300 – 325 Wm^{-2} occur mainly in southern Africa.

6.2. Surface Albedo

Surface albedo measures the fraction of incoming solar radiation reflected to space. Information on surface albedo is a vital input to regional- and global-scale climate models as it influences the redistribution of energy at the earth's interface and also impacts moisture availability. Satellites provide information useful for deriving surface albedo at various spatial scales for modeling applications. One of the earliest estimates of surface albedo over Africa was derived by Rockwood and Cox (1978) using SRS-1 satellite brightness temperatures and aircraft data from the Global Atmospheric Research Program (GARP) Atlantic Tropical Experiment (GATE). Estimates have also been derived from NOAA AVHRR data (Saunders 1990; Song and Gao 1999; Strugnell et al. 2001), *Meteosat-5/7* (Pinty et al. 2000a), MODIS (Lucht et al. 2000; Schaaf et al. 2002), the Clouds and the Earth Radiant Energy System (CERES) sensor aboard the *Terra* satellite (Kato et al. 2005), and Meteosat Second Generation (MSG) (Geiger et al. 2004).

Figure 6.2 shows the *Meteosat-7* monthly mean surface albedo computed for January, April, July, and October 2004. In all seasons, albedos greater than 0.5 occur in parts of the Sahara. Slight variation in the magnitude of the albedo throughout the

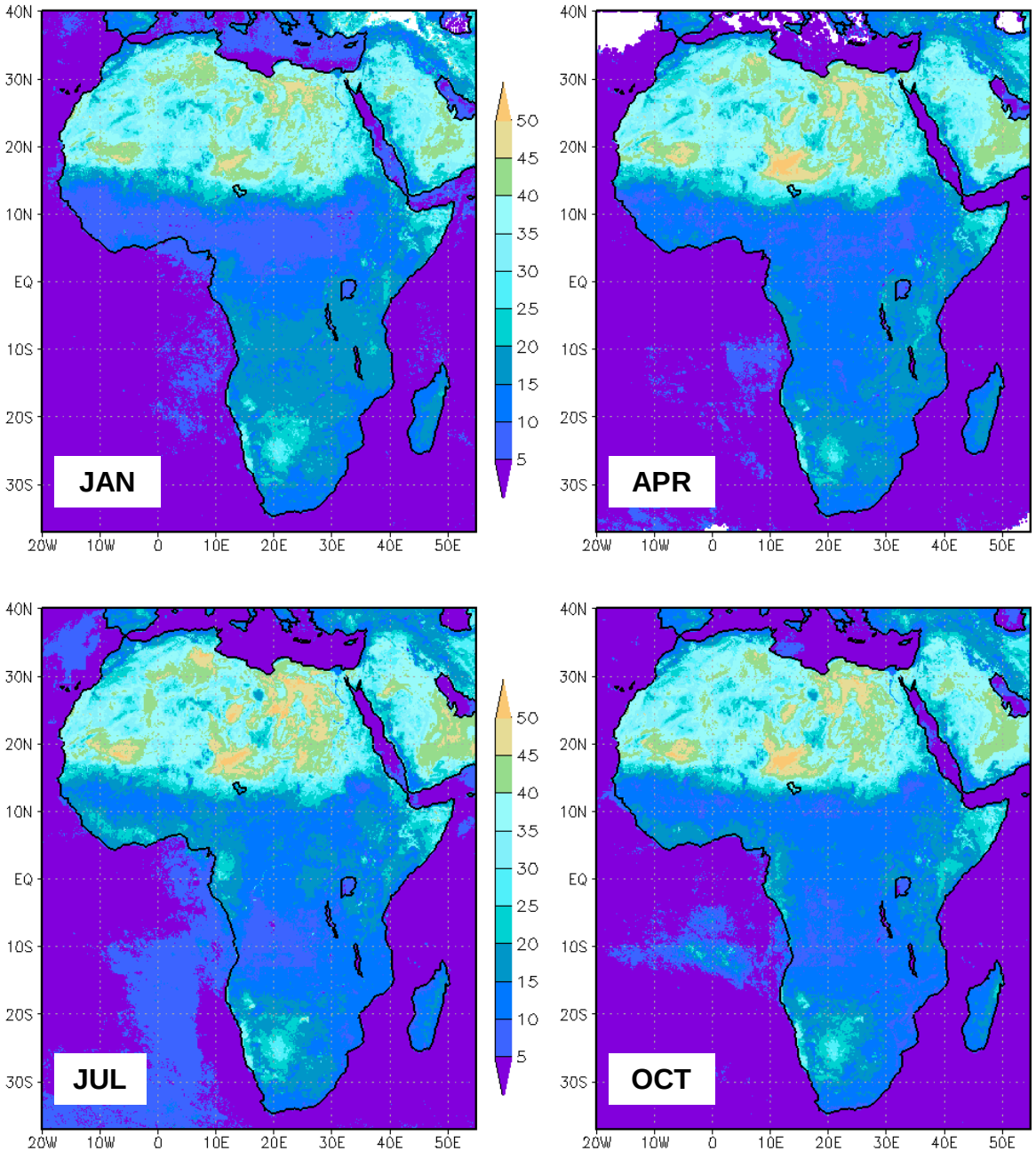

Figure 6.2. Monthly mean surface albedo for January, April, July, and October 2004.

seasonal cycle occurs in these regions, with the minimum albedo occurring in January. Several mountainous parts of the Sahara receive slightly more rainfall than surrounding areas, resulting in albedos less than 0.25. Albedos in the Kalahari and Namib Deserts in southern Africa are considerably lower than those in the Sahara, with maxima of 0.3. The albedo remains nearly invariant throughout the year in these deserts, as well as in the semi-arid regions of Somalia and Ethiopia in eastern Africa. The largest seasonal changes in albedo occur in the region between 10° N to 15° S, where the progression of monsoon rainfall and the annual cycle of deciduous forests cause more pronounced changes in land surface conditions.

Seasonal changes in surface albedo derived from Meteosat in 1996 were analyzed by Pinty et al. (2000b) and Govaerts (2002). In addition to the seasonal decrease in albedo caused by monsoon rains, decreases were also observed in the dry season due to biomass burning which peaks from November – January in the northern hemisphere and July – August in the southern hemisphere (Cooke 1996). The impact of biomass burning was stronger in the Sahel than in the southern hemisphere. Within the Sahel, surface albedo reduction was larger (8%) at the northern border where vegetation is sparse and normally has a higher albedo than in the thickly vegetated southern portion. Albedo decreases due to biomass burning did not exceed 5% in the southern hemisphere. Impact of fires in the northern hemisphere were found to be more significant in reducing albedo than the rainfall effect, such that the albedo was lower during the burning season than during the rainy season. A similar feature was found in the *Meteosat-7* data derived with the UMD_SRB-R model where albedos in the Sahel were 0.1 – 0.15 higher in July (Figure 6.3).

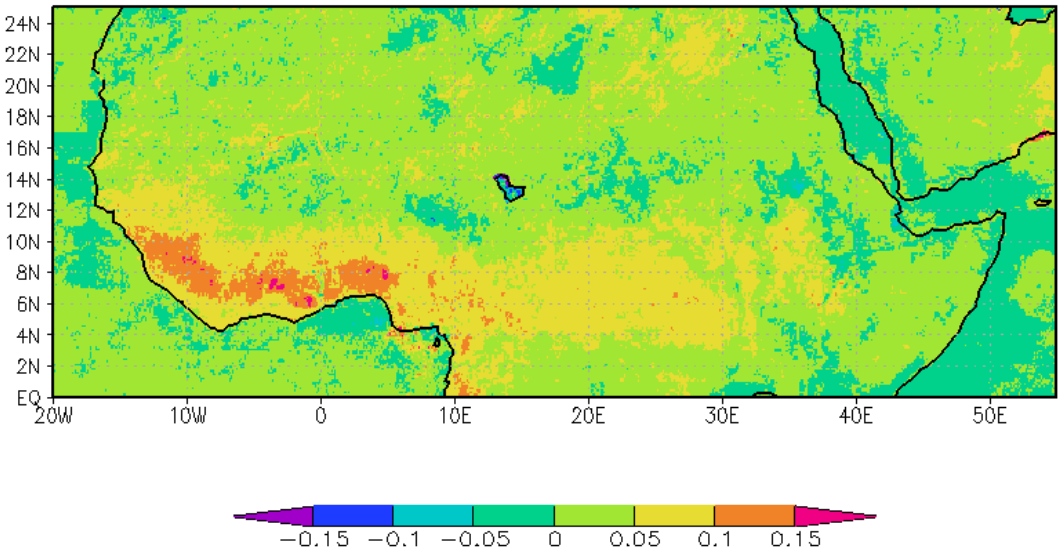

Figure 6.3. Difference in monthly mean surface albedo July 2004 minus January 2004.

Differences exist in various satellite estimates of surface albedo and Sato et al. (1989) noted that errors in albedo used in GCMs ranged from 5 – 15% for different locations and seasons. Knorr et al (2001) found surface albedos larger than 0.35 throughout the Sahara desert with maximum values above 0.5 using *Meteosat-7* satellite observations, similar to those derived here. AVHRR estimates do not exceed 0.4 throughout the Sahara region (Strugnell et al. 2001; Wei et al. 2001), while MODIS estimates are in between these values (Tsvetaskinskaya et al. 2002). The most recently derived MSG values also exceed MODIS estimates, particularly in the visible portion of the spectrum (Geiger et al. 2004). Such differences may significantly impact rainfall predictions by GCMs. Knorr et al. (2001) ran the ECHAM4 model with higher albedo estimates from Meteosat against a control run using the model's nominal albedo estimates. Precipitation was reduced by 30

mm/month in the Sahel and 20 mm/month in the Sahara, bringing model predictions much closer in line with observations. This illustrates the need for careful attention to surface albedo inputs used for model forcing.

The *Meteosat-7* surface albedo values of this study are computed as a ratio of the upwelling and downwelling radiative fluxes. Fluxes are derived for clear-sky and cloudy-sky conditions at both the surface and TOA at instantaneous, hourly, daily, and monthly timescales. This makes it possible to study both surface and TOA albedo under all conditions (clear and cloudy). The effects of environmental conditions such as rainfall can be assessed by using the daily average products. This section presents the methodology and a brief overview of surface albedo results. Comprehensive analysis will be completed when more years of data have been produced.

.

Chapter 7: Summary

The key objective of this work was to develop inference schemes that will result in information needed for addressing several issues of priority to the GEWEX program as articulated in the CEOP framework, namely:

1. To aid in the investigation of processes that impact the hydro-climate of the Indian and African monsoon regions at local and regional scales by deriving information on clouds and radiative fluxes at high temporal and spatial resolution from the *Meteosat-5* and *Meteosat-7* satellites

2. To apply the information to document the evolution of cloud systems throughout the Indian monsoon cycle, to investigate the impact of aerosols on the Indian monsoon and on surface radiative fluxes, and to characterize the seasonal changes in the surface albedo and radiation regimes in Africa.

The first objective was accomplished by demonstrating the transferability of methods to derive clouds and radiative fluxes from the GOES satellites over North America to the Meteosat satellites over the monsoon regions of interest. This includes the adaptation of cloud detection tests from the GOES channels to those of the Meteosat systems. The UMD_SRB radiative flux inference scheme used operationally for North America was modified to handle the challenges of the Indian and African monsoon regions. Specifically, a correction is used to better represent radiative transfer at high elevations such as the Tibetan Plateau region, and new sources of aerosol information are incorporated to account for the spatial and seasonal variability of the aerosol load in the monsoon regions.

Four specific questions to be addressed with the newly developed information as raised in Chapter 1 and the findings are summarized here:

1. How does the spatial distribution and diurnal cycle of clouds and convection change as the Indian monsoon evolves through the pre-monsoon, peak-monsoon, and post-monsoon seasons?

The cloud patterns for two years with climatologically normal Indian monsoon rainfall were studied. The evolution of the monsoon is seen as an increase in cloudiness from 10° N – 20° N during the monsoon build-up phase, a northward progression of increased cloudiness to 25° N during peak monsoon, and a retreat of maximum cloudiness to 5° N – 15° N during the monsoon dissipation phase. The daytime (8-15 LST) diurnal cycle of total cloud amounts is generally flat during the pre-monsoon season, U-shaped during peak-monsoon, and ascending toward an afternoon peak in the post-monsoon season. Low clouds dominate the Tibetan Plateau and northern Arabian Sea while high clouds are more frequent in the southern Bay of Bengal and Arabian Sea. An afternoon peak in high clouds is most prominent in coastal India and the Bay of Bengal. Afternoon convection peaks earlier over water than land. Comparison of cloud amounts from *Meteosat-5*, ISCCP D1, and model output from the ERA-40 Re-analysis and the NCEP/NCAR Re-analysis indicates the largest disparity among cloud amounts from the various sources during peak-monsoon.

2. How does the aerosol load in the Indo-Gangetic Basin impact the Indian monsoon?

The "Elevated Heat Pump" hypothesis was re-evaluated using *Meteosat-5* cloud data and recent aerosol information from MODIS and MISR. High and low aerosols years from the period 2000 – 2005 were contrasted to determine whether a high aerosol load in the Indo-Gangetic Basin led to a northward shift and enhancement of monsoon precipitation as proposed by the EHP hypothesis. It was found that in some aspects, observations are in agreement with the hypothesis but not in all aspects of it. Anomalous warming over the Tibetan Plateau due to aerosol absorption did occur as predicted in the high aerosol year (although apparently not induced by aerosol absorption), but it did not act as a mechanism to increase precipitation in the Himalayan foothills and northern India. However, suppression of precipitation in southern India and enhancement in central China and Korea was observed as predicted.

Other plausible factors were investigated to explain the discrepancies between the *Meteosat-5* derived cloud and convection patterns and those predicted by the EHP hypothesis. It was determined that the numerical model simulations used as a basis to develop the hypothesis may have been flawed because they did not incorporate ocean/atmosphere coupling or aerosol semi-direct effects. The latter appear to be responsible for reduced precipitation in the western portion of the IGB under high aerosol load. Additionally, many anomalous dynamical factors combined to make 2004 an exceptional drought year, and may have masked evidence of the EHP effect.

3. How are flux retrieval algorithms in the African monsoon region impacted by the source of aerosol optical depth information and the incorporation of aerosol absorbing properties?

Recent improvement in observational datasets of aerosol properties have been leveraged to test new aerosol treatments in the UMD_SRB radiative flux inference scheme. One method used actual observed AOD values from MODIS but relied on default values of aerosol absorbing properties. The other method used an aerosol dataset that contains detailed information on the spatial and temporal variations in both AOD and aerosol absorbing properties, but did not correspond in time to the year of the flux data being retrieved. Both of the methods tested performed better than the Land SAF DSSF algorithm used to provide surface radiative forcing to the AMMA LSMs. This algorithm greatly overestimates DSSF in Africa due to poor representation of aerosols. While the use of observed AOD values from MODIS reduced the bias of the flux retrievals by about 30 Wm^{-2}, accounting for the absorbing properties improved the retrievals even further.

4. How do the surface albedo and radiation regimes change seasonally over Africa?

The evolution of DSSF and surface albedo for the year 2004 was shown. Maximum values of DSSF exceeding 325 Wm^{-2} occured over the Sahara Desert in April and July and over the Kalahari Desert in January. DSSF values in the ITCZ were 175 – 225 Wm^{-2} on average. Lowest values of DSSF were less than 125 Wm^{-2}, occurring on the northern border of Africa in January. October showed the least extreme range of DSSF, with only a few regions exceeding 300 Wm^{-2}. Surface albedos greater than 0.45 occurred in the Sahara Desert year-round, while the maximum albedo of the southern deserts remained steady at 0.25 throughout all

seasons. The most seasonal variation in albedo occurred from 10° N to 15° S due to changing land and soil moisture conditions.

This research developed the tools to meet the needs for high-resolution cloud and radiative flux information that can be used as forcing and validation data for local and regional-scale modeling as implemented in the CEOP program. Four applications of the information have been demonstrated here but its potential uses are much wider. Future direction of this work includes:

- Developing a nighttime cloud detection algorithm for *Meteosat-5* and -*7* to improve the utility of the data set for validating numerical model-produced clouds throughout the full diurnal cycle.

- Testing the effect of other aerosol data sources (such as MISR and the Goddard Institute for Space Studies (GISS) products) on the radiative flux inference scheme.

- Processing the entire 8 – 9 year records of the *Meteosat-5* and -*7* data to produce more robust cloud, radiative flux, and surface albedo climatologies.

- Comparing the patterns of convective clouds in the Indian and African monsoon regions to gain insights on the differences in the monsoon rainfall mechanisms of the two regions.

- Investigating the impact of African dust on convection.

Other investigators are also beginning to make use of the information developed through this research. The *Meteosat-5* cloud analyses are already being

used for an inter-comparison of Model Output Location Time Series (MOLTS) data with satellite-derived cloud products. It is hoped that the data that has been made available by this research will be instrumental in numerous other investigations of monsoon dynamics and climate prediction.

Bibliography

Ackerman, S. A., K. I. Strabala, W. P. Menzel, R. A. Frey, C. C. Moeller, and L. E. Gumley, 1998: Discriminating clear sky from clouds with MODIS. *J. Geophys. Res.*, **103**, 32,141-32,157.

Augustine, J. A., J. J. DeLuisi, and C. N. Long, 2000: SURFRAD—A national surface radiation budget network for atmospheric research. *Bull. Amer Meteor. Soc.*, **81**, 2341-2357.

Babu, S. S., K. K. Moorthy, and S. K. Satheesh, 2004: Aerosol black carbon over Arabian Sea during intermonsoon and summer monsoon seasons. *Geophys. Res. Lett.*, **31,** L06104, doi:10.1029/2003GL018716.

Bamzai, A. S., and J. Shukla, 1999: Relation between Eurasian Snow Cover, Snow Depth, and the Indian Summer Monsoon: An Observational Study. *J. Climate*, **12**, 3117-3132.

Barkstrom, B. R., E. F. Harrison, and R. B. Lee III, 1990: Earth Radiation Budget Experiment—Preliminary seasonal results. *Eos, Trans. Amer. Geophys. Union*, **71**, 297 and 304.

Barros, A. P., G. Kim, E.Williams, and S.W. Nesbitt, 2004: Probing orographic controls in the Himalayas during the monsoon using satellite imagery, *Nat. Haz. and Earth Sys. Sci*., **4**, 29-51.

Bergman, J. W., and M. L. Salby, 1996: Diurnal variations of cloud cover and their relationship to climatological conditions. *J. Climate*, **9**, 2802-2820.

Bollasina, M., and S. Nigam, 2008: Absorbing aerosols and summer monsoon evolution over South Asia: An observational portrayal. *J. Climate,* in press.

Bosilovich, M. G. and R. Lawford, 2002: Report on the Coordinated Enhanced Observing Period (CEOP) International Workshop. Bull. Amer. Meteor. Soc., **83**, 1495-1499.

Bothwell, G. W., Hansen, E. G., Vargo, R. E. and K. C. Miller, 2002: The Multi-angle Imaging SpectroRadiometer science data system, its products, tools and performance. *IEEE Trans. Geosci. Remote Sens.*, **40** (7), 1467-1476.

Brest, C. L., and W. B. Rossow, 1992: Radiometric calibration and monitoring of NOAA AVHRR data for ISCCP. *Int. J. Remote Sens.*, **13**, 235-273.

Brown, P., 1989: Accessing the Arizona Meteorological Network by Computer. The University of Arizona, College of Agriculture, Tucson, AZ 85721.

Chakraborty, A., and T. N. Krishnamurti, 2003: A coupled model study on ENSO, MJO and Indian summer monsoon rainfall relationships, *Meteor. and Atmos. Physics*, 84, 243-254.

Chang, C.P., P. Harr, and J. Ju, 2001: Possible Roles of Atlantic Circulations on the Weakening Indian Monsoon Rainfall–ENSO Relationship. *J. Climate*, **14**, 2376–2380.

Cherchi, A., and A. Navarra, 2003: Reproducibility and predictability of Asian summer monsoon in the ECHAM4-GCM. *Climate Dyn.*, **20**, 365-379.

Chevallier, F., and G. Kelly, 2002: Model clouds as seen from space: Comparison with geostationary imagery in the 11-mm window channel. *Mon. Wea. Rev.*, **130**, 712–722.

Chin, M., P. Ginoux, S. Kinne, B. N. Holben, B. N. Duncan, R. V. Martin, J. A. Logan, A. Higurashi, and T. Nakajima, 2002: Tropospheric aerosol optical

thickness from the GOCART model and comparisons with satellite and sunphotometer measurements. *J. Atmos. Sci.* **59,** 461-483.

Chou, C., J. D. Neelin, and H. Su, 2001: Ocean-atmosphere-land feedbacks in an idealized monsoon. *Quart. J. Royal Metoc. Soc*., **127**, 1869-1892.

Chung, C., V. Ramanathan, and J. T. Kiehl, 2002: Effects of the South Asian absorbing haze on the northeast monsoon and surface–air heat exchange. *J. Climate*, **15**, 2462-2476.

Chylek, P., M. K. Dubey, U. Lohmann, V. Ramanathan, Y. J. Kaufman, G. Lesins, J. Hudson, G. Altmann, and S. Olsen, 2006: Aerosol indirect effect over the Indian Ocean. *Geophys. Res. Lett.*, **33**, L06806, doi:10.1029/2005GL025397.

Cooke, W. F., B. Koffi, and J.-M. Gr6goire, 1996: Seasonality of vegetation fires in Africa from remote sensing data and application to a global chemistry model. *J. Geophys. Res*., **101**, 21,051-21,065.

Dai, A., 2001: Global precipitation and thunderstorm frequencies. Part II: Diurnal variations. *J. Climate,* **14**, 1112–1128.

d'Entremont R. and Gustafson G., 2006: Cloud Detection and Property Retrieval Across The Day/night Terminator. 14th Conference on Satellite Meteorology and Oceanography.

Derrien, M., and H. Le Gleau, 2005: MSG/SEVIRI cloud mask and type from SAFNWC. *Int. J. of Rem. Sens*., **26**, 4707-4732.

Dugam, S. S., S. B. Kakade, and R. K. Verma, 1997: Interannual and long-term variability in the North Atlantic Oscillation and Indian summer monsoon rainfall. *Theor. Appl. Climatol.* **58** 21–29.

Dybbroe, A., 2001: The retrieval of the SAFNWC cloud mask and cloud type from AVHRR and SEVIRI at high latitudes, SAFNWC Action PT06-04, Available at http://www.smhi.se/saf under Documents.

Flohn, H., 1968: Contributions to a meteorology of the Tibetan Highlands. Atmos. Sci. Paper No. 130, Colorado State University, Fort Collins, CO 80523,120 pp.

Fuller, D. O., and C. Ottke, 2002: Land cover, rainfall and land-surface a lbedo I n West Africa. *Clim. Change*, **54**, 181-204.

Gadgil, S., 2003: The Indian Monsoon and its variability. *Annu. Rev. Earth Planet. Sci*., **31**, 429-467.

Gambheer, A. V. and G. S. Bhat, 2001: Diurnal variation of deep cloud systems over the Indian region using INSAT-1B Pixel data. *Meteor. Atmos. Phys*., **78**, 215-226.

Geiger, B., L. Franchisteguy, D. Lajas, J.-L. Roujean, 2004: Operational derivation of land surface albedo and down-welling short-wave radiation in the framework of the Land-SAF project. Proceedings. 2004 IEEE International, 3(20-24), September 2004, 1707-1710. DOI:10.1109/IGARSS.2004.1370660.

Govaerts, Y. M., M. Clerici, and N. Clerbaux, 2004: Operational calibration of the Meteosat radiometer VIS band. *Geos. and Rem. Sens. IEEE Trans.*, **42**, 1900-1914.

Govaerts, Y. M., J. M. Pereira, B. Pinty, and B. Mota 2002: Impact of fires on surface albedo dynamics over the African continent. *J. Geophys. Res.*, **107(D22)**, 4629, doi:10.1029/2002JD002388.

Gray, W. M., and R. W. Jacobson, 1977: Diurnal variation of deep cumulus convection. *Mon. Wea. Rev.*, **105**, 1171–1188.

Grodsky S.A., and J.A. Carton, 2001: Coupled land/atmosphere interactions in the West African monsoon. *Geophys. Res. Letts.*, **28**, 1503-1506.

Gupta, S. K., D. P. Kratz, A. C. Wilber, and L. C. Nguyen, 2004: Validation of parameterized algorithms used to derive TRMM-CERES surface radiative fluxes. *J. Atmos. Oceanic Tech.*, **21**, 742-752.

Hahn, D. and J. Shukla, 1976: An apparent relationship between Eurasian snow cover and Indian monsoon rainfall. *J. Atmos. Sci*., **33**, 2461–2462.

Halthore, R. N., and Coauthors, 2005: Intercomparison of shortwave radiative transfer codes and measurements. *J. Geophys. Res.*, **110**, D11206, doi:10.1029/2004JD005293.

He, H., J. W. McGinnis, Z. Song, and M. Yanai, 1987: Onset of the Asian summer monsoon in 1979 and the effect of the Tibetan Plateau. *Mon. Wea. Rev.*, **115**, 1966-1995.

Heymsfield, A. J., and G. M. McFarquhar, 2001: Microphysics of INDOEX clean and polluted cumulus clouds. *J. Geophys. Res*., **106(D22),** 28,653– 28,673.

Holben, B. N., and Coauthors, 2001: An emerging ground-based aerosol climatology: Aerosol optical depth from AERONET. *J. Geophys. Res.*, **106,** 12,067–12,097.

Holben, B. N., and Coauthors, 1998: AERONET—A federated instrument network and data archive for aerosol characterization. *Remote Sens. Environ.*, **66,** 1–16.

Hollinger, S. E., B. C. Reinke, and R. A. Peppler, 1994: Illinois Climate Network: Site description, instrumentation, and data management. Illinois State Water Survey Circular 178, WARM Network Publication 1, 63 pp.

Hsu, N. C., J. R. Herman, J. F. Gleason, O. Torres, and C. J. Seftor, 1999: Satellite detection of smoke aerosols over a snow/ice surface by TOMS. *Geophys. Res. Lett.*, **26**, 1165-1168.

Huffman, G., R. Adler, P. Arkin, A.Chang, R. Ferraro, A. Gruber, J. Janowiak, A. McNab, R. Rudolf, and U. Schneider, 1997: The Global Precipitation Climatology Project (GPCP) combined precipitation dataset. *Bull. Am. Meteorol. Soc.*, **78**, 5-20.

IPCC, 2007: Climate Change 2007: The Physical Science Basis. Contribution of Working Group I to the Fourth Assessment Report of the Intergovernmental Panel on Climate Change [Solomon, S., D. Qin, M. Manning, Z. Chen, M. Marquis, K.B. Averyt, M. Tignor and H.L. Miller (eds.)]. Cambridge University Press, Cambridge, United Kingdom and New York, NY, USA, 996 pp.

Islam, M. N., T. Hayashi, H. Uyeda, T. Terao, and K. Kikuchi, 2004: Diurnal variations of cloud activity in Bangladesh and north of the Bay of Bengal in 2000. *Rem. Sens. Envir.,* **90**, 378-388.

Janowiak, J. E., P. A. Arkin, and M. Morrissey, 1994: An examination of the diurnal cycle in oceanic tropical rainfall using satellite and in situ data. *Mon. Wea. Rev.,* **122**, 2296–2311.

Jenamani, R. K., S. R. Kalsi, H. R. Hatwar, and S. K. Subramanian, 2007: Another deficient monsoon 2004—A comparison with drought year 2002 and possible causes. *Mausam*, **56**, 161-176.

Jenamani, R. K., 2004: Comments on periodicity in the frequency of Indian monsoon cyclonic disturbances and storms. *Mausam*, **55**, 1189-1194.

Joseph, J. H., W. J. Wiscombe, and J. A. Weinman, 1976: The delta-Eddington approximation for radiative transfer. *J. Atmos. Sci.*, **33**, 2452–2459.

Kaufman, Y., D. Tanre´, L. A. Remer, E. F. Vermote, A. Chu, and B. N. Holben, 1997: Operational remote sensing of tropospheric aerosols over land from EOS moderate resolution imaging spectroradiometer. *J. Geophys. Res.*, **102**, 17,051–17,067.

Kakade, S. B., and S. S. Dugam, 2006: Spatial monsoon variability with respect to NAO and SO. *J. Earth Syst. Sci.* **115**, 601–606

Kanamitsu, M., W. Ebisuzaki, J. Woolen, S.-K. Yang, J. J. Hnilo, M. Fiorino, and G. L. Rotter, 2002: NCEP/DOE AMIP-II reanalysis (R-2), *Bull. Am. Meteorol. Soc.*, **83**, 1631-1643.

Kato, S., F.G., Rose, and T.P., Charlock, 2005: Computation of domain-averaged irradiance using satellite-derived cloud properties. *J. Atmos. Ocean. Tech.*, **22b**, 146-164.

Kistler, R., and co-authors, 2000: The NCEP/NCAR 50-year Reanalysis. *Bull. Am. Metoc. Soc*. **82**, 247-267.

Knorr, W., Schnitzler, K.-G., and Y. Govaerts, 2001: The role of bright desert regions in shaping North African climate. *Geophys. Res. Lett.*, **28(19)**, 3489-3492.

Koike, T., 2004: The Coordinated Enhanced Observing Period – An initial step for integrated global water cycle observations. WMO Bull., **53**, 115-121.

Krishnamurthy, V. and B. N. Goswami, 2000: Indian monsoon-ENSO relationship on interdecadal timescale. *J. Climate,* **13(3),** 579-595.

Krishnamurthy, V., and J. Shukla, 2000: Intraseasonal and interannual variability of rainfall over India. *J. Climate*, **13**, 4366-4377.

Krishnamurti, T. N. and C. M. Kishtawal, 2000: A Pronounced Continental-Scale Diurnal Mode of the Asian Summer Monsoon, *Mon. Wea. Rev.*, **128**, 462-473.

Kumar, K. K., B. Rajagopalan, M. Hoerling, G. Bates, and M. A. Cane, 2006: Unraveling the mystery of Indian monsoon failure during El Nino. *Science,* **314**, 115-119. (2006); DOI: 10.1126/science.1131152.

Kumar, K. K., B. Rajagopalan, and M. A. Cane, 1999: On the weakening relationship between the Indian monsoon and ENSO. *Science*, **284** 2156. DOI: 10.1126/science.284.5423.2156.

Landsea, C. W. and W. M. Gray, 1992: The strong association between Western Sahel monsoon rainfall and intense Atlantic hurricanes. *J. Clim.*, **5**, 435-453.

Laszlo, I., H. Jacobowitz, and A. Gruber, 1988: The relative merits of narrowband channels for estimating broadband albedos. *J. Atmos. Ocanic Technol.*, **5**, 757-773.

Lau, K. M., and K. M. Kim, 2006: Observational relationships between aerosol and Asian monsoon rainfall, and circulation. *Geophys. Res. Lett.*, **33**, L21810, doi:10.1029/2006GL027546.

Lau, K.-M., M. K. Kim, and K. M. Kim, 2006: Asian summer monsoon anomalies induced by aerosol direct forcing: the role of the Tibetan Plateau. *Clim. Dyn.*, **26**, 855-864, doi:10.1007/s00382-006-0114-z.

Lau, K. M., J. Matsumoto, M. Bollasina, and H. Berbery, 2005: Diurnal variability in the monsoon region: Preliminary results from the CEOP Inter-Monsoon Studies (CIMS). CEOP Newsletter No. 5.

Lee, R. B., III, and Coauthors, 1998: Prelaunch calibrations of the Clouds and Earth's Radiant Energy System (CERES) Tropical Rainfall Measuring Mission and Earth Observing System Morning (EOS-AM1) spacecraft thermistor bolometer sensors. *IEEE Trans. Geosci. Remote Sens.*, **36**, 1173-1185.

Leroy M., and Coauthors, 1997: Retrieval of atmospheric properties and surface bidirectional reflectances over the land from POLDER. *J. Geophys. Res.*, **102**, pp17023-17037.

Li, C. and M. Yanai, 1996: The onset and interannual variability of the Asian summer monsoon in relation to land-sea thermal contrast. *J. Climate*, **9**, 358-375.

Li, J., W. P. Menzel, Z. Yang, R. A. Frey, and S. A. Ackerman, 2003: High-spatial-resolution surface and cloud type classification from MODIS multispectral band measurements. J. Appl. Meteor., 42(2), 204-226.

Li, X., R. T. Pinker, M. M. Wonsick, and Y. Ma, 2007: Towards improved satellite estimates of short-wave radiative fluxes: Focus on cloud detection over snow. Part I: Methodology. *J. Geophys. Res.*, **112**, D07208, doi:10.1029/2005JD006698.

Li, Z., H. G. Leighton, and R. D. Cess, 1993: Surface net solar radiation estimated from satellite measurements: Comparisons with tower observations. *J. Climate*, **6**, 1764-1772.

Liou, K. N., W.-L. Lee, and A. Hall, 2007: Radiative transfer in mountains: Application to the Tibetan Plateau. *Geophys. Res. Lett.*, **34**, L23809, doi:10.1029/2007GL031762.

Liu, H. and R. T. Pinker, 2008: Radiative Fluxes from Satellites: Focus on aerosols. *J. Geophys. Res.*, In press.

Liu, H., R. T. Pinker, M. Chin, B. Holben, and L. Remer, 2008: Synthesis of information on aerosol optical properties. *J. Geophys. Res.*, **113**, doi:10.1029/2007JD008735.

Liu, H., R. T. Pinker, and B. Holben, 2005: A global view of aerosols from merged transport models, satellite, and ground observations. *J. Geophys. Res.*, **110**, doi:10.1029/2004JD004695.

Lucht, W., C. B. Schaaf, and A. H. Strahler, 2000. An algorithm for the retrieval of albedo from space using semiempirical BRDF models. *IEEE Trans. Geosci. Remote Sens.*, **38(2)**, 977– 998.

Luo, H. and M. Yanai, 1984: The large-scale circulation and heat sources over the Tibetan Plateau and surrounding areas during the early summer of 1979. Part II: Heat and moisture budgets. *Mon. Wea. Rev.*, **112**, 966-989.

McGarry, M. M, and R. J. Reed, 1978: Diurnal variations in convective activity and precipitation during Phases II and III of GATE. *Mon. Wea. Rev.*, **106**, 101–113.

McGill, M. J., M. A. Vaughan, C. R. Trepte, W. D. Hart, D. L. Hlavka, D. M. Winker, and R. Kuehn, 2007: "Airborne validation of spatial properties

measured by the CALIPSO lidar", *J. Geophys. Res.*, **112**, D20201, doi:10.1029/2007JD008768.

Meehl G.A., J.M. Arblaster and W.D. Collins, 2008: Effects of black carbon aerosols on the Indian monsoon, *J. Climate*, **21**, 2869-2882.

Menon, S, J. Hansen, L. Nazarenko, and Y. Luo, 2002: Climate effects of black carbon aerosols in China and India. *Science,* **297**, 2250-2253.

Minnis, P., L. Nguyen, D. R. Doelling, D. F. Young, W. F. Miller, and D. P. Kratz, 2002: Rapid Calibration of Operational and Research Meteorological Satellite Imagers. Part I: Evaluation of Research Satellite Visible Channels as References. *J. Atmos. Oceanic Technol.,* **19**, 1233-1249.

Mitchell, K. E., and Coauthors, 2004: The Multi-institution North American Land Data Assimilation System (NLDAS): Utilizing multiple GCIP products and partners in a continental distributed hydrological modeling system. *J. Geophys. Res., Atmos.,* **109 (D7)**.

Mukai S., and I. Sano, 1999: Retrieval algorithm for atmospheric aerosols based on multi-angle viewing of ADEOS/POLDER. *Earth Planets Space Sci.,* **51 (11)**, 1247-1254.

Murakami, M., 1983: Analysis of the deep convective activity over the western Pacific and Southeast Asia. Part I: Diurnal variation. *J. Meteor. Soc. Japan*, **61**, 60-77.

Murakami, M., 1987: Effects of the Tibetan Plateau, *Monsoon Meteorology*, C.-P. Chang and T. N. Krishnamurti, Eds., Oxford University Press, 235-270.

Nesbitt, S. W., and E. J. Zipser, 2003: The diurnal cycle of rainfall and convective intensity according to three years of TRMM measurements. *J. Climate*, **16**, 1456-1475.

NOAA/NESDIS/OSDPD/SSD, 2004: *IMS daily Northern Hemisphere snow and ice analysis at 4 km and 24 km resolution*. Boulder, CO: National Snow and Ice Data Center. Digital media.

Ohmura A., and Coauthors, 1998: Baseline Surface Radiation Network (BSRN/WRMC), a new precision radiometry for climate research. *Bull. Amer. Meteor. Soc.*, **79**, 2115 - 2136.

Parthasarathy B., Munot A.A., Kothawale D.R., 1995: Monthly and seasonal rainfall series for all-India homogeneous regions and meteorological subdivisions : 1871-1994. Research Report No. RR-065, Indian Institute of Tropical Meteorology, Pune, 113pp.

Parthasarathy, B. and S. Yang, 1995: Relationships between regional Indian summer monsoon rainfall and Eurasian snow cover. *Advances Atmos. Sci.*, **12**, 143-150. DOI 10.1007/BF02656828.

Patra, P. K., S. K. Behera, J. R. Herman, S. Maksyutov, H. Akimoto, and T. Yamagata, 2005: The Indian summer monsoon rainfall: interplay of coupled dynamics, radiation, and cloud microphysics. *Atmos. Chem. Phys.*, **5**, 2181-2188.

Pinker, R. T., X. Li, W. Meng and E. Yegorova, 2007: Towards improved satellite estimates of short-wave radiative fluxes: Focus on cloud detection over snow. 2: Results. *J. Geophys. Res.*, **112,** D09204, doi:10.1029/2005JD006699.

Pinker, R. T., J. D. Tarpley, and I. Laszlo et al., 2003: Surface radiation budget in support of the GEWEX Continental-Scale International Project (GCIP) and the GEWEX American Prediction Project (GAPP), including the North

American Land Data Assimilation System (NLDAS) Project. *J. Geophys. Res.*, **108**, D22.

Pinty, B., F. Roveda, M. M. Verstraete, N. Gobron, Y. Govaerts, J. V. Martonchik, D. J., Diner, and R. A. Kahn, 2000a: Surface albedo retrieval from Meteosat 1. Theory. *J. Geophys. Res.*, **105(D14)**, 18,099-18,112.

Pinty, B., F. Roveda, M. M. Verstraete, N. Gobron, Y. Govaerts, J. V. Martonchik, D. J., Diner, and R. A. Kahn, 2000b: Surface albedo retrieval from Meteosat 2. Applications. *J. Geophys. Res.*, **105(D14)**, 18,113-18,134.

Platnick, S., M. D. King, S. A. Ackerman, W. P. Menzel, B. A. Baum, J. C. Reidi, R. A. Frey, 2003: The MODIS cloud products: Algorithms and examples from Terra.. *IEEE Trans. Geosci. Remote Sens.* **41**, 459-473.

Prasad, A. K. and R. P. Singh, 2007: Comparison of MISR-MODIS aerosol optical depth over the Indo-Gangetic basin during the winter and summer seasons (2000 – 2005). *Rem. Sens. of Environ.*, **107**, 109-119.

Ramanathan, V., C. Chung, D. Kim, T. Betge, L. Buha, J. T. Kiehl, W. M. Washington, Q. Fu, D. R. Sikka, and M. Wild, 2005: Atmospheric brown clouds: Impacts on South Asian climate and hydrological cycle. *Proc. Natl. Acad. Sci. U .S. A.*, **102**, 5326-5333,doi:10.1073/phas.0500656102.

Ramanathan, V., and Coauthors, 2001: Indian Ocean Experiment: An integrated analysis of the climate forcing and effects of the great Indo-Asian haze. *J. Geophys. Res.*, 106(D22), 28,371–28,398.

Ramsay, B., 1998: The interactive multi-sensor snow and ice mapping system, *Hydrol. Process.*, **12**, 1537-1546.

Randall, D. A., Harshvardhan, and D. A. Dazlich, 1991: Diurnal variability of the hydrologic cycle in a general circulation model. *J. Atmos. Sci.*, **48**, 40–62.

Raschke, E., S. Bakan, and S. Kinne, 2006: An assessment of radiation budget data by ISCCP and GEWEX-SRB. *Geophys. Res. Lett*., **33**, LO7812, doi:10.1029/2005GL025503

Roca, R., S. Louvet, L. Picon, and M. Desbois, 2005: A study of convective systems, water vapor and top of the atmosphere cloud radiative forcing over the Indian Ocean using INSAT-1B and ERBE data. *Meteorol. Atmos. Phys.*, **90**, 49-65.

Roca, R., and V. Ramanathan, 2000: Scale dependence of monsoonal convective systems over the Indian Ocean, *J. Climate*, **13**, 1286–1298.

Rockwood, A. A., and S. K. Cox, 1978: Satellite inferred surface albedo over northwestern Africa. *J. Atmos. Sci*., **35**, 513-522.

Rossow, W. B., and L. C. Garder, 1993a: Cloud detection using satellite measurements of infrared and visible radiances for ISCCP. *J. Climate*, **6**, 2370-2393.

Rossow, W. B., and L. C. Garder, 1993b: Validation of ISCCP cloud detections. *J. Climate*, **6,** 2370- 2393.

Rossow, W. B., and R. A. Schiffer, 1999: Advances in understanding clouds from ISCCP. *Bull. Amer. Meteor. Soc*., **80,** 2261-2287.

Rossow, W. B., and R. A. Schiffer, 1991: ISCCP cloud data products. *Bull. Amer. Meteor. Soc*., **71**, 2-20.

Rossow, W. B., A. W. Walker, D. E. Beuschel, and M. D. Roiter, 1996: International Satellite Cloud Climatology Project (ISCCP) documentation of new cloud datasets. *WMO/TD-No. 737*, 115 pp., World Meteorological Organization.

Rozendall, M. A., C. B. Leovy, and S. A. Klein, 1995: An observational study of diurnal variations of marine stratiform cloud. *J. Climate*, **8**, 1795-1809.

SAF/LAND/MF/VR_DSSF/I_08, 2008: SAF for Land Surface Analysis Validation Report: DSSF.

Sato N., and Coauthors, 1989: Effects for implementing the SiB in the general circulation model. *J. Atmos. Sci*., **46**, 2757-2782.

Saunders, R. W., 1990: The determination of broad band surface albedo from AVHRR visible and near-infrared radiances. *Int. J. Remote Sens.*, **11,** 49–67.

Schaaf, C. B., and co-authors, 2002: First operational BRDF, albedo nadir reflectance products from MODIS. *Remote Sens. Environ*., **83(1)**, 135-148.

Schiffer, R. A., and Rossow, W. B., 1985: ISCCP Global Radiance Data Set: A New Resource for Climate Research. *Bull. Amer. Meteor. Soc*., **66**, 1498-1505.

Schiffer, R. A., and Rossow, W. B., 1983: The International Satellite Cloud Climatology Project (ISCCP): The First Project of the World Climate Research Programme. *Bull. Amer. Meteor. Soc*., **64**, 779-784.

Sen Roy, S., and R. C. Balling, 2007:Diurnal variations in summer season precipitation in India. *Int. J. Climat*e, **27**, 969-976.

Singh, O. P., 2001: Long term trends in the frequency of monsoonal cyclonic disturbances over the north Indian Ocean. *Mausam*, **52**, 4655-4668.

Song, J., and W. Gao, 1999: An Improved Method to Derive Surface Albedo from Narrowband AVHRR Satellite Data: Narrowband to Broadband Conversion. *J. Appl. Meteor.*, **38**, 239–249.

Sorooshian, S., X. Gao, K. Hsu, R. A. Maddox, Y. Hong, H. V. Gupta, and B. Imam, 2002: Diurnal Variability of Tropical Rainfall Retrieved from Combined GOES and TRMM Satellite Information. *J. Climate*, **15**, 983–1001.

Sperber, K. R., and T. N. Palmer, 1996: Interannual tropical rainfall variability in general circulation model simulations associated with Atmospheric Model Intercomparison Project. *J. Climate*, **9**, 2727-2750.

Stanhill, G., and S. Cohen, 2001: Global dimming: a review of the evidence for a widespread and significant reduction in global radiation with discussion of its probable causes and possible agricultural consequences. *Agric. For Meteorol*., **107**, 155-278.

Stephens, G. L., and Coauthors, 2002: The CloudSat Mission and the A-Train: A New Dimension of Space-Based Observations of Clouds and Precipitation, *Bull. Amer. Meteor. Soc.*, **83**, 1771-1790.

Stowe, L. L., P. A. Davis, and E. P. McClain, 1998: Scientific Basis and Initial Evaluation of the CLAVR-1 Global Clear/Cloud Classification Algorithm for the Advance Very High Resolution Radiometer. *J. Atmos. Ocean. Meteor.*, **16**, 656-681.

Strugnell, N. C., W. Lucht, and C. Schaaf, 2001: A global albedo data set derived from AVHRR data for use in climate simulations. *Geophys. Res. Lett.*, **28(1)**, 191–194.

Sui, C.H., K.M. Lau, Y.N. Takayabu, and D.A. Short, 1997: Diurnal Variations in Tropical Oceanic Cumulus Convection during TOGA COARE. *J. Atmos. Sci.*, **54**, 639–655.

Taniguchi, K. and T. Koike, 2007: Increasing atmospheric temperature in the upper troposphere and cumulus convection over the eastern part of the Tibetan Plateau in the pre-monsoon season of 2004. *J. Meteor. Soc. Japan*, **85A**, 271-294.

Tanre, D., Y. Kaufman, M. Herman, and S. Mattoo, 1997: Remote sensing of aerosol properties over oceans using the MODIS/EOS spectral radiances. *J. Geophys. Res.*, **102**, 16,971– 16,988.

Taylor, C.M. and Lebel, T., 1998: Observational evidence of persistent convective-scale rainfall patterns, *Mon. Wea. Rev.*, **126**, 1597-1607.

Tsvetsinskaya, E. A., C. B. Schaaf, F. Gao, A. H. Strahler, R. E. Dickinson, X. Zeng, and W. Lucht, 2002: Relating MODIS-derived surface albedo to soils and rock types over Northern Africa and the Arabian peninsula. *Geophys. Res. Lett.*, **29(9)**, DOI: 10.1029/2001GL014096.

Ueda, H. and T. Yasunari, 1998: Role of warming over the Tibetan Plateau in early onset of the summer monsoon over the Bay of Bengal and the South China Sea. *J. Meteor. Soc. Japan*, **76**, 1-12.

Uppala, S.M., and Coauthors, 2005: The ERA-40 re-analysis. *Quart. J. Roy. Meteorol. Soc.*, **131**, 2961-3012.doi:10.1256/qj.04.176

WCP-55, World climate research report of the experts meeting on aerosols and their climatic effects, edited by A. Deepak and H. E. Gerber, 107 pp., Williamsburg, VA, 1983.

Wei, X., A. N. Hahmann, R. E. Dickinson, Z.-L. Yang, X. Zeng, J. Schaudt, C. B. Schaaf, and N. Strugnell, 2001: Comparison of albedos computed by land surface models and their evaluation against remotely sensed data. *J. Geophys. Res.*, **106(D18)**, 20,687– 20,702.

Weinreb, M. P., M. Jamison, N. Fulton, Y. Chen, J. X. Johnson, J. Bremer, C. Smith, and J. Baucom, 1997: Operational calibration of Geostationary Operational

Environmental Satellite-8 and -9 imagers and sounders. *Appl. Opt.*, **36**, 6895-6904.

Wild, M., Ohmura, A., Gilgen, H., and D. Rosenfeld, 2004: On the consistency of trends in radiation and temperature records and implications for the global hydrological cycle. *Geophys. Res. Lett.*, **31**, L11201, doi:10.1029/2003GL019188.

Wiscombe, W.J., R. M. Welch, and W. D. Hall, 1984: The effects of very large drops on cloud absorption: I. Parcel models. *J. Atmos. Sci*., **41**, 1336- 1355.

Wonsick, M., R. T. Pinker, W. Meng, and L. Nguyen, 2006: Evaluation of surface shortwave flux estimates from GOES: Sensitivity to sensor calibration. *J. Oceanic Atmos. Sci*., **23**, 927-935.

Yang, G. Y., and J. Slingo, 2001: The Diurnal Cycle in the Tropics. *Mon. Wea. Rev*., **129**, 784–801.

Yang, K., R. T. Pinker, Y. Ma, T. Koike, M. M. Wonsick, S. J. Cox, Y. Zhang, and P. Stackhouse, 2008: Evaluation of satellite estimates of downward shortwave radiation over the Tibetan Plateau. *J. Geophys. Res.*, **113**, D17204, doi:10.1029/2007JD009736.

Yeh, T.-C, 1981: Some characteristics of the summer circulation over the Qinghai-Xizang (Tibet) Plateau and its neighborhood. *Bull. Amer. Meteor. Soc.*, **62**, 14-19.

Yeh T. C, and Y. X. Gao, 1979: *The Meteorology of the Qinghai-Xizang (Tibet) Plateau.* Science Press, Beijing, 278 pp.

Zuidema, P., 2003: Convective clouds over the Bay of Bengal. *Mon. Wea. Rev*., **131(5)**, 780-798.